Relationships between Kinematics, Microphysics and Lightning in High Plains Storms Observed During the Sever Thunderstorm Electrification and Precipitation Study

by
Sarah Anne Tessendorf

Department of Atmospheric Science
Colorado State University
Fort Collins, Colorado

Colorado State University

Department of Atmospheric Science

Paper No. 774

RELATIONSHIPS BETWEEN KINEMATICS, MICROPHYSICS, AND LIGHTNING IN HIGH PLAINS STORMS OBSERVED DURING THE SEVERE THUNDERSTORM ELECTRIFICATION AND PRECIPITATION STUDY

Submitted by

Sarah Anne Tessendorf

Department of Atmospheric Science

In partial fulfillment of the requirements

For the Degree of Doctor of Philosophy

Colorado State University

Fort Collins, Colorado

Summer 2006

ABSTRACT

RELATIONSHIPS BETWEEN KINEMATICS, MICROPHYSICS, AND LIGHTNING IN HIGH PLAINS STORMS OBSERVED DURING THE SEVERE THUNDERSTORM ELECTRIFICATION AND PRECIPITATION STUDY

The Severe Thunderstorm Electrification and Precipitation Study (STEPS) was established to improve our understanding of electrification mechanisms and lightning in High Plains storms. In particular, STEPS focused on investigating anomalous positive cloud-to-ground (CG) lightning, which had been documented to occur more often in this region than in the rest of the U.S. Radar and lightning observations of four storms observed during the STEPS field campaign are analyzed and discussed. The four cases include a predominantly positive CG-producing (PPCG) supercell on 29 June, a supercell on 3 June that produced no CG lightning of either polarity, a negative CG-producing multicellular storm on 19 June, and a PPCG multicellular storm on 22 June. Data from multiple Doppler radars have been synthesized to calculate the three-dimensional wind field, polarimetric radar variables have been combined with thermodynamic soundings to estimate hydrometeor types throughout the echo volumes, and Lightning Mapping Array (LMA) data have been sorted into flashes and studied to determine the flash rates and charge structure for several hours of each storm's lifetime. The purpose of this study is to

determine what features are unique for storms that produce predominantly positive CG lightning, and attempt to reveal the processes that lead to this behavior.

The 29 June supercell produced large amounts of hail and frequent positive CG lightning, as well as exhibited a large volume of strong (> 10 m s^{-1}) updraft and a deep region of cyclonic vertical vorticity. The charge structure of the 29 June supercell was inverted, with a main region of positive charge centered near 8 km MSL with a negative charge layer above and below. The inferred charge structure in the 3 June case consisted of an inverted dipole, with positive charge beneath upper-level negative charge. A lower negative charge layer was not detected in 3 June and may have been the reason for the lack of CG lightning. This case produced some hail, but not as much hail volume as 29 June, and the updraft volume and cyclonic vertical vorticity were dramatically lower as well. The 19 June multicellular storm exhibited a normal charge structure, with main negative charge centered at 7 km MSL, and positive charge layers above and below, and therefore produced mostly negative CG lightning. The storm produced negligible hail, and had very weak and shallow updrafts, yielding near zero values of strong updraft volume. The 22 June multicellular storm exhibited both inverted and normal charge structures in different regions of the storm complex. The volume of strong updraft was very high, similar to that of 29 June, and the storm produced ample amounts of hail. Both positive and negative CG lightning was observed in this storm complex, but the majority of the CG lightning was of positive polarity.

The results indicate that PPCG storms tend to have larger updrafts (both wider and larger in volume), which is consistent with previous studies. Large updrafts and enhanced vertical vorticity also play an important role in the production of large hail. Furthermore, low-level negative charge (below a larger region of positive charge) was observed in the cases that produced positive CG lightning, which may be the impetus needed for the flash to come to ground. This lower negative charge, in essence, represents the lowest charge layer of an inverted tripolar charge structure. The charge structures observed during the production of negative CG lightning were a normal tripole (with negative charge situated between upper and lower positive charge layers) on 19 June and an inverted dipole (with negative charge above positive) in the anvil on 22 June. Cloud-to-ground flash rates (of either polarity) decreased when either the lower charge layer of the corresponding tripolar structure was absent, or when the low-level charge layer exhibited an enhanced number of LMA sources, in which case intra-cloud (IC) discharges seemed to be preferred between the two lowest charge layers of the tripole.

Sarah Anne Tessendorf
Atmospheric Science Department
Colorado State University
Fort Collins, 80523
Summer 2006

TABLE OF CONTENTS

LIST OF TABLES

PART I

LIST OF FIGURES

PART I

PART II

PART III

PART I: THE 29 JUNE 2000 SUPERCELL OBSERVED DURING STEPS: KINEMATICS AND MICROPHYSICS

CHAPTER 1

INTRODUCTION

The Severe Thunderstorm Electrification and Precipitation Study (STEPS) was established "to achieve a better understanding of the interactions between kinematics, precipitation production, and electrification in severe thunderstorms on the High Plains" (Weisman and Miller 2000). The field campaign took place from 17 May to 20 July 2000 near Goodland, Kansas. An overview of the STEPS field program can be found in Lang et al. (2004).

STEPS research aims to identify relationships between microphysical and dynamical processes in severe storms on the High Plains and, in particular, why some storms produce predominantly positive cloud-to-ground (PPCG) lightning. One specific scientific goal of STEPS, as outlined in the Scientific Overview (http://www.mmm.ucar.edu/pdas/steps-science.html), is "To understand the formation of precipitation and its influence on electrical development, especially in those storms producing large hail." In this study, we will focus primarily on the evolutionary aspects of convective kinematics that ultimately lead to severe, hail-producing storms.

On 29 June 2000, a multi-cellular convective storm developed near Bird City, KS and intensified into a supercell as it passed through the STEPS radar network between

2130 UTC 29 June and 0115 UTC[1] 30 June. This storm produced copious amounts of large hail (up to 5 cm), an F1 tornado, as well as extraordinary intracloud (IC) flash rates (~300 min^{-1}; Williams 2001) and frequent positive cloud-to-ground (CG) lightning strikes. The unique observational platforms employed and the nearly four hours of continuous kinematic and microphysical observations permit us to add new insight to previous studies on hail growth in supercells, especially regarding evolution into the severe storm stage.

Previous studies of hailstorms have shown that supercells are responsible for much of the large hail over the High Plains (Browning 1977). Browning and Foote (1976, hereafter BF76) outlined a three-stage process for hail production in supercells. In the first stage, small particles (or embryos) grow during their initial ascent near the right flank of the main updraft. Secondly, some of these embryos circulate cyclonically around the forward flank of the main updraft as they descend. This branch forms what is referred to as the "embryo curtain" around the main updraft. Lastly, particles from the embryo curtain are able to enter the main updraft and grow into large hailstones in a single up-and-down path. Nelson (1983) concluded that, although a recycling process similar to that of the BF76 model was certainly likely, potential embryos had to be coming from a much broader region (an "embryo corridor") than the rather limited area of the BF76 embryo curtain. Several other studies (Dye et al. 1983; Miller et al. 1983, 1988, 1990) have found that, to serve as effective embryos for hail growth, particles

[1] All times are Universal Time (UTC); local time for this case study is found by subtracting six hours. All references to altitude will be in kilometers above mean sea level (MSL). The local ground level was approximately 1.1 km MSL. All listed particle sizes will be particle diameters.

entering the updraft must already be as large as 100 μm to 1 mm, thus implying that a recycling process must be taking place.

Microphysical and kinematic factors that influence hail growth during a storm's near-steady, severe stage were outlined in Nelson (1987, their Table 2). Among the list of microphysical factors that contribute to large hail are high values of supercooled liquid water and large embryos. Kinematic factors for large hail were listed as light horizontal flow across the updraft, large contiguous updraft area (with mean updraft of 20-40 m s^{-1}), and favorable horizontal updraft gradients. Nelson argued that kinematic factors had a much greater influence on "extreme hailfall" events compared to any that might result from microphysical factors as proposed by Knight and Knight (1973). We will further address the relative importance of these two basic controls on whether or not a storm can and does produce hail.

Because most studies of hail growth such as those cited have used measurements from storms that are already in their severe phase, we are left with several unanswered questions, certainly less than satisfactory answers. We still do not have a clear understanding of the relative importance of microphysics and kinematics in the production of hail and the origin(s) of the starting embryonic particles for hail growth. Further, we have only a rudimentary understanding of the evolution from early convection into severe, hail-producing storms.

This study aims to establish the nature of this storm's kinematic structure and its evolution into a severe stage with large hail, and Wiens et al. (2005) discusses how these factors may have affected its resulting electrification and lightning characteristics. This study uses synthesized wind fields from Doppler radar observations and particle growth

trajectories to investigate the relationships between the kinematics and microphysics that characterize the 29 June 2000 storm over the course of its four-hour lifetime from its earliest development through its mature and dissipating phases. Additionally, we hope to better identify the coupling of kinematic and/or microphysical controls on large hail growth. Furthermore, the diagnosis of trajectories that favored graupel and hail growth in this storm will aid in our interpretation of how the kinematics and precipitation growth might have influenced the electrification processes discussed in Wiens et al. (2005). Wiens et al. (2005) uses the New Mexico Tech Lightning Mapping Array to infer the storm's total lightning and charge structure and to examine detailed observations of PPCG lightning in this storm and theories for its production.

CHAPTER 2

DATA AND METHODS

Instrumentation and observing systems operated during the STEPS field campaign and used in this study include: three S-band Doppler radars (two of which were polarimetric research radars) for mapping the three-dimensional structure of precipitation and storm winds; balloon-borne in situ electric field mills to measure in-storm parameters including temperature, pressure, wind, and electric field operated by the National Severe Storms Laboratory, (NSSL, Rust and MacGorman 2002); a mobile sounding unit for environmental wind and thermodynamic profiles near the storm; and the National Lightning Detection Network (NLDN) to measure CG lightning strike locations and polarities in "real time" (Cummins et al. 1998).

2.1 Basic radar data and derived winds

The Colorado State University CSU-CHILL and National Center for Atmospheric Research (NCAR) S-Pol polarimetric Doppler radars, along with the Goodland National Weather Service (NWS) WSR-88D radar (KGLD) comprised the triple-Doppler radar network for STEPS (Table 1). The three radars were arranged in a roughly equilateral triangle with ~60-km baselines providing radar coverage of eastern Colorado, northwestern Kansas, and southwestern Nebraska (Fig. 1). All of these radars measure reflectivity (Z_h) and radial velocity (V_r) derived from transmitted and received signals

that are horizontally polarized. The research radars also measure the following polarimetric variables: differential reflectivity (Z_{dr}), linear depolarization ratio (LDR), the correlation coefficient (ρ_{hv}), and the differential propagation phase (ϕ_{dp}). Overviews of polarimetric variables and their use in bulk hydrometeor detection can be found in Herzegh and Jameson (1992), Doviak and Zrnic (1993), Bringi and Chandrasekar (2000), and Straka et al. (2000). Such capabilities provide particle shape and size information, which can be combined with air temperature from a local sounding to infer hydrometeor types within storms (Herzegh and Jameson 1992; Conway and Zrnic 1993; Carey and Rutledge 1996; Carey and Rutledge 1998, Straka et al. 2000; see following section for details).

The CHILL and S-Pol Z_h, Z_{dr}, and LDR fields along with radial velocity data and received powers from each horizontally- and vertically-polarized channel were routinely interpolated onto a 0.5-km resolution Cartesian grid using NCAR's Sorted Position Radar INTerpolator (SPRINT: Mohr and Vaughn 1979; Miller et al. 1986). Second trip echo contamination in the CHILL data was eliminated by thresholding on differential propagation phase.[2] S-Pol radial velocities were omitted where sidelobe contamination was suspected. After interpolation, the velocity data were unfolded by means of NCAR's Custom Editing and Display of Reduced Information in Cartesian Space (CEDRIC) software (Mohr et al. 1986).

[2] Data were omitted when $\bullet_{dp} > -5°$ prior to 2338 UTC. Past this time differential phase shift values had increased within the first trip echo such that a more conservative threshold of $\bullet_{dp} > 30°$ was required.

The three-dimensional wind fields were computed using the radial velocities from all three radars when available; otherwise, winds were computed from only two radars. Interpolated radial velocities were advected during the synthesis process in accordance with the method outlined by Gal-Chen (1982). Vertical air motion was obtained by integrating the continuity equation using the variational scheme (O'Brien 1970). This synthesis procedure was done every ~5 min (synchronized full volumetric scans of the storm were done by all three radars at this time interval) for 36 volume scans during the nearly four-hour observation period 2130 UTC 29 June through 0115 UTC 30 June.

At 0004 30 June, NSSL launched a balloon that provided vertical profiles of electric field and temperature through the updraft. The temperature sounding was used in the classification algorithm for hydrometeor types from polarimetric radar data.

2.2 Hydrometeor classification

The original CHILL and S-Pol polarimetric data were first edited to eliminate noise, clutter, and suspect data using thresholds in ρ_{hv} and the standard deviation of ϕ_{dp}. These methods have been described in Ryzhkov and Zrnic (1998) and used in studies such as Carey and Rutledge (1996, 1998, 2000) and Cifelli et al. (2002). Specific differential phase (K_{dp}) was then calculated from the differential phase in the manner outlined in Hubbert and Bringi (1995) and Carey et al. (2000). These edited data were separately interpolated with SPRINT to the same 0.5-km grid. A fuzzy logic hydrometeor classification algorithm (hereafter FHC), adapted from Liu and Chandrasekar (2000) and Straka et al. (2000), was implemented for the Cartesian gridded data to estimate bulk hydrometeor types within the storm (see Table 2 for classification

criteria). There are limitations to this procedure that must be kept in mind. Clearly, most radar pulse volumes within a storm consist of more than just one hydrometeor type, thus the FHC-inferred type most likely represents those particles which dominate the radar received signals. FHC-inferred hydrometeor types have been based largely on theory; however, limited studies such as Liu and Chandrasekar (2000) have compared FHC output to some ground-based and in situ observations and successfully validated the FHC procedure in their cases.

An example of the polarimetric data and corresponding FHC results at 2331 during the storm's severe phase are shown in Fig. 2. Horizontal sections in Fig. 2 show that the region of hail is immediately surrounded by rain and drizzle at 3 km (Fig. 2a), and by graupel and ice at 8.5 km (Fig. 2b). The vertical section in panels (c) and (e) highlights a so-called Z_{dr} column (Hall et al. 1984, Illingworth et al. 1987), which in this case extends upward to nearly 7 km to temperatures well below freezing. Observed values of Z_{dr} in excess of 4 dB indicate that oblate water drops as large as 4-6 mm (Wakimoto and Bringi 1988, Bringi and Chandrasekar 2000) were present within the west side of the radar echo vault. Elevated K_{dp} values, indicative of high liquid water content associated with the presence of oblate drops (Hubbert et al. 1998), are also seen in the lowest regions of the Z_{dr} column (Fig. 2g). The Doppler-derived winds shown in the vertical cross-sections (Figs. 2c-g) indicate that these large water drops were located on the fringe of the updraft and just beneath the so-called embryo curtain (BF76). If the winds allow these sizes of water drops to enter the updraft and rise to freezing levels, they will serve as very efficient cloud water collection centers that can rapidly attain large hailstone sizes.

A small pocket of elevated LDR directly above the apex of the Z_{dr} column is evident in panels (d) and (f) of Fig. 2. Bringi et al. (1997) showed that an LDR 'cap' was consistent with partially frozen rain or wet graupel. Smith et al. (1999) described this feature as raindrops in the process of freezing. The vertical cross-section of FHC output in Fig. 2c clearly shows this characteristic signature associated with the process of drops freezing and becoming high-density graupel or small hail. Large values of LDR around the periphery of the storm within low reflectivity are a result of dividing the returned signal in the horizontal channel by the weakly depolarized, nearly noise values in the vertical channel in the LDR calculation and should be considered suspect.

Hydrometeor echo volumes were also calculated for each radar scan time by multiplying the number of grid points (N) that satisfied the hydrometeor type of interest by the volume of a grid box (0.125 km^3).

2.3 Precipitation growth model

The precipitation growth model is from Knight and Knupp (1986) and, as used here, only includes a high-density growth phase. Since density is used only in the model calculation of particle fallspeed, we strongly feel this approach is adequate for our purposes. We will rely on the FHC results to identify the most likely particle types at all times and throughout the observed storm volumes.

The Knight and Knupp growth model uses a simple microphysical scheme whereby all particles are assumed to be spherical and geometrically sweep out cloud water, which is converted to particle mass during each 10-sec time step. The amount of cloud water mass which gets converted to particle mass depends on the collection

efficiency, which for this study was assumed to be unity. Temperatures and liquid water contents within cloud are based upon their adiabatic values computed from the representative sounding (Fig. 4a) as follows. To simulate horizontal entrainment at each altitude, we linearly decrease the liquid water content from its adiabatic value inside the core updraft with speeds >10 m s^{-1} to 0 at $w \leq 0$ m s^{-1}. The in cloud temperature is treated in a similar way except it is decreased to the environmental air temperature outside the updraft. In the vertical direction, we further decrease the liquid water content linearly from its adiabatic value at the -30° C level, to 0 at the -40° C level to approximate the effects of glaciation and depletion near storm top. Particles are allowed to grow anywhere between cloud base and the -40° C level, though very little increase in mass will occur in the lower regions of the cloud since the cloud liquid water content there is relatively small.

Sensitivity tests conducted by us and by Knight and Knupp (1986) indicate that final particle size depends most on the prescribed cloud liquid water content and the Doppler-derived winds, and less so on the initial locations and sizes of small embryonic particles for the growth trajectories. Further, we agree with Knight and Knupp's (1986) suggestion that adding any further detail or sophistication in the growth model is rather pointless in light of the overwhelming sensitivity to the winds and the cloud liquid water content, which at best, can only be prescribed in some sort of realistic way consistent with our intuition. The model does not consider microphysical processes such as particle freezing, melting, wet and dry growth, shedding of liquid water, or breakup of large water drops. This also means that whether the particle is liquid or frozen is not an explicit

output from the model so that its type must be arbitrarily assigned as a function of size and the temperature at the particle's current location.

It is not our intent in this study to be overly concerned about the details of precipitation growth, but rather to use the growth model as a diagnostic tool to help evaluate possible embryo source regions and growth paths that occur under our prescribed conditions, and to determine how this storm likely became the severe, hail-producing storm that was observed. Results from the precipitation growth model will be combined with all the observations, including results from the hydrometeor classification scheme, to develop a physically-consistent picture of the overall microphysical aspects of this storm's evolution.

Table 1. Characteristics of the radars used in this study

Radar Characteristic	**CSU-CHILL**	**NCAR S-Pol**	**KGLD WSR-88D**
Wavelength (cm)	11.01	10.71	10.0
Polarization	Linear, H & V	Linear, H &V	Linear, H
Peak Power (kW)	800-1000	>1000	475
Beamwidth (deg)	1.1	0.91	1.0
Pulse Repetition Frequency (Hz)	1000	960	1000
Nyquist ($m\ s^{-1}$)	27.5	25.7	25
Maximum range (km)	150	156.25	150

Table 2. Thresholds used to construct membership beta functions in the fuzzy logic hydrometeor classification.

Type	Z_h (dBZ)	Z_{dr} (dB)	K_{dp} (° km^{-1})	LDR (dB)	ρ_{hv}	T (°C)
Drizzle	< 28	0 to 0.7	0 to 0.03	< -32	> 0.97	> 0
Rain	25 to 60	> 0.7	0.03 to 6	-34 to –27	> 0.95	> -10
Dry Snow	< 35	> 0	0 to 0.6	< -25	> 0.95	< 0
Wet Snow	< 45	0 to 3	0 to 2	-13 to -18	0.82 to 0.95	-1.5 to 2.5
Vertical Ice	< 35	-0.5 to 0.5	<-0.25	< -24	> 0.95	< 0
Low-density Graupel	40 to 50	-0.5 to 1	-0.5 to 0.5	< -30	> 0.96	< -1
High-density Graupel	40 to 55	-0.5 to 3	-0.5 to 2	-25 to -20	> 0.95	-15 to 15
Small Hail (D<20mm)	50 to 60	-0.5 to 0.5	-0.5 to 0.5	-18 to -24	0.92 to 0.98	< 18
Large Hail (D>20mm)	> 55	< 0.5	-0.5 to 1	> -20	0.84 to 0.92	N/A

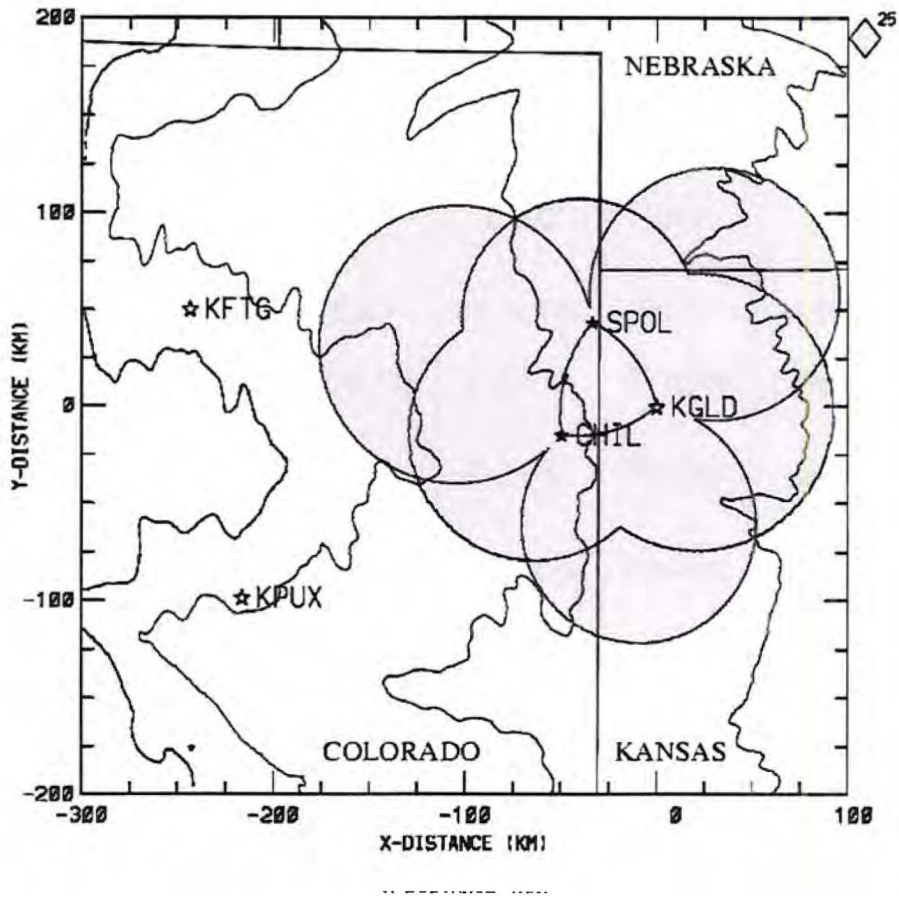

Figure 1. Nominal areas of coverage (gray shading outlined with thick black lines) by the STEPS radar network (CHIL-SPOL-KGLD) for dual-Doppler (beam-crossing angles between 25°-155°) winds. Topographic height contours (black lines) are at 3, 4, 5, and 6 kft. The straight, thin black lines are the CO-KS, CO-NE, and KS-NE state borders. NWS WSR-88D radars are shown for Denver CO (KFTG), Pueblo CO (KPUX), and Goodland KS (KGLD). All distances are East-West (X) and North-South (Y) from the Goodland radar.

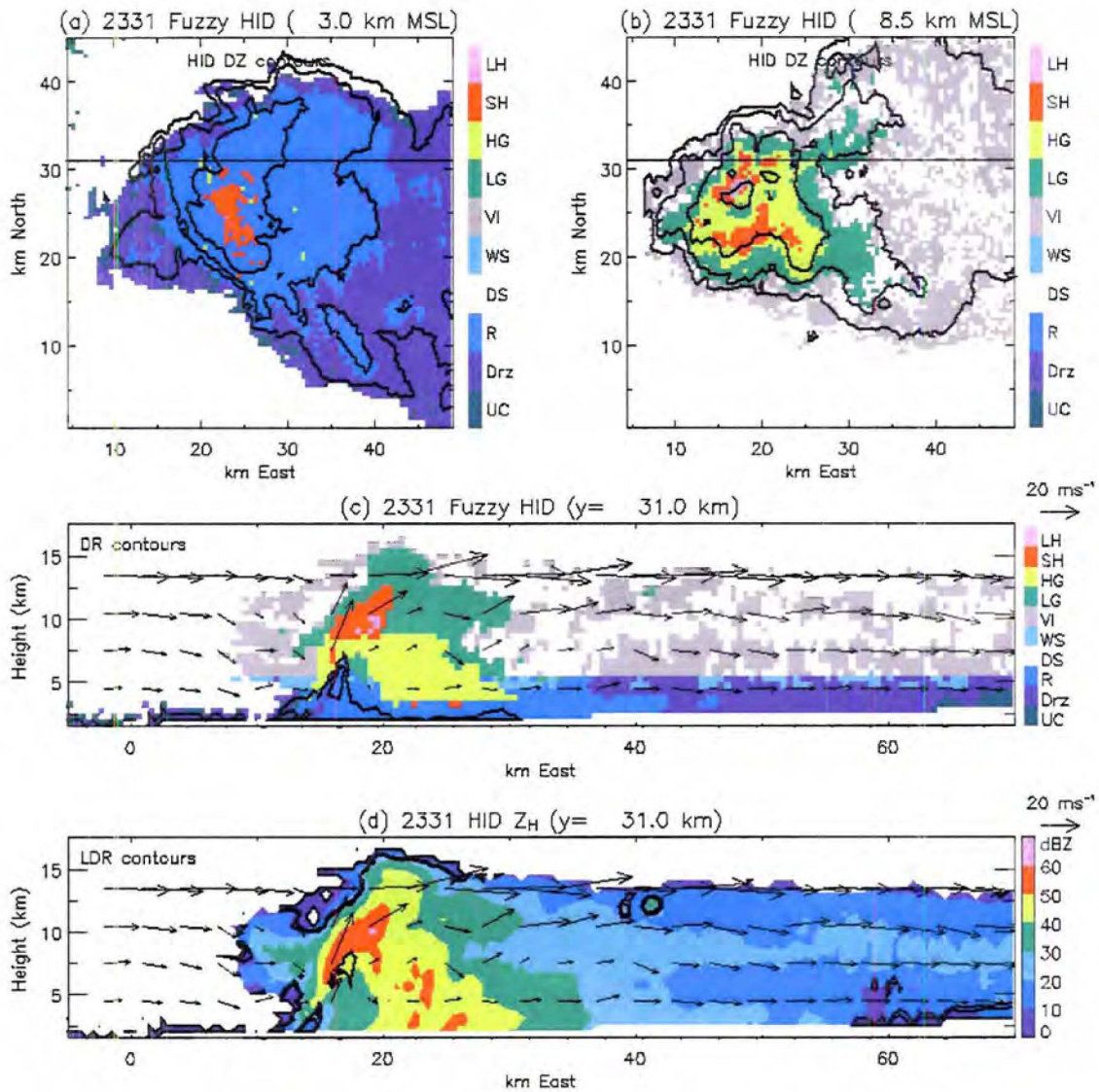

Figure 2. Horizontal cross sections of FHC output at 2331 for (a) z = 3 km MSL and (b) z = 8.5 km MSL with reflectivity contours overlaid in black starting at 15 dBZ with an interval of 15 dBZ. Vertical cross sections at y = 31 km of (c) FHC with black Z_{dr} contours of 2 and 4 dB overlaid, (d) reflectivity with black LDR contours of -20 and -18 dB overlaid, (e) Z_{dr} color contours, (f) LDR color contours, and (g) K_{dp} color contours. Hydrometeor types are: large and small hail (LH and SH), high-density and low-density graupel (HG and LG), vertical ice (VI), wet and dry snow (WS and DS), rain (R), drizzle (Drz), and unclassified category (UC). Storm-relative wind vectors (plotted every 3 km) in the vertical plane are overlaid onto (c)-(g) for reference.

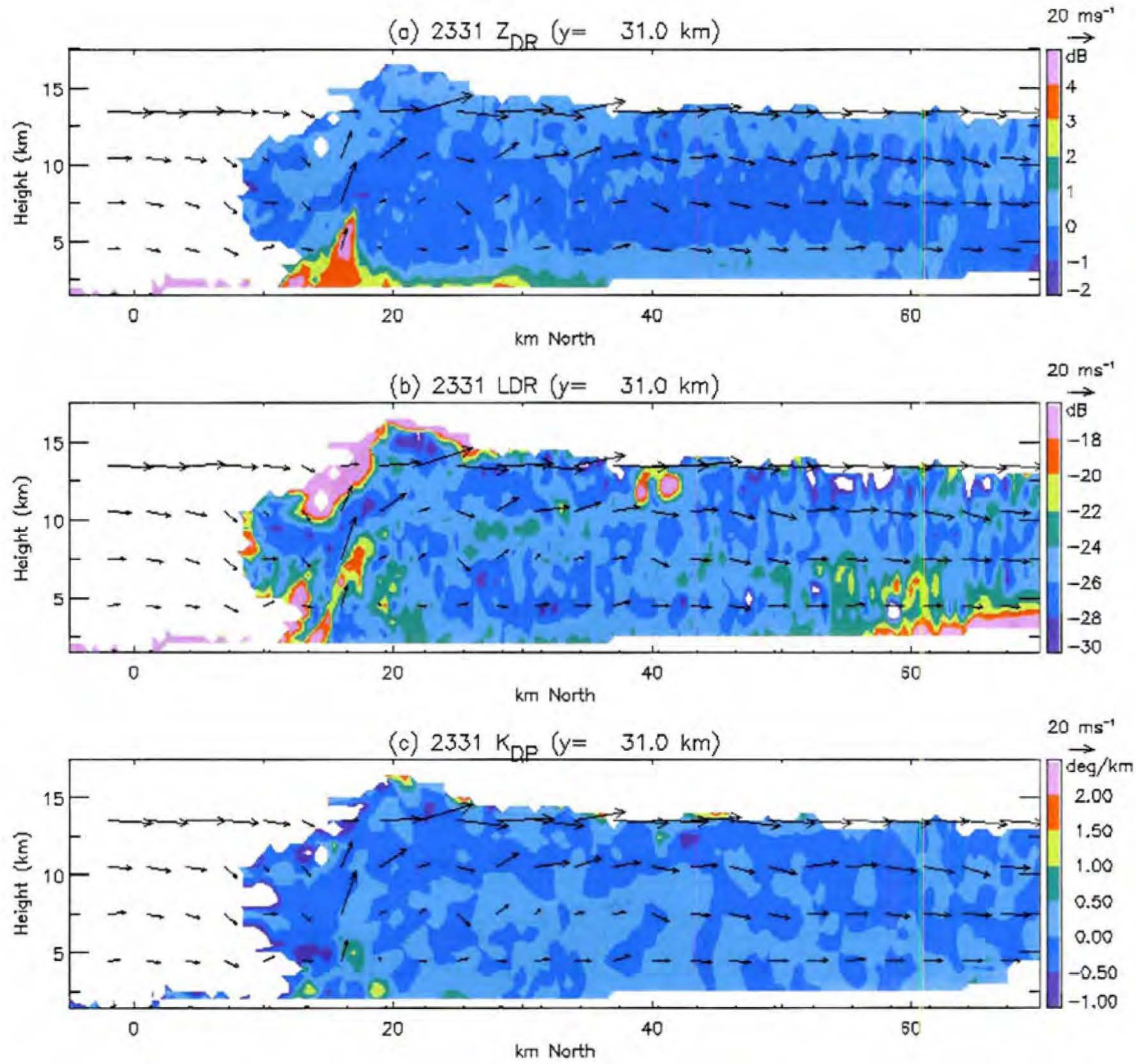

Figure 2 (cont'd).

CHAPTER 3

STORM ENVIRONMENT AND EVOLUTION

3.1 Environmental conditions

Early convection which eventually moved through the STEPS radar domain developed along a southeastward moving SurFace Boundary (SFB) associated with low-level moisture advection by the southerly flow ahead of an advancing mid-level short-wave that passed over the area (Fig. 3). The SFB was identifiable mostly as a wind shift line with southerly to south-southeasterly surface flow ahead of it and northerly to northwesterly flow behind it. There was about 5-10° F contrast in dew point and very little contrast in temperature across this surface boundary. There was sufficient convergence across the SFB to initiate small cumulus clouds seen as a thin-line echo in the regional composite of WSR-88D data (Fig. 3). Once this SFB entered the northwest corner of Kansas, it could be seen with STEPS radars as a thin-line echo oriented southwest to northeast. The large radar echo mass to the northeast of the SFB also passed southeastward, but it was well outside the STEPS domain. Second trip echoes from this larger Mesoscale Convective System (MCS) did occasionally contaminate the STEPS radar data.

The environmental soundings (Fig. 4) were taken with NCAR Mobile GPS/Loran Sounding Systems (MGLASS) both ahead of (Fig. 4a) and behind (Fig. 4b) the

advancing SFB. High surface-based Convective Available Potential Energy (CAPE was 1254 J kg^{-1} according to the 2022 Goodland sounding, Fig. 4a) and a veering, strongly sheared (5-10 m s^{-1} per 3.5 km in the low levels) wind profile are ingredients that favor severe thunderstorm (supercell) development (Moller et al. 1994). The sounding taken at 2338 (Fig. 4b) behind the SFB showed much drier environmental air above 550 mb (~5 km). Low-level outflow was not resolved in the Doppler-derived winds since the lowest reliable level was about a kilometer above the surface; however, winds from the NWS operational surface network were consistent with a mid- to upper-level, rear inflow of northwesterly to westerly air to form the low-level downdraft and outflow, especially during the later intense phase of the storm of interest.

3.2 Overview of storm evolution

The 29 June supercell (marked as Storm A in Fig. 5) was first detected as a small echo at 2130 along the southeastward-moving SFB. Another storm (B in Fig. 5) persisted throughout most of Storm A's lifetime, although it did not become severe, unlike Storm A. During the period 2130-2325, prior to its right turn and tornadic stage, Storm A moved[3] east-southeastward, toward 115°, at a speed of roughly 10 m s^{-1}. By about 2328 the storm had completed a 35° right turn, and began to travel somewhat more slowly with a velocity of 9 m s^{-1} towards 150°. Since the right turn signaled the time when the storm entered its most severe and steady phase, it will be used as a reference throughout the remainder of the discussion.

[3] Storm motion was estimated following the core of reflectivity.

The rather abrupt looking right turn most evident along the path of the core reflectivity (heavy dark line in Fig. 5a) is actually quite gradual in both updraft and vertical vorticity (Fig. 5b-c). The updraft and reflectivity cores were mostly co-located until the right turn at which time the updraft core became offset toward the right flank (southwest portion of the storm) of the reflectivity core. Likewise, the vorticity core was displaced farther yet from the right flank of the reflectivity core. This displacement meant that strong cyclonic horizontal flow was now located around the right flank of the updraft. The importance of this development in enabling this storm to produce large hail (>2 cm) will be explored more fully in Sec. 4. Two other noteworthy severe weather events, that occurred when the storm turned right, were the touchdown of a tornado at 2328 (T in Fig. 5) and the dramatic increase in +CG activity. The tornado dissipated around 2344. The NSSL mobile mesonet (Straka et al. 1996) team unofficially categorized the tornado as F1 on the Fujita scale. Only a few positive polarity CG strikes were detected prior to the right turn; however, once the storm had made its right turn, both in-cloud and CG lightning activity increased dramatically as seen in Fig. 5.

According to Storm Data (maintained by the National Climatic Data Center at http://www4.ncdc.noaa.gov/cgi-win/wwcgi.dll?wwEvent~Storms), large hail (>2 cm) was first reported at 2235. Hail sizes to 4.5 cm were reported at 2307. By 0054, the storm exhibited large low-level radar reflectivities (up to 75 dBZ) and was still producing very large hail (~5 cm) according to mobile mesonet reports.

3.3 Detailed storm evolution

Several storm features including volumes of reflectivity, updraft, vertical vorticity, and hail are quantified in Fig. 6. The dashed line shown in Fig. 6a indicates that the total storm volume (Z_h >0 dBZ) gradually increased over the observation period. Since the other radar-derived variables underwent a similar gradual growth trend, we chose to normalize these by dividing them by the total storm volume in order to highlight any shorter-duration surges that might be evident during the storm's evolution. This procedure helped identify four distinct periods in the storm's lifetime: a developing phase (2130-2213), a mature phase (2213-2325), a Severe Right (SR) mature phase (2325-0036), and a declining phase (0036-0115). These four stages closely follow the life-cycle classification scheme for severe storm cells proposed by Browning (1964) as distinct from the three-stage classification scheme used by Byers and Braham (1949) to describe the evolution of individual, non-severe thunderstorm cells.

Detailed horizontal cross-sections of low- and mid-level wind and reflectivity features along with vertical cross-sections through the storm core are shown in Figs. 7-11. These cross-sections were chosen as representative of the various phases in the lifetime of this storm. The following detailed discussion will follow the time history of events as shown in Fig. 6, while referring to these detailed cross-sections when needed.

3.3.1 DEVELOPING PHASE (2130-2213)

Reflectivities were below 50 dBZ, updraft volume was small and transient, and there was no mesocyclonic-strength vertical vorticity (>10^{-2} s^{-1}; Moller et al. 1994) or hail echo volume (Fig. 6). Total lightning flash rates (calculated according to the method

outlined in Wiens et al. 2005) increased to 10-20 flashes min^{-1}, but no CG lightning was detected (Fig. 6e). Reflectivity structure of the storm at this point was fairly non-descript (not shown). Near the end of this stage, a weak and shallow Z_{dr} column was detected, which indicated the presence of large oblate drops entering the updraft. Soon after the first appearance of the Z_{dr} column, hail above the melting level was evident (Fig. 6d). By 2213, the updraft volume exhibited a sharp increase, and reflectivities above 50 dBZ as well as vorticity greater than 10^{-2} s^{-1} were observed. The storm relative flow was from the south-southwest at low levels, while from the northwest aloft. Reflectivities were as high as 65 dBZ and appeared somewhat multicellular with two distinct updraft cores, the stronger of the two reaching 15 m s^{-1} (Fig. 7c). The stronger of these two cells continued development into the mature phase.

3.3.2 MATURE PHASE (2213-2325)

The volume of updraft greater than 10 m s^{-1} remained high, measurable volumes of high reflectivity and vorticity were present, and two periods of hail growth and fallout were detected[4] (Fig. 6). The total lightning flash rates doubled to peak at ~100 min^{-1} at 2239 then decreased back to ~50 min^{-1}. A few CG flashes were detected and the storm exhibited a vaulted structure in reflectivity during the peak of this phase (2239-2252; see also Fig. 8c). This vault indicates that a strong, broad updraft persisted over a significant depth and prevented hydrometeors from growing along a path from cloud base to radar detectable sizes within its core. A horizontal cross-section through the vault at 2239

[4] We have used hail echo volume below the melting level as a proxy for hail fallout since the lowest level radar scans were not consistently available throughout the entire analysis period.

reveals a Bounded Weak Echo Region (BWER[5]) in the reflectivity field with the corresponding updraft core in its center (Fig. 8b). A shallow isolated cell was present to the southwest of the storm at this time (Fig. 8a), which may have provided some embryos for hail growth as it was upwind of the storm relative low-level inflow. The low-level, storm-relative flow exhibited more cyclonic curvature, while the mid-level flow was more westerly and divergent around the updraft core (Fig. 8). The end of this phase was marked by a brief decline in the high reflectivity, vorticity, and hail volumes (Fig. 6).

We can only speculate about the cause of this decline since there are a number of potential causes, acting singly or in concert. Most likely, the earliest phases of this storm are best described as consisting of a modest-strength evolutionary component on top of an initially weaker, but steadier (perhaps persistent is a better term) component. The storm transitions from a rapidly evolving, weak phase to a slowly evolving (near steady), strong phase somewhat similar to the separate concepts of steady, and weak- and strong-evolution presented by Foote and Frank (1983).

3.3.3 SR MATURE PHASE (2325-0036)

A dramatic increase in vorticity volume and touchdown of the tornado, as well as the right turn itself, distinguished the beginning of the SR phase at 2325 (Fig. 6). A steady increase in total lightning flash rate and a sudden rise in CG flash rate (predominantly of positive polarity) were also evident (Fig. 6e). The low-level

[5] In our view, the BWER is an inverted bowl-like structure where the inside surface of the bowl represents the upward displacement, by an intense updraft, of the family of three-dimensional trajectories of significantly-sized precipitation particles.

reflectivity field at 2325 exhibited a flanking line of weak echo extending westward from the high reflectivity core (Fig. 9a). This flanking line was likely associated with outflow[6] beneath one of the early updraft surges that was now dissipating as it continued toward the northeast. The mid-level reflectivities show evidence of two BWERs, one more pronounced within a stronger (up to 45 m s^{-1}) and deeper updraft and located nearer the core of the storm, and the other weaker and located more along the flanking line (Fig. 9).

In environments with a clockwise-turning hodograph, Rotunno and Klemp (1982) found that a vertical pressure gradient is enhanced on a storm's right flank, favoring right-flank updraft growth and intensification. Through numerical simulations, Klemp et al. (1981) showed that a right turn occurred after the original updraft elongated and split or after a second updraft (possibly initiated along an advancing gust front) developed on the right flank of the original one. Consistent with the latter idea, successive syntheses indicated that the new updraft on the right flank of this storm continued to grow and became dominant, while the original updraft was cut off at low-levels and then dissipated. There also appears to be more divergence of the storm relative flow around the mid-level updraft at this time, particularly to its south, leading to the reflectivity maximum southeast of the main updraft (Fig. 9b).

Approximately 20 minutes after the beginning of the SR phase, the volumes of reflectivity greater than 50 dBZ and hail above the melting level abruptly rose to their peak values (Figs. 6a and d). The vertical vorticity volume greater than 10^{-2} s^{-1} had begun to decline by 2343, coincident with the dissipation of the tornado. At this time, a

[6] Our synthesis does not show such a so-called rear flank downdraft, but this is likely due to the lack of low-level radar data needed to detect the associated (and apparently shallow) divergence near the ground.

large area of low-level reflectivities exceeded 60 dBZ and the storm had developed a strong, broad updraft on its right-flank (Fig. 10). The mid-level BWER seen in Fig. 8 had nearly filled in with high reflectivities by 2343, presumably due to the presence of large hydrometeors. Cyclonic low-level storm relative flow and strong divergence of the mid-level storm relative winds around the main updraft were still apparent. A low-level hook echo, typical of most "classic" supercells, was not detected until near the middle of this phase even though the storm had been a severe right-moving storm for over 30 minutes. The total lightning flash rate reached its peak value of near 300 flashes min^{-1} near 0020. There was a distinct spike in CG flash rates near the end of this period (Fig. 6e).

3.3.4 DECLINING PHASE (0036-0115)

This phase began near 0036 when the high reflectivity, updraft, vorticity, and hail volumes were waning (Fig. 6) and ended as the storm propagated outside of the radar domain. It should be noted that this storm persisted for another three hours as part of a large mesoscale convective system (MCS to the upper right in Fig. 3) before complete dissipation. At 0036, the broad area of low-level reflectivity greater than 60 dBZ had elongated parallel to the storm relative flow and a mid-level BWER could be discerned again (Fig. 11). A new cell had developed to the northwest of the storm near 0004 and can be seen in Figure 11a. The low-level storm relative flow was still slightly cyclonic along the storm's right flank, and mid-level divergence around the updraft was still evident (Fig. 11). Even in the presence of a strong and broad updraft, the vaulted nature of the storm was beginning to subside, and was gone by 0049. The absolute peak in the CG flash rate occurred just at the end of the analysis period (Fig. 6e).

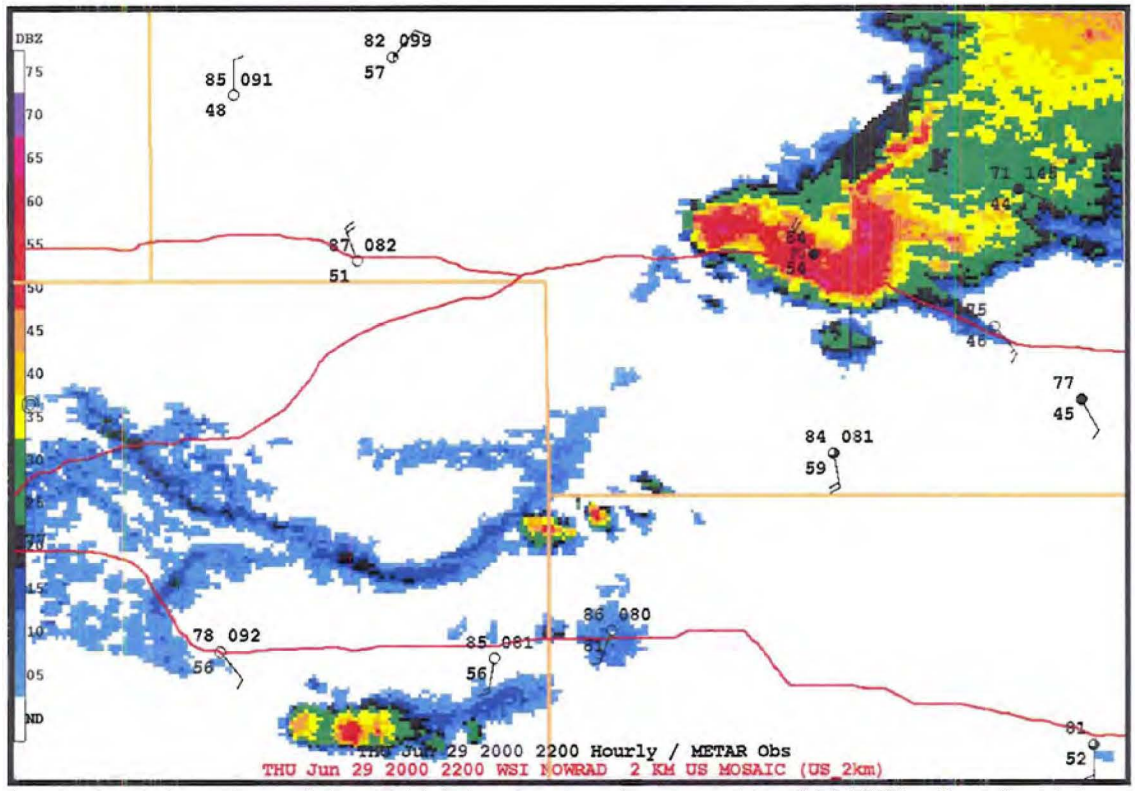

Figure 3. Subsection of the WSI 2-km National composite of NOWRAD reflectivity at 2200 on 29 June 2000. Surface data are plotted with standard station meteograms: temperature (F, upper left), dew point temperature (F, lower left), and last three digits of surface pressure (mb*10, upper right), along with % cloud cover and weather. Wind speeds are half barb (5 knots) and full barb (10 knots).

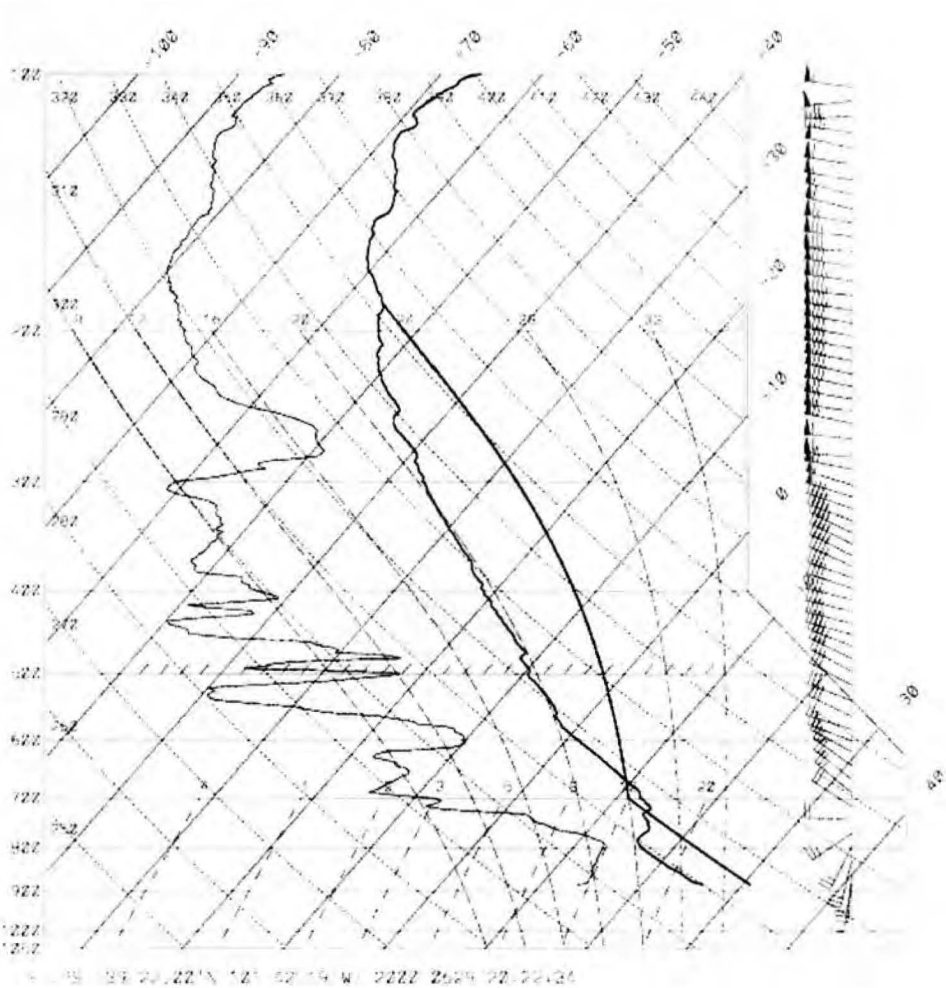

(a)

Figure 4. Skew-T plots of MGLASS soundings on 29 June 2000 at (a) 2022 UTC in Goodland and (b) 2338 UTC in northeastern Colorado near Holyoke, north of SPOL.

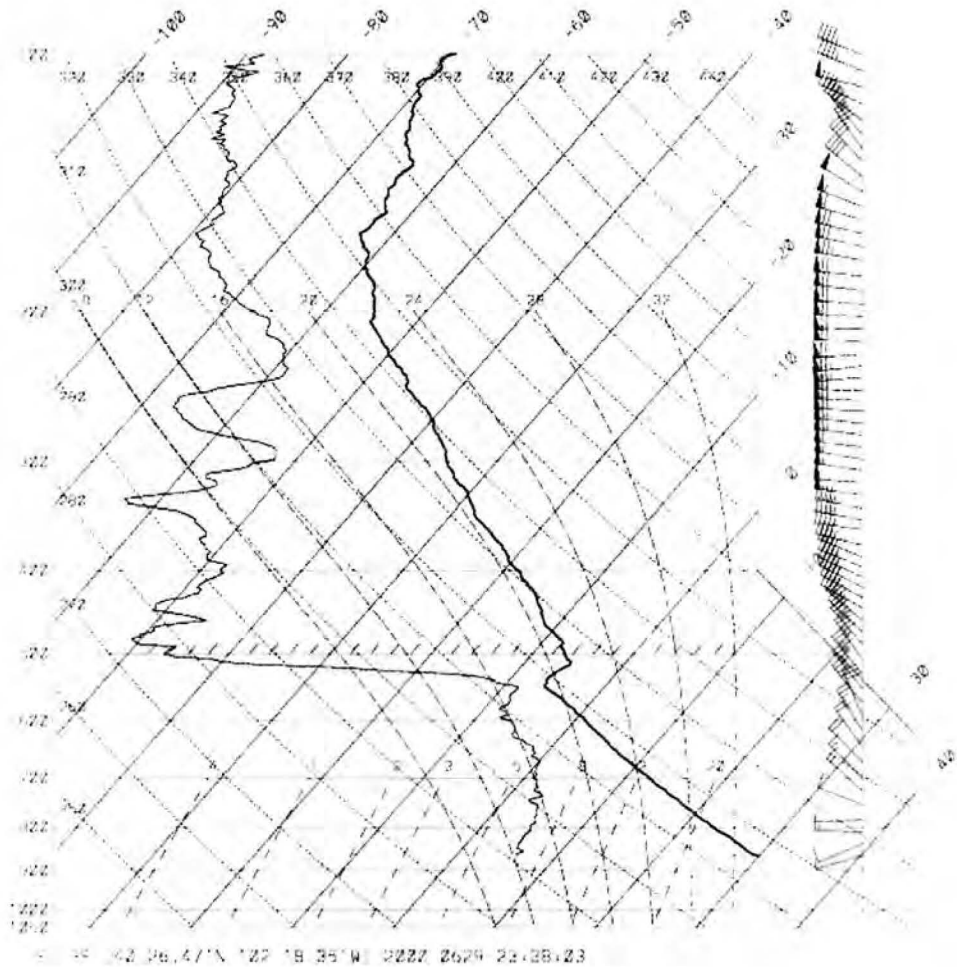

(b)

Figure 4 (cont'd).

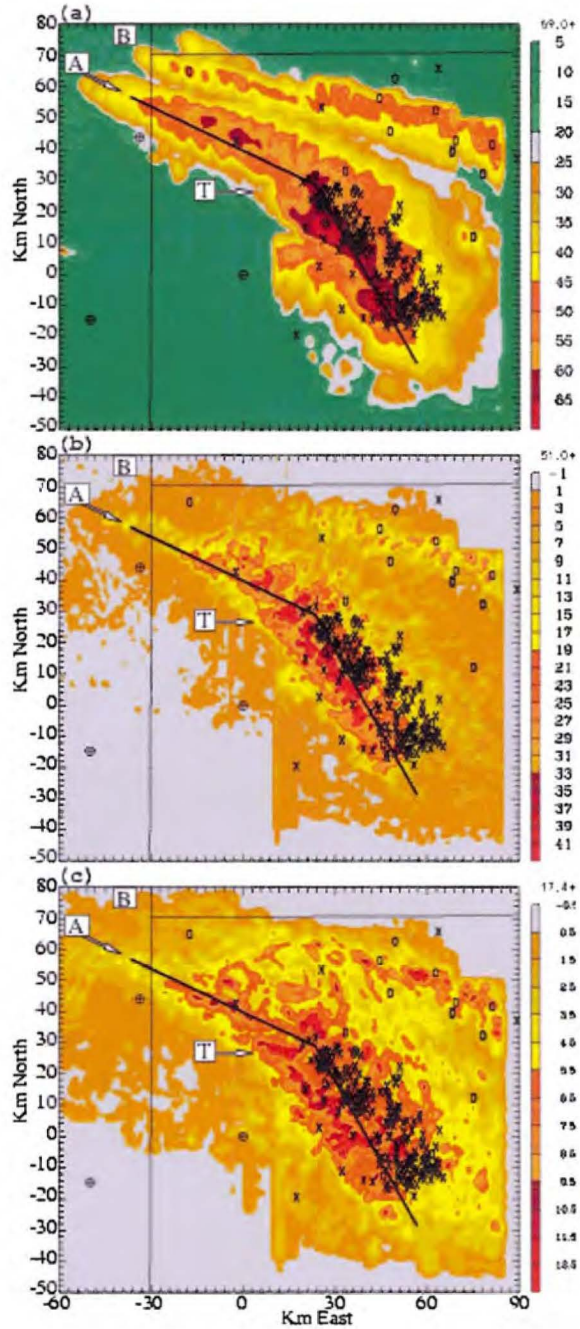

Figure 5. Swaths of maximum in the vertical column (a) KGLD reflectivity (dBZ), (b) updraft (m s^{-1}), and (c) vertical vorticity (10^{-3} s^{-1}) for the period 2130-0115 UTC with NLDN lightning data overlaid (x = positive CG flash, o = negative CG flash). Radar locations are denoted with a '⊕' symbol, with KGLD at (x,y) = (0,0). The storm motion (based on the path of the reflectivity core) is highlighted with a black line. The symbol (A) denotes the storm of interest, (B) an adjacent non-severe storm, and (T) the tornado and its path.

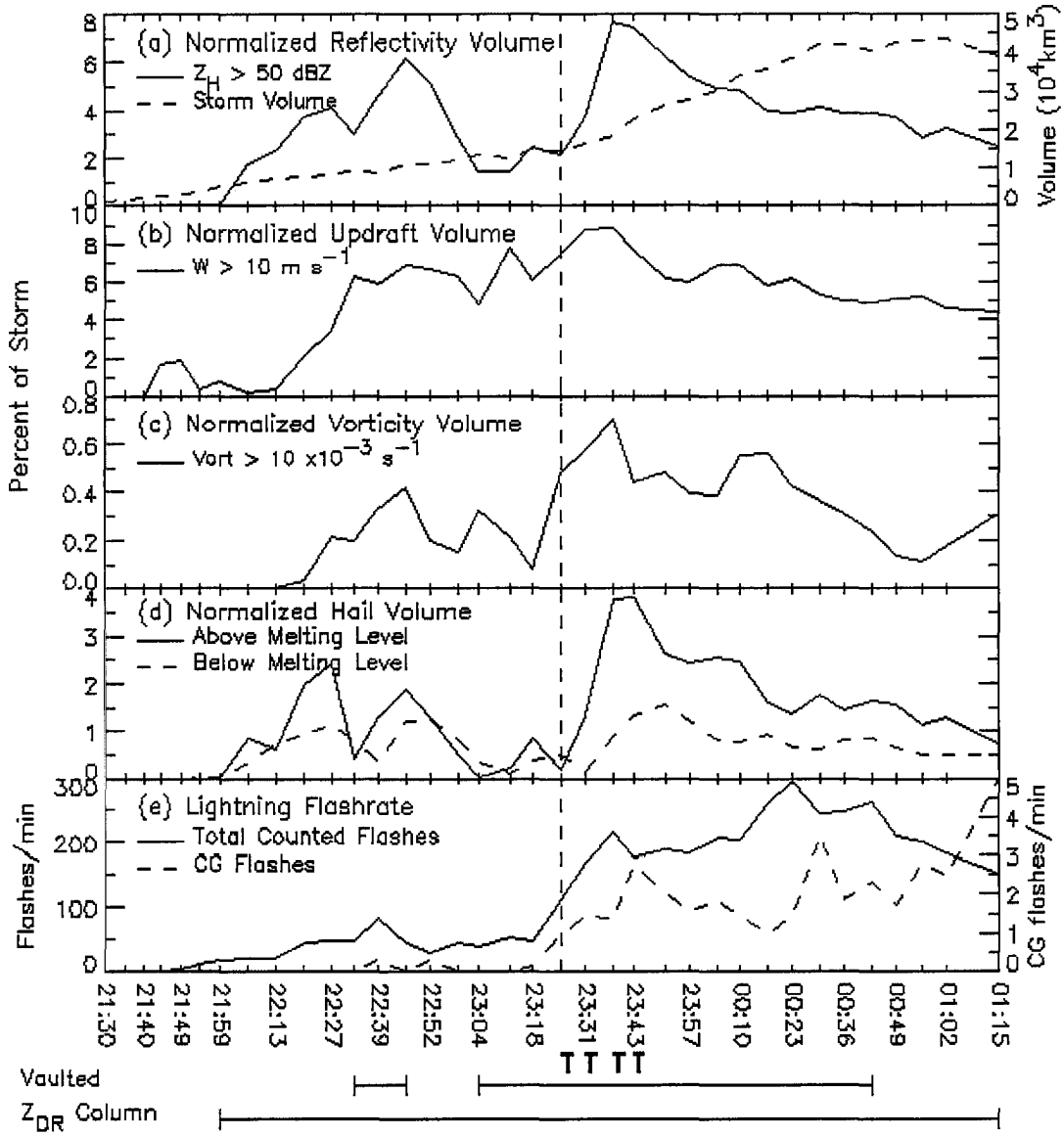

Figure 6. A time series overview of observed storm characteristics including: (a) the total storm volume (km^3) with reflectivity greater than 0 dBZ (dashed line) and the percent of the total storm volume with reflectivity greater than 50 dBZ (solid line), (b) percent of the total storm volume with updrafts greater than 10 m s^{-1}, (c) percent of the total storm volume with vertical vorticity greater than 10^{-2} s^{-1}, (d) percent of total storm volume with hail detected by FHC above the melting level (solid line) and below the melting level (dashed line), and (e) total lightning flashrate (solid line) and cloud-to-ground lightning flashrate (dashed line) for each time (UTC) during the analysis period. The 'T' indicates the tornado was on ground at that time, and bars across the bottom of the plot indicate the times when the storm had a vaulted reflectivity structure or a Z_{dr} column of at least 2 dB in magnitude. The vertical dashed line represents the time that the storm made its right turn.

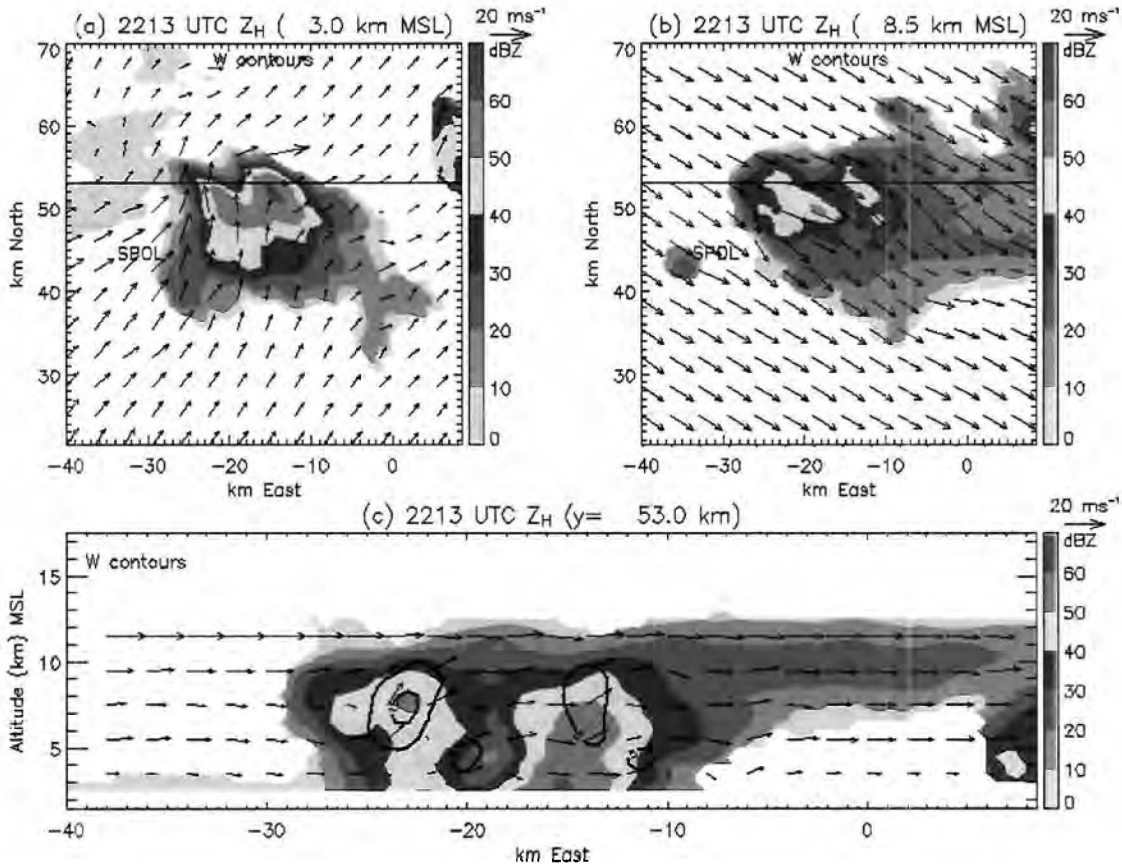

Figure 7. Winds and storm structure illustrating the temporal boundary between the early developing and ordinary mature phases at 2213: (a) horizontal cross-section of grayscale reflectivity at z = 3 km and bold black updraft contours beginning at 5 m s^{-1} with a contour interval of 10 m s^{-1} (due to the weak updrafts at this synthesis time no contours are evident in this frame), (b) horizontal cross-section of grayscale reflectivity at z = 8.5 km with bold black updraft contours beginning at 15 m s^{-1} with a contour interval of 15 m s^{-1} (again, no contours are evident in this frame due to the weak updrafts at this time), and (c) vertical cross-section of grayscale reflectivity at y = 53 km with bold black updraft contours beginning at 5 m s^{-1} with a contour interval of 10 m s^{-1}. All plots have storm-relative wind vectors overlaid.

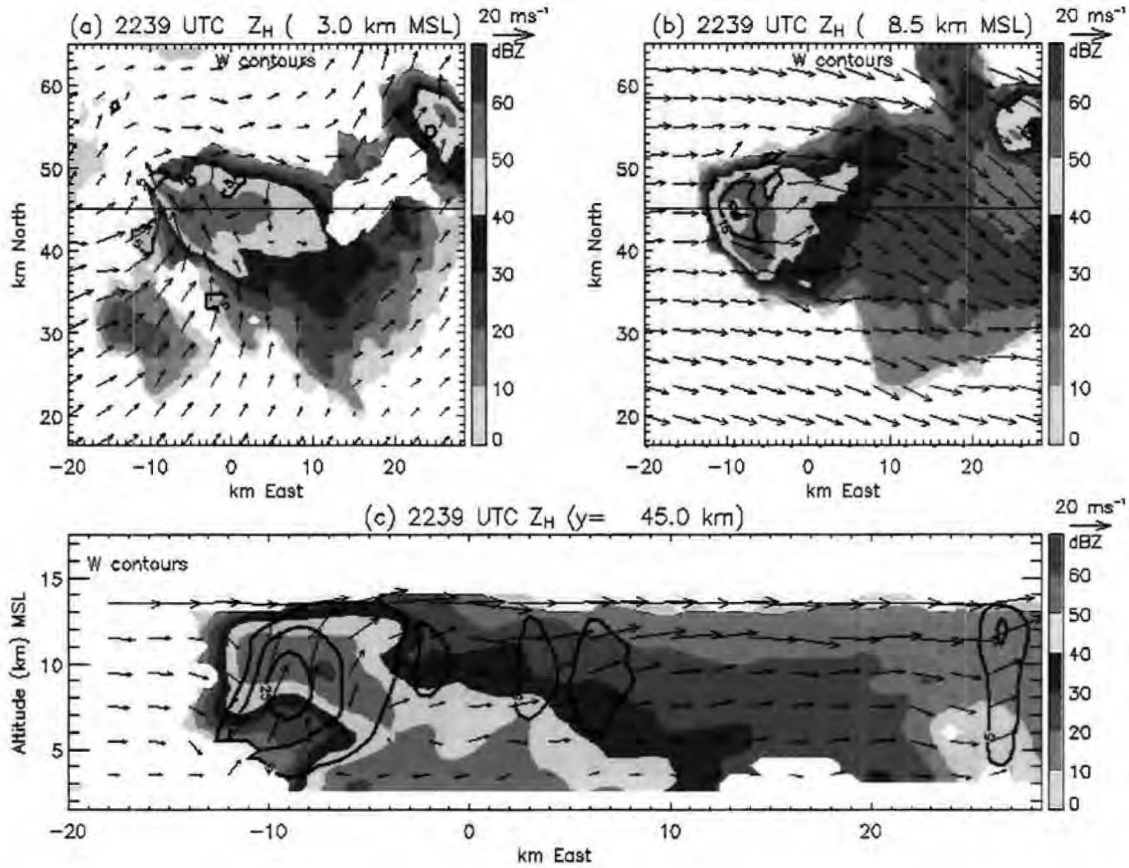

Figure 8. Same as Figure 7, except for synthesis showing the storm structure during the ordinary mature phase at 2239 and (c) y = 45 km.

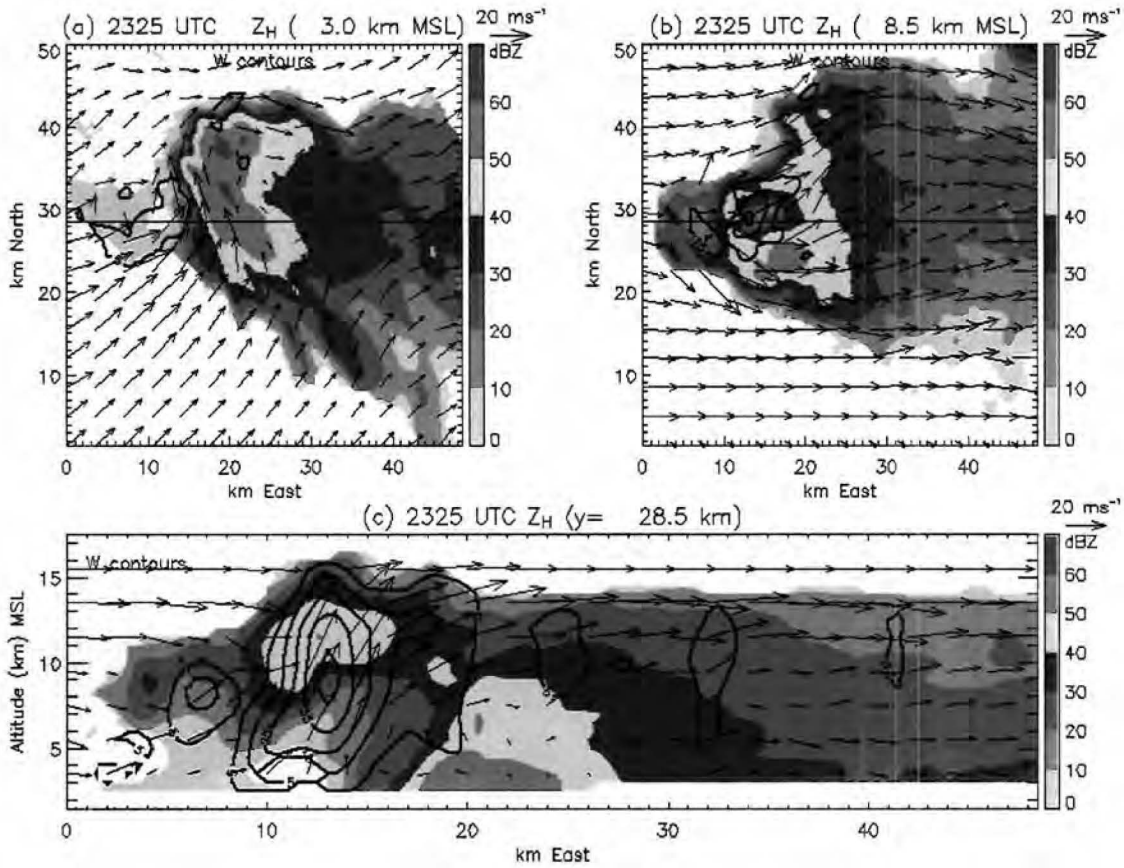

Figure 9. Same as Figure 7, except for synthesis representing the beginning of the tornadic period within the SR mature phase at 2325 and (c) y = 28.5 km.

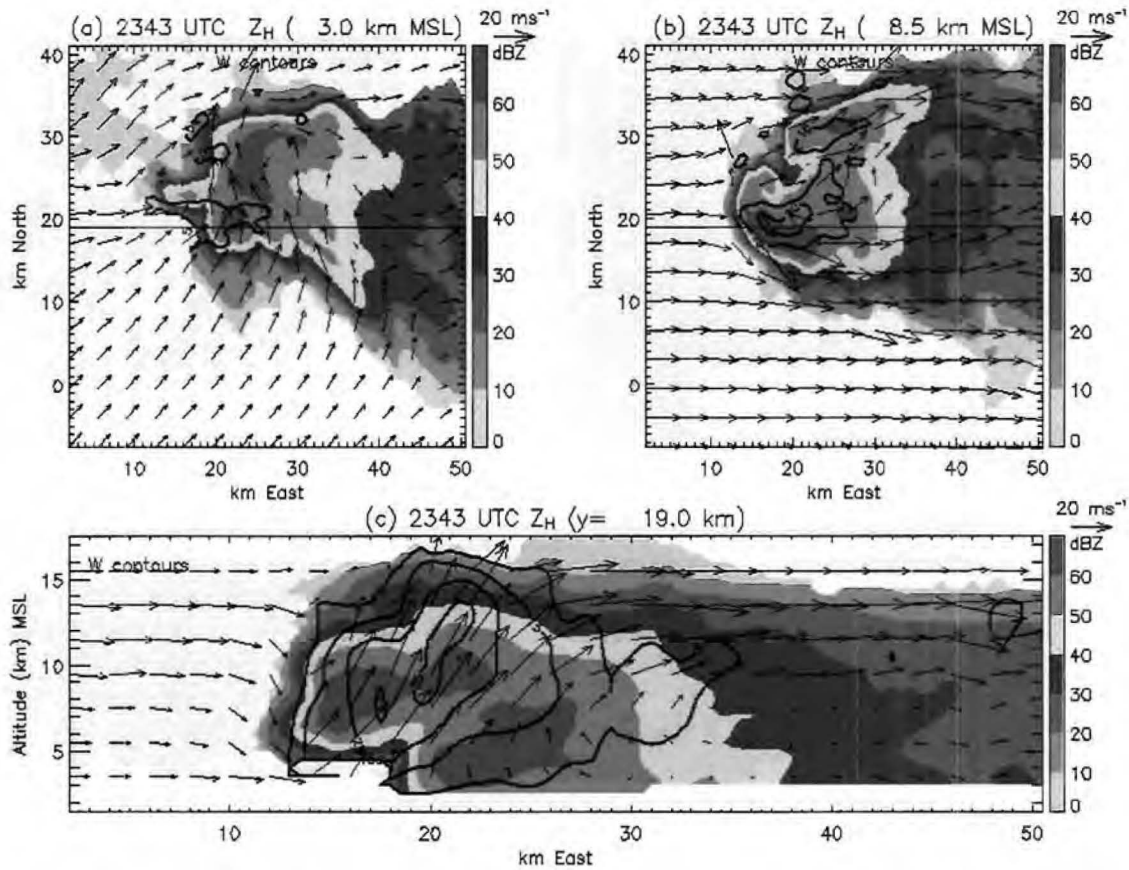

Figure 10. Same as Figure 7, except for synthesis illustrating the end of the tornadic period within the SR mature phase at 2343 and (c) y = 19 km.

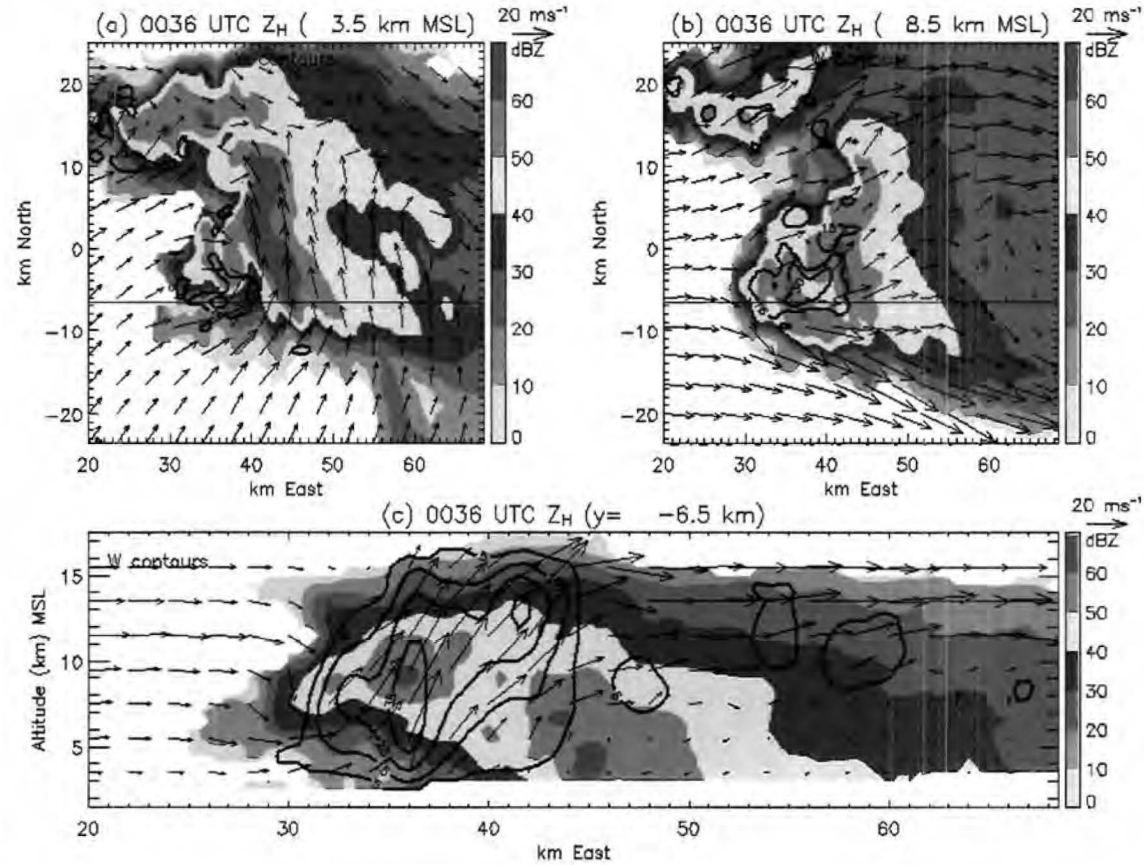

Figure 11. Same as Figure 7, except for synthesis representing the storm structure in the declining phase at 0036 and (a) z = 3.5 km and (c) y = −6.5 km.

CHAPTER 4

AIRFLOW AND HAIL GROWTH

4.1 Overview of airflow and radar echo structure

There are several features evident in the time-height contour plots of storm-wide maximum values and volumes associated with the updraft and vertical vorticity (Fig. 12) that are likely strong controls on the production of graupel and hail (Fig. 13). As seen in Fig. 12a, there are six distinct surges in updraft intensity that exceed 30-50 m s^{-1} and last for about 10-30 min. The last surge after 2357 and lasting some 40 min occurred during the "most steady" phase of the storm so we are counting it as only one surge even though there are two somewhat minor surges within it. The updraft intensity (maximum values in Fig. 12a) and volume (Fig. 12b) were located mostly at or above the 9-km level where the adiabatic liquid water content reached its maximum value, a region where hail should grow most rapidly but not necessarily reach its maximum size. The low- to midlevel right-flank cyclonic flow is evident in both the vorticity maxima (Fig. 12c) and in the volume of vorticity exceeding 10^{-2} s^{-1} after 2325 (Fig. 12d). The very earliest organizing phase of the storm is also evident in the low values of updraft and vorticity prior to about 2213.

In response to storm intensification as revealed in both the updraft and vorticity, reflectivity maxima (Fig. 13a) and volume (Fig. 13b) both increased while the storm echo top steadily rose. The graupel (total of low-density and high-density categories; Fig. 13c)

and hail (total of small and large categories; Fig. 13d) volumes deduced with the FHC algorithm show a similar behavior. It is noteworthy that increases in reflectivity volume (Fig. 13b) clearly follow the updraft surges. Since reflectivity must exceed 50 dBZ in the FHC algorithm for hail, the deduced hail echo volumes will also follow the updraft surges. Graupel production (Fig. 13c) also follows these trends.

4.2 Hail growth calculations

Particle growth calculations were made for ten sizes of starting embryonic particles (0.02, 0.05, 0.1, 0.2, 0.3, 0.4, 0.5, 0.6, 0.8, and 1.0 mm) spaced 1 km apart on a regular 80 km x 80 km horizontal grid, and with starting altitudes every 1 km from 4 to 12 km, for each of 31 synthesis times from 2130 29 June through 0036 30 June. Embryos were allowed to grow only from starting locations within the regular grid where there was some radar echo (Z_h >0 dBZ). Such an ensemble of particles was inserted into the flow at each of the 31 synthesis times, and allowed to grow over the next 35-40 min using winds from the initial and subsequent seven synthesis times. Winds used were ground-relative so that results to be presented represent time-resolved, ground-relative growth trajectories. The total mass of cloud liquid water swept out by each growing particle was determined at the end of each 10-sec time step and incorporated into an ever-increasing particle mass and diameter. Each particle was then advanced with winds interpolated to its current location and time after initialization along with a new fall speed calculated from the new diameter. This procedure continued along each trajectory until the growing particle either fell out (defined as reaching 3 km or lower in altitude) with at least a 2-mm diameter or reached the edge of the computation domain. The results,

therefore, also include precipitation particles that are smaller than hail (arbitrarily defined as any particle size ≥10 mm). Since melting with possible shedding of this melt-water are not accounted for in this simple growth model, particles that descend below the melting level (~5 km) cannot lose any mass.

We have somewhat arbitrarily separated calculated precipitation sizes that reach the ground into graupel (diameter <10 mm, the smaller of which will likely completely melt) and hail (diameter ≥10 mm) categories to be consistent with those defined in the FHC algorithm (Fig. 14). The overall trends in calculated graupel and hail growth are shown in Fig. 15 as time-height contour plots of the numbers of trajectory model grid points that satisfied the given size threshold at each height and time within 1-km grid boxes for the entire period when synthesized Doppler winds were available. These plots have been constructed in this way so that we can compare calculated growth with observed growth (Fig. 14). This approach also reveals how the calculated growth responded to the evolution of the storm's kinematic structure.

Both high-density and low-density graupel categories deduced with the FHC algorithm have been summed for presentation in Fig. 14a. Likewise, small and large hail have been summed and shown in Fig. 14b. These plots are similar to Fig. 13c-d, but now include melting to rain and drizzle and storm-wide trends in the growth model results for comparison. Based on the melting model presented in Pruppacher and Klett (1997), high-density graupel and small hailstones would completely melt after falling about 1.5 km below 0 °C (5 km). No graupel will survive past a 2-km descent, which corresponds to a temperature of about 15 °C. Ice particles smaller than 10 mm will completely melt within about a 2.5-km descent, which in this storm corresponds to a temperature of 18

°C. The FHC algorithm places more and more of the graupel and small hail categories into the rain category as precipitation descends, which can be seen in Fig. 14c. The drizzle that is included here comes mostly from the melting of small graupel and other ice particles outside the most active updraft region of the storm.

Results from the precipitation growth model are shown in Fig. 15. It is abundantly clear from these plots that the resolved Doppler wind fields were unable to produce even graupel-sized particles until after about 2148, ~18 minutes after initial radar detection of the storm. Further, no hail was produced until almost an hour (2227) after the storm was first detected. There are also obvious surges in the amounts of graupel and hail as demonstrated by the local maxima in the lower half of the storm, below about -10 °C. These surges from the growth model correspond quite well with those deduced from the FHC algorithm (Fig. 14).

Fallout locations for hail larger than 30 mm from the growth model were mostly confined to the area of radar reflectivity exceeding 55 dBZ (Fig. 16a). Virtually all of the modeled hail larger than 20 mm fell out along the left flank of the core updraft (Fig. 16b), especially just before the obvious right-turn of the storm at 2325.

Small embryonic particles that eventually fall out as hail originate mostly within the region surrounding the upstream and right flanks of the updraft (Fig. 17). This broad embryo source region (corresponding roughly to the embryo curtain of BF76) extends downward from the mid- to upper-level stagnation zone associated with obstacle flow and around the right flank of the updraft core. The base of the embryo source region in the low levels near cloud base is directly above the broad low-level inflow to the updraft. Since this "embryo corridor" (Nelson 1983) contains either weak updraft or downdraft,

most starting particles are able to descend to heights below the level of non-divergence of the updraft. As particles descend, the horizontally convergent flow in the lower part of the storm sweeps them toward the updraft core. Foote (1984) pointed to this horizontally convergent flow as the fundamental way by which updrafts can ingest small embryonic particles for growth to hail sizes.

There are essentially two growth paths that intermingle within the updraft core, one from the low-level inflow (Fig. 17) and one from the upwind stagnation zone (Fig. 18). The INFLOW path marked in Fig. 17 represents growth-from-scratch of small cloud droplets (~20-50 μm). These growing particles will arrive in the mid-levels and generally be smaller than ones (~mm-sizes) sedimenting around the right flank of the updraft from mid-levels (Fig. 18, RF) as they move cyclonically into the updraft core. Particles along this path will tend to be larger than ones from the low level INFLOW when the two growth paths cross.

Once growing particles pass through the updraft core, size-sorting along the anticyclonic path toward the left flank of the storm will occur, with larger particles descending first as they pass out of the core updraft and smaller particles staying in the S-shaped path (shown most clearly in Fig. 17) until they move farther to the right at which time they fall out. Early in the storm's evolution, when the vorticity was weaker and more confined on the right flank of the updraft maximum, these two colliding paths were much less pronounced. With time, the area and strength of right-flank cyclonic vorticity increased leading to more of the types of trajectories illustrated in Figs. 17 and 18, with bigger particles now tending to originate more toward the right flank and smaller

particles <10 mm continuing to originate along the INFLOW path and moving into the anticyclonic path aloft.

In order to find out how critical the sizes and magnitudes of updraft and vorticity were to the production of hail, we performed precipitation growth calculations assuming that each of the wind synthesis times represented a steady kinematic structure. This simplification was done so that results from precipitation growth could be more easily compared to the evolution of the synthesized winds. Histories of the percents of storm volume occupied by strong updraft (>10 m s^{-1}) and mesocyclonic-strength vertical vorticity (>10^{-2} s^{-1}) are compared with the resulting precipitation particle sizes from the growth model in Fig. 19.

It is quite clear from this analysis that hail larger than 10 mm can be grown in direct response to increases in updraft volume as seen at 2149 and 2159 (Fig. 19). However, these two small surges along with some of the other fluctuations seen in Fig. 19 should be considered as relatively minor when compared to the much more obvious increase following 2227. Continued increases in updraft volume after 2213 result in continued increases in the number of favorable trajectories leading to hail larger than 10 mm. However, it is noteworthy that hail larger than 20 mm also requires an increase in the volume of mesocyclonic-strength vorticity within the storm as seen by the increase in percent of favorable trajectories for this final size only after 2220. Cyclonically curved flow in the low- to mid-levels was found to be important in recycling sub- to near-mm particles from the upwind stagnation zone into the updraft for continued growth to hail sizes (see Fig. 17). If the updraft is bigger, more of these recycling trajectories are

favored to produce large hail. It is also evident in Fig. 19 that hail is grown at the expense of graupel as shown by the decline in trajectories favoring graupel after 2227.

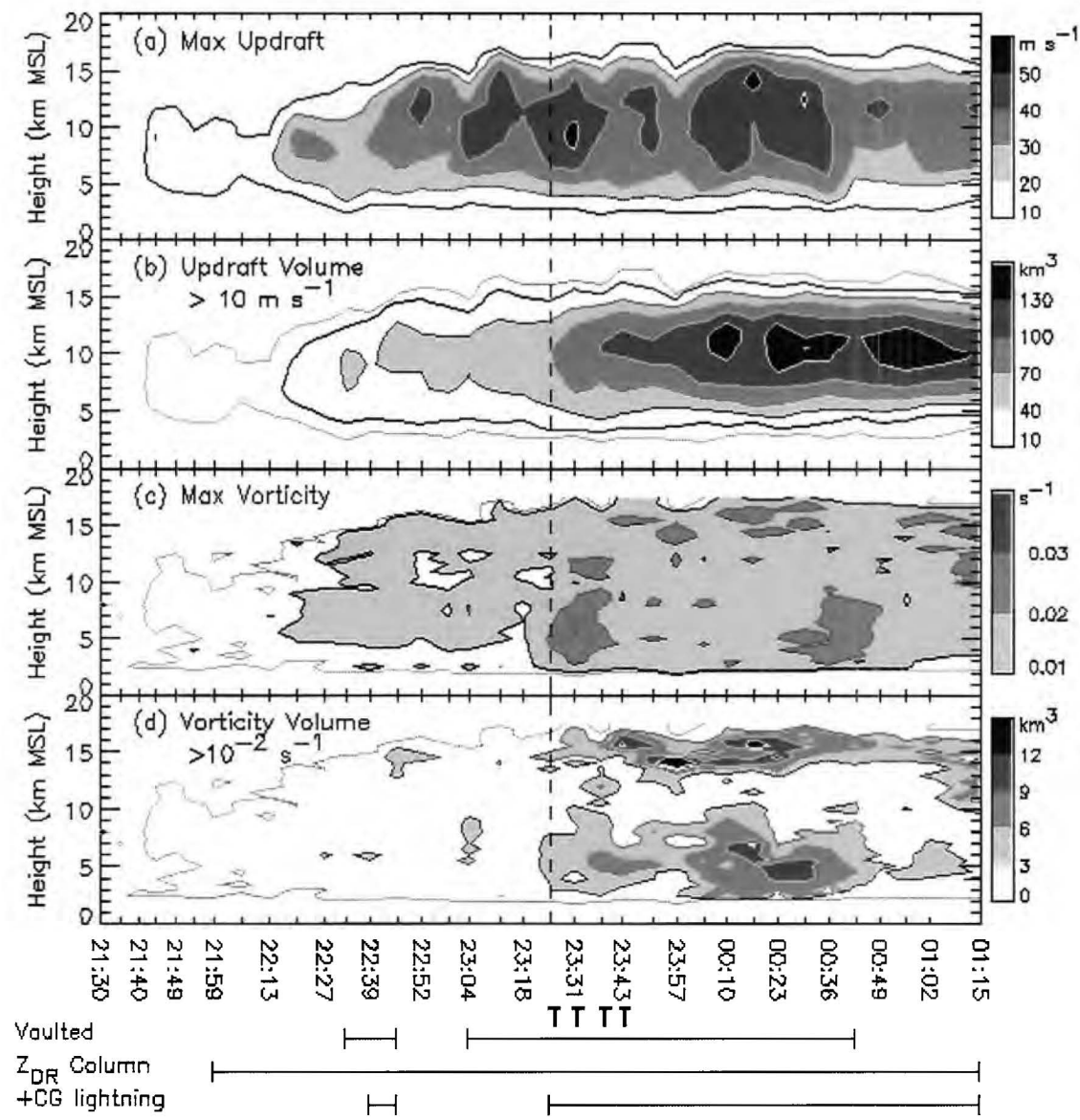

Figure 12. Time-height cross-sections of (a) maximum updraft (m s^{-1}), (b) updraft volume (km^3) greater than 10 m s^{-1}, (c) maximum vertical vorticity (s^{-1}), and (d) vertical vorticity volume (km^3) greater than 10^{-2} s^{-1}. A thick black line indicating the 10 m s^{-1} maximum updraft contour is overlaid in (b), and the 5 x 10^{-3} s^{-1} maximum vertical vorticity contour is overlaid in (c) and (d) for reference. The 'T' indicates the tornado was on ground at that time, and bars across the bottom of the plot indicate the times when the storm had a vaulted reflectivity structure, a Z_{dr} column of at least 2 dB in magnitude, and positive cloud-to-ground lightning. The vertical dashed line represents the time when the storm made its right turn.

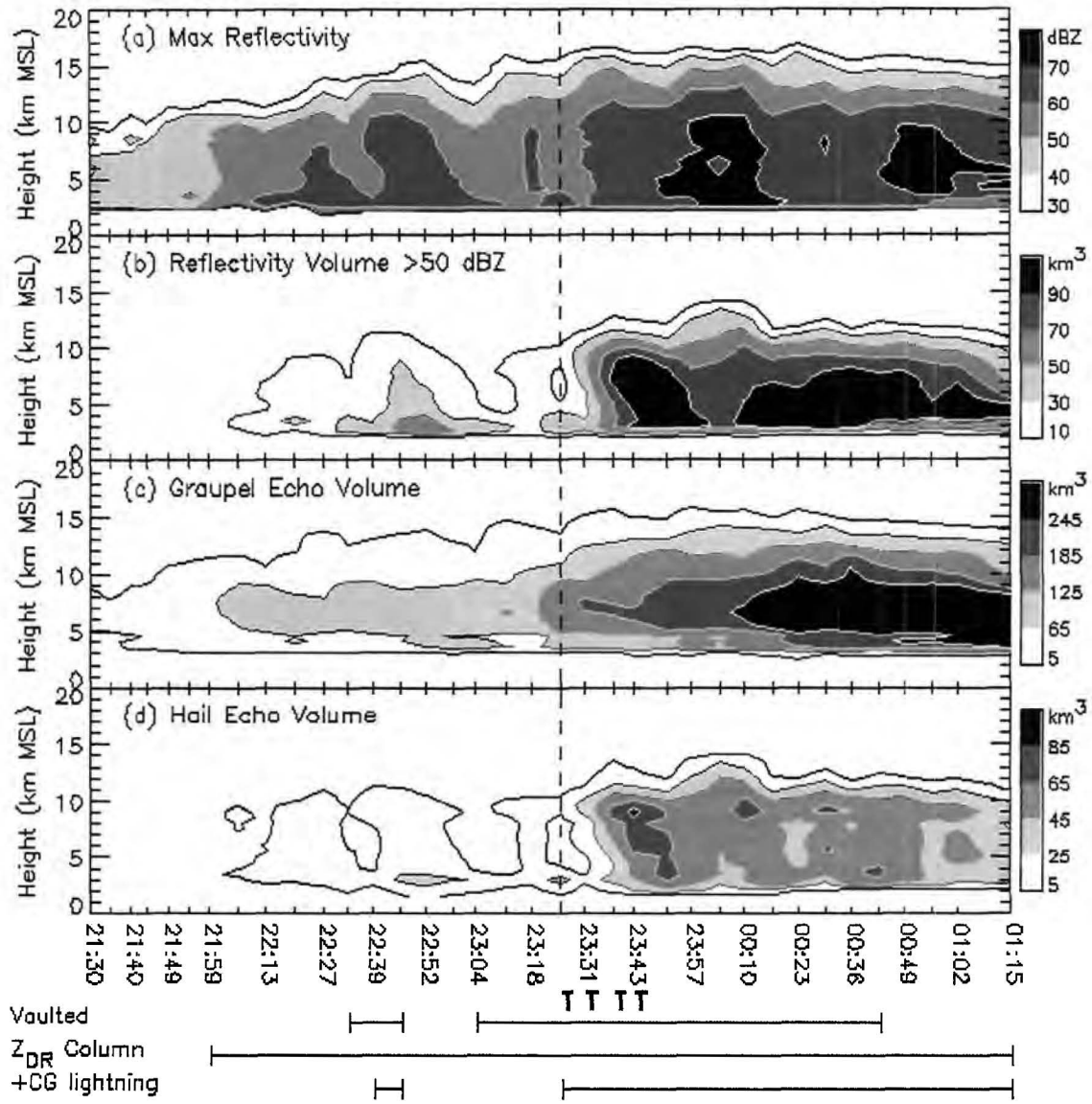

Figure 13. Same as Figure 12, except (a) maximum reflectivity (dBZ), (b) reflectivity volume (km^3) greater than 50 dBZ, (c) FHC total graupel (low-density + high-density) echo volume (km^3), contours beginning at 5 km^3 with a contour interval of 60 km^3, and (d) FHC total hail (small + large) echo volume (km^3), contours beginning at 5 km^3 with a contour interval of 20 km^3.

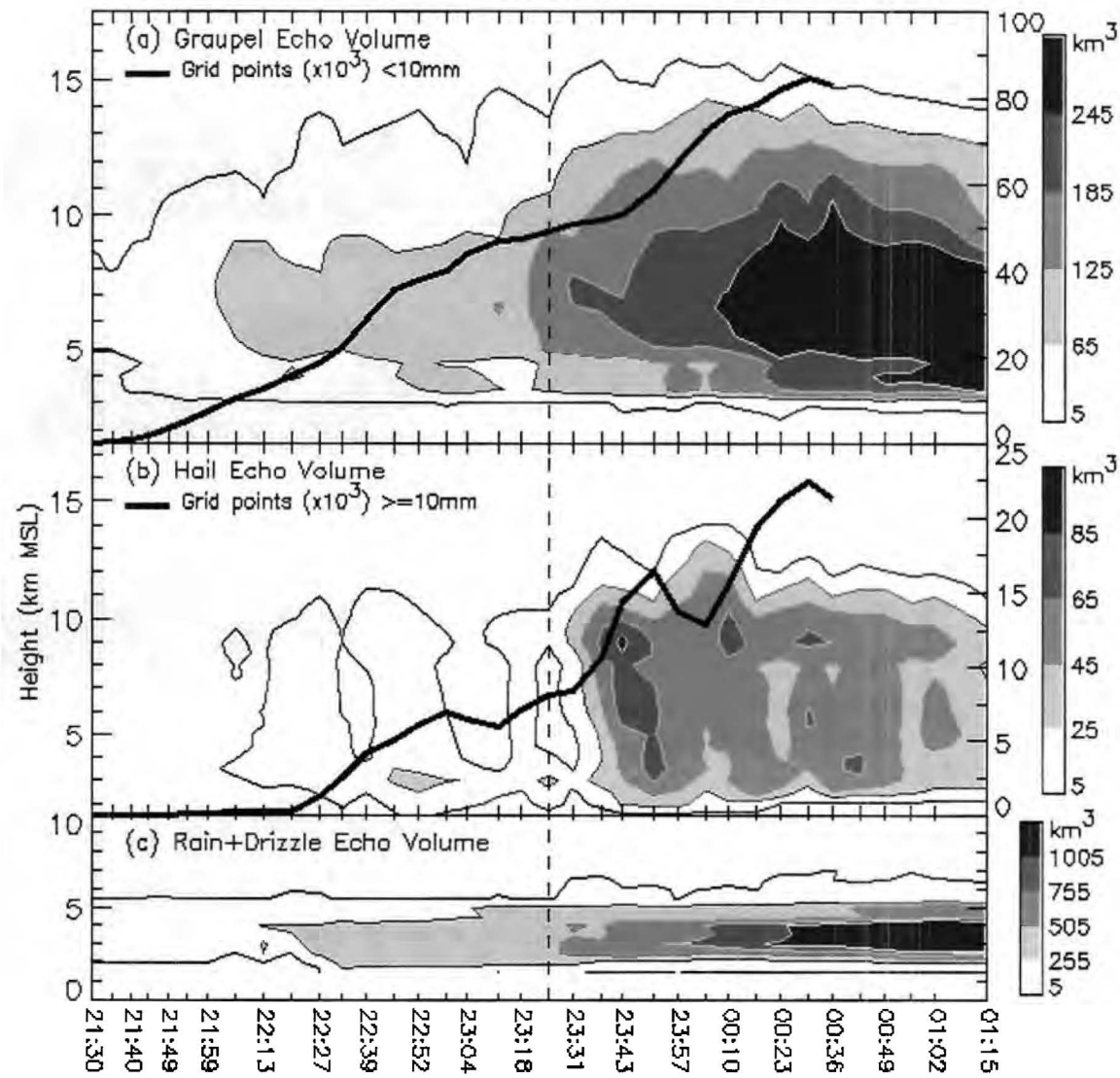

Figure 14. Time-height cross sections of (a) FHC total graupel (low-density + high-density) echo volume (km^3), contours beginning at 5 km^3 with a contour interval of 60 km^3, (b) FHC total hail (small + large) echo volume (km^3), contours beginning at 5 km^3 with a contour interval of 20 km^3, and (c) FHC rain and drizzle echo volume (km^3), contours beginning at 5 km^3 with a contour interval of 250 km^3. Height (km MSL) is denoted on the left axis in (a)-(c). A thick black line indicating the total number of graupel-producing (<10 mm) grid points (x10^3; see right axis) from the particle growth model at each time is overlaid onto (a), and a similar line indicating the number of hail-producing (≥ 10 mm) grid points (x10^3; see right axis) is overlaid onto (b). The particle growth model used Doppler-derived wind data until 0036.

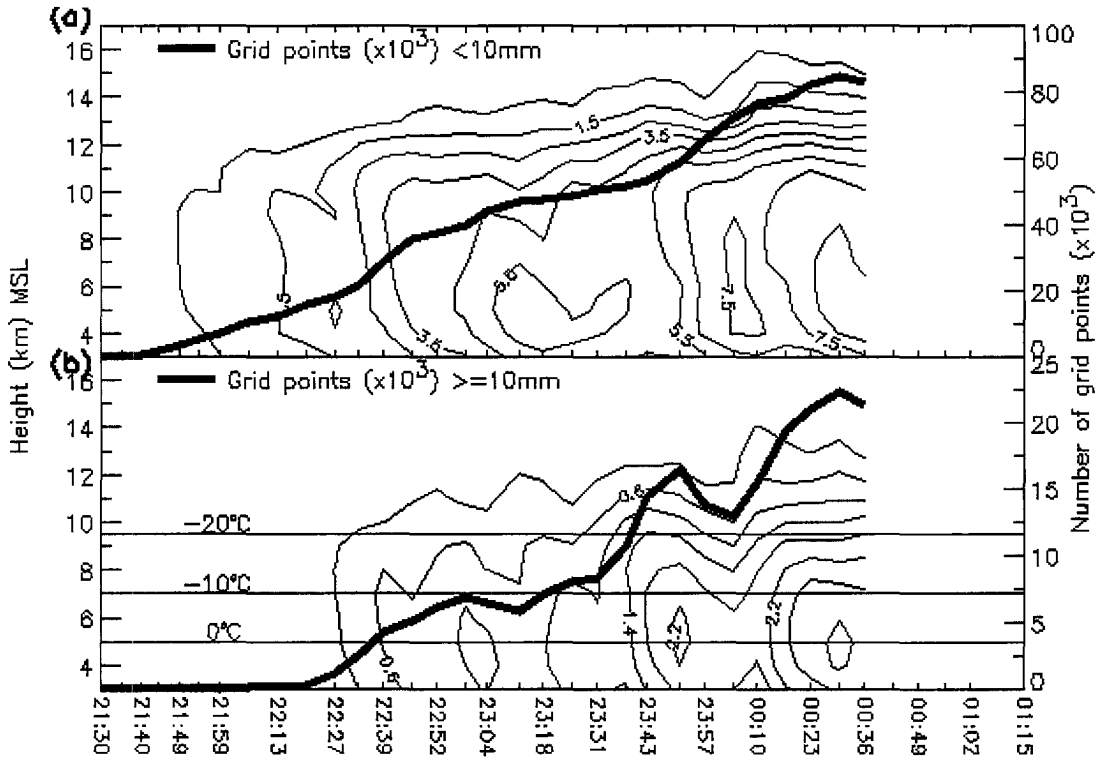

Figure 15. Time-height cross sections of the gridded particle growth model output to compare with Fig. 14. Contours represent the number of graupel-producing (<10 mm) grid points in (a) and the number of hail-producing (≥10 mm) grid points in (b) at each time and height. Contours in (a) begin at 0.5 x 10^3 and have a contour interval of 1.0 x 10^3, and in (b) they begin at 0.2 x $10^3$and have a contour interval of 0.4 x 10^3. The thick black lines overlaid are the same as those in panels (a) and (b) of Fig. 14. Isotherms are overlaid in (b) to highlight the 0 °C, -10 °C, and -20 °C levels.

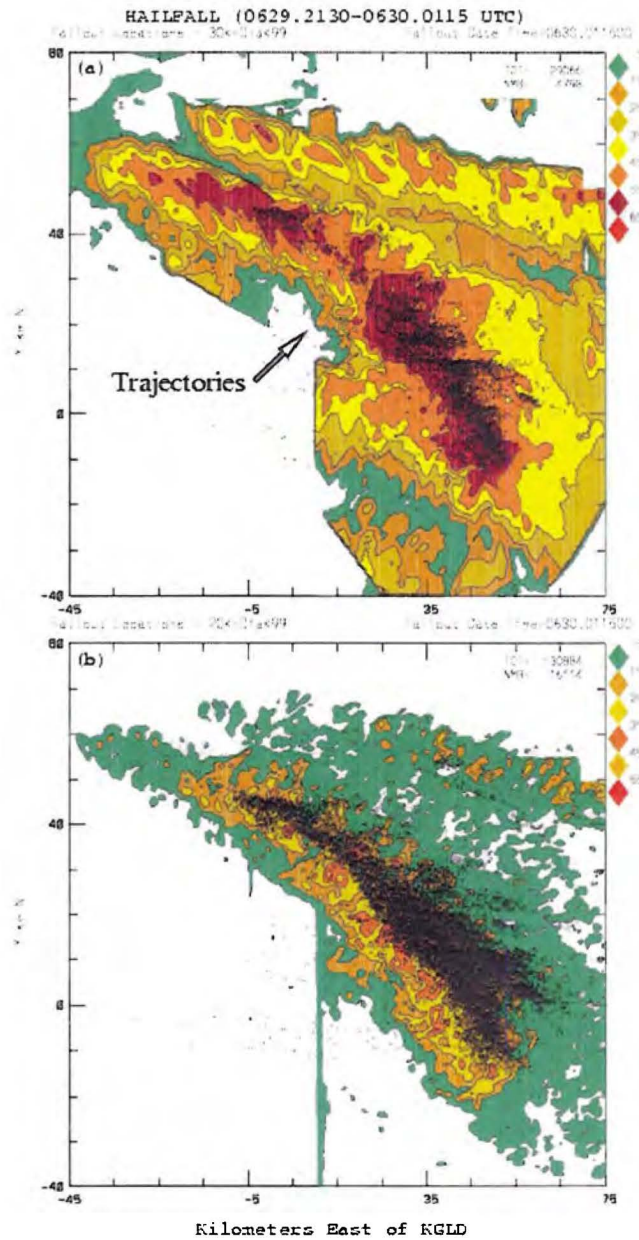

Figure 16. Swaths of maximum in the vertical column (a) KGLD reflectivity (dBZ), (b) updraft (m s^{-1}) for the period 2130-0115 UTC with particle growth model hailfall overlaid as black dots. Modeled hailfall with sizes greater than 30 mm (rather than 20 mm to reduce the number of fallout points so that the underlying reflectivity structure is visible) are overlaid in (a) and greater than 20 mm in (b). The trajectories shown in Figs. 17-18 are from the area highlighted in (a).

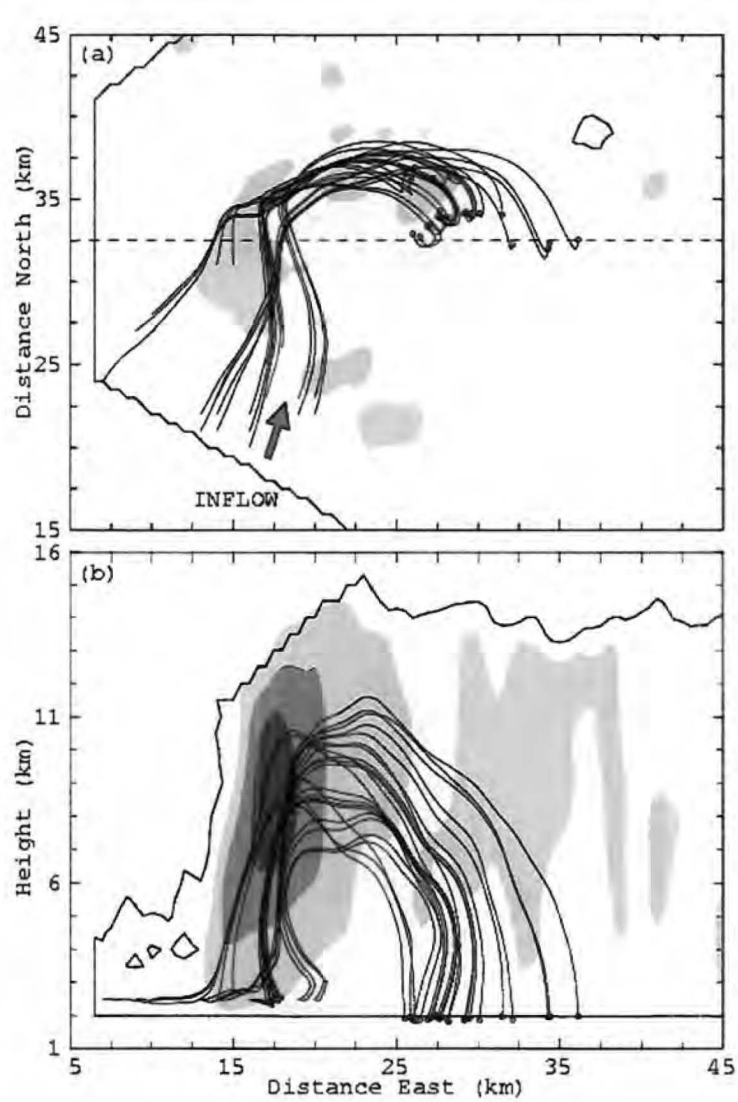

Figure 17. Representative hail growth trajectories from embryonic particles (20 μm diameter) started at 2.5 km near cloud base. Trajectories leading to hail (diameter ≥10 mm) that falls out below 2 km are overlaid onto (a) horizontal (z=2.5 km) and (b) vertical (y=32.5 km) sections of vertical air motion. The grayscale contours of vertical motion are 2, 12, and 22 m s^{-1}. The black contour line represents -10 dBZ.

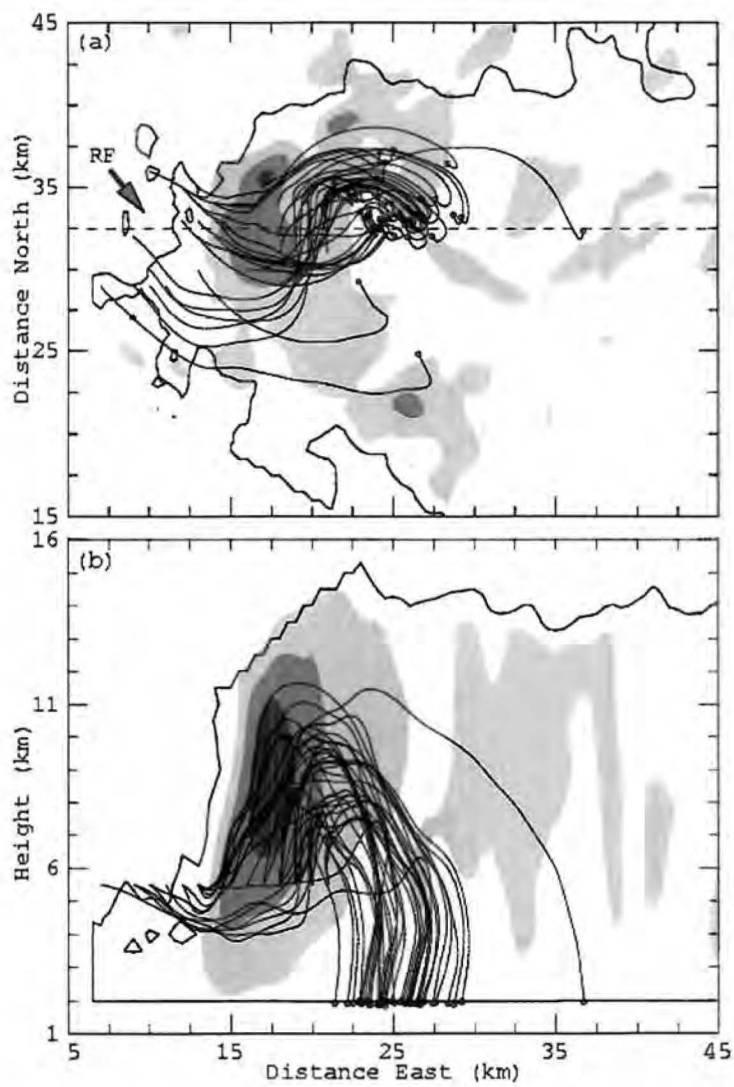

Figure 18. Same as Fig. 17 except for (a) horizontal (z=5.5 km) section and embryonic particles (100 μm diameter) started at 5.5 km.

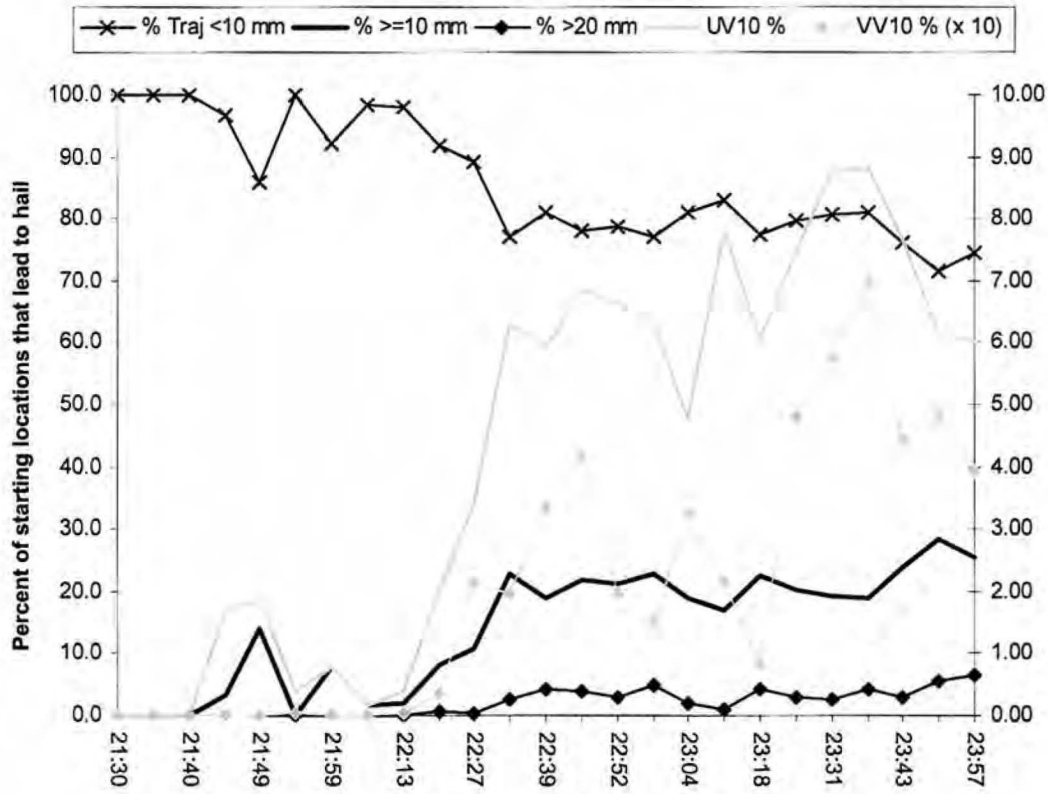

Figure 19. Time series summarizing normalized updraft >10 m s^{-1} volume (UV10), and normalized vertical vorticity >10 x 10^{-3} s^{-1} volume (VV10, multiplied by factor of 10 for graphical purposes) in gray on the right axis, and the percent of starting trajectories in the particle growth model that grew to diameters <10 mm, ≥10 mm, and >20 mm in black on the left axis.

CHAPTER 5

SUMMARY

This well-observed severe storm has given us the opportunity to study in some detail the kinematic and microphysical evolution from its earliest developing phase through its mature and dissipating phases. The developing phase was important not only in organizing the storm upscale from its initial multicellular structure to one more commonly associated with steady, intense supercells but also in allowing enough time for the storm to produce an ample supply of embryonic particles for future graupel and hail production. The storm slowly grew in size and intensity until large areas of strong updraft (>10 m s^{-1}) and mesocyclonic-strength vorticity were present. This supercellular structure with strong cyclonically curving flow in the low- to mid-levels around the right flank of the updraft core made it possible for graupel and hail to be readily grown through a recycling of particles which had initially grown to near mm-sizes in their first pass through the updraft. Polarimetric radar observations indicated the presence of liquid water drops as large as 6 mm entering the updraft in locations where they could easily grow into large hail. Elevated LDR caps on top of the Z_{dr} columns further support the notion of large drops being carried aloft and freezing.

Several surges in the updraft were observed to be superimposed upon the more steady, broadscale flow field associated with the SR mature (Browning 1964), or supercellular, phase. These surges persisted for the 20-min periods typical of smaller

convective cells such as described by Byers and Braham (1949). A time of 20 min is about how long it takes for a convective bubble to rise to its level of neutral buoyancy and the precipitation produced along the way to fall out. Each of these updraft surges was accompanied by surges in the observed reflectivity (graupel and hail) as well as lightning activity, particularly +CG strikes. We can only speculate on the likely causes of these updraft surges. The reflectivity surges led to increased rainout into intruding mid-level air, which in turn could modulate low-level cold pool production and outflow. These modulations, if present, could then feedback on the amount of low-level convergence along the leading edge of the expanding outflow, and thus modulate the updraft. It is extremely difficult to observe this kind of feedback so its exact details can only be revealed with fully four-dimensional, high-resolution numerical models.

The exact processes that lead to near-mm to mm-sized embryonic particles large enough to grow to hail cannot be accurately diagnosed with the resolved Doppler winds. Therefore, it has been customary in studies of hail growth (e.g. Nelson 1983, Foote 1984) to assume that near-mm to mm-sized embryos exist throughout the storm volume and then to determine where in the storm these particles are most likely to continue growing to hail sizes.

We found that if near-mm to mm-sized embryonic particles find their way into the updraft, their growth rates are usually fast enough that they can achieve hail sizes and fallout before passing through the layer of high cloud liquid water. However, even if very small (10s of micron diameters) particles somehow got into the main updraft, they experienced rather slow growth rates because they tend not to sweep out and collect much cloud water because of their relatively small cross-sectional areas. When the

updraft was fairly intense, approximately >10 m s^{-1}, these small particles were carried upward so fast that they did not have enough time to grow to hail sizes and were simply exhausted into the anvil.

One of the most important aspects of the flow in this storm for the production of large hail was the presence of cyclonic flow in low- to mid-levels and on the right flank of the updraft. It appears that this horizontal flow was very efficient in bringing embryonic particles into the main updraft for continued growth. However, there must be sufficient curvature in the flow so that particles are swept into the updraft before they are carried too far downstream from the updraft core.

Most of the air that entered the main updraft core from low levels experienced rapid ascent and was exhausted into the anvil at and above about 13 km. Some updraft air was detrained in midlevels into the downstream region of weaker reflectivities east of the core. Also there were some small areas of downdraft in the low levels on the west side of the core, but there was no midlevel inflow of environmental air into any sort of well-organized downdraft. Cyclonic flow around the storm's right flank in the lowest levels carried air from the low level region of weak echo into the main inflow path. At higher levels this cyclonic flow carried air directly into the updraft core. Environmental air also streamed around the updraft perimeter in mid- to upper-levels and beneath the anvil outflow and detrained some air from the weaker updraft perimeter. This air stream was essentially outside the dividing streamline between air within the updraft core and horizontal flow that stays essentially at the same altitude as it flows around the updraft core. This was especially true above the level where the updraft became divergent. Foote (1984) pointed to the convergent nature of the updraft in low levels and its

divergent nature in the higher levels as the basic way air and mm-sized precipitation particles move toward and away from the updraft core.

We found that graupel and small hail could be grown from scratch from cloud droplet nucleation at cloud base, followed by freezing and continued growth aloft. However, particles smaller than a few mm were mostly exhausted into the eastward streaming anvil once the updraft strengthened during the mature phase. We were unable to demonstrate that the early horizontal flow out of the diverging updraft aloft did indeed carry any of these near-mm sized particles westward from the updraft core. Reflectivity values around the west (upwind) side of the mid- to upper-level, early updraft were near –10 dBZ, which is much higher than might be expected if the radar echo was composed solely of small ice crystals and frozen cloud droplets with sizes of a few 10s of microns. As the storm expanded in the mid- to upper-levels, the likelihood of some mm-sized particles passing westward became more certain, likely a result of unresolved motions not present in the Doppler-derived winds.

The observed onsets of positive CG lightning and large hail as deduced with the hydrometeor identification algorithm and diagnosed with the precipitation growth model were essentially coincident in time. Trends in both hail echo volumes and positive CG lightning were found to closely follow the updraft surges, which is discussed in more detail in Wiens et al. (2005). Additionally, maxima in hail echo volume as measured by both the FHC and the particle growth model, resided between the melting level and the -10° C level (5-7 km MSL) of the storm.

CHAPTER 6

CONCLUSIONS

This study has shown that hail embryos can come from a much broader region than the so-called embryo curtain (BF76) as previously suggested by Nelson (1983). Smaller cells were observed upstream of the low-level inflow at two or three different times, and could have contributed more embryonic particles that would have affected graupel and hail production. Our findings are also very consistent with Foote's (1984) supposition that horizontally converging flow below the updraft maximum is the basic injection mechanism for transporting embryos into the updraft.

From the precipitation growth calculations, we have outlined four basic conditions that must be met in order for the storm to produce (large) hail: (1) small near-mm to mm-sized embryonic particles must be present, (2) there must be a mechanism for transporting these particles into the updraft, (3) the updraft must be of sufficient size and intensity to grow these embryonic particles into hail, and (4) the horizontal winds must keep the growing particles within favored hail growth conditions. In particular, strong updraft (>10 m s^{-1}) within a large fraction of the storm was required to produce any hail. A large region of cyclonically curved flow around the right flank of this updraft was apparently critical for the production of any hail larger than 20 mm. We conclude that if these kinematic features are not present, a storm can only produce graupel particles with little or no hail.

REFERENCES

Bringi, V.N., and V. Chandrasekar, 2000: Polarimetric Doppler Weather Radar: Principles and Applications, Cambridge University Press, Cambridge, United Kingdom, 636 pp.

Bringi, V.N., K. Knupp, A. Detwiler, L. Liu, I.J. Caylor, and R.A. Black, 1997: Evolution of a Florida thunderstorm during the Convection and Precipitation/Electrification Experiment: The case of 9 August 1991. *Mon. Wea. Rev.*, ***135***, 2131-2160.

Browning, K.A., 1964: Airflow and precipitation trajectories within severe local storms which travel to the right of the winds. *J. Atmos. Sci.*, **21**, 634-639.

Browning K.A., 1977: The structure and mechanisms of hailstorms. *Hail: A Review of Hail Science and Hail Suppression,* G.B. Foote and C.A. Knight, Eds., *Meteor. Monogr.,* No. 38, , Amer. Meteor. Soc., 1-43.

Browning, K.A., and G.B. Foote, 1976: Airflow and hail growth in supercell storms and some implications for hail suppression. *Quart. J. Roy. Meteor. Soc.*, **102**, 499-533.

Byers, H.R., and R.R. Braham, 1949: *The Thunderstorm.* U.S. Gov't Printing Office, Washington D.C., 287 pp. [NTIS PB-234-515.]

Carey, L.D., and S.A. Rutledge, 1996: A multiparameter radar case study of the microphysical and kinematic evolution of a lightning producing storm. *Meteorol. Atmos. Phys.*, **59**, 33-64.

Carey, L.D. and S.A. Rutledge, 1998: Electrical and multiparameter radar observations of a severe hailstorm. *J. Geophys. Res.*, **103**, 13,979-14,000.

Carey, L. D. and S. A. Rutledge, 2000: The Relationship Between Precipitation & Lightning in Tropical Island Convection: A C-band Polarimetric Radar Study. *Mon. Wea. Rev.*, **128**, 2687-2710.

Carey, L.D., S.A. Rutledge, D.A. Ahijevych, and T.D. Keenan, 2000: Correcting Propagation Effects in C-band Polarimetric Radar Observations of Tropical Convection Using Differential Propagation Phase. *J. Appl. Meteor.*, **39**, 1405-1433.

Cifelli, R. W.A. Petersen, L.D. Carey, and S.A. Rutledge, 2002: Radar Observations of the Kinematic, Microphysical, and Precipitation Characteristics of Two MCSs in TRMM-LBA. *J. Geophys. Res*, **29(10)**, 10.1029/2000JD0000264.

Conway, J.W., and D.S. Zrnic, 1993: A study of embryo production and hail growth using dual-Doppler and multiparameter radars. *Mon. Wea. Rev.*, **121**, 2511-2528.

Cummins, K. L., M. J. Murphy, E. A. Bardo, W. L. Hiscox, R. B. Pyle, and A. E. Pifer, 1998: A combined TOA/MDF technology upgrade of the U.S. National Lightning Detection Network. *J. Geophys. Res.*, **103** (D8), 9035–9044.

Doviak, R. J., and D. S. Zrnic, 1993: Doppler Radar and Weather Observations, 2nd Ed., Academic Press, San Diego, California, 562 pp.

Dye, J.E., B.E. Martner, and L.J. Miller, 1983: Dynamical-microphysical evolution of a convective storm in a weakly-sheared environment. Part I: Microphysical observations and interpretation. *J. Atmos. Sci.*, **40**, 2083-2096.

Foote, G.B., 1984: A study of hail growth utilizing observed storm conditions. *J. Climate Appl. Meteor.*, **23**, 84-101.

Foote, G.B., and H. W. Frank, 1983: Case study of a hailstorm in Colorado. Part III: Airflow from triple Doppler measurements. *J. Atmos. Sci.,* **40**, 686-707.

Gal-Chen, T., 1982: Errors in fixed and moving frames of reference. Applications for conventional and Doppler radar analysis. *J. Atmos. Sci.*, **39**, 2279-2300.

Hall, M.P.M., J.W.F. Goddard, and S.M. Cherry, 1984: Identification of hydrometeors and other targets by dual-polarization radar. *Radio Sci.*, **19**, 132-140.

Herzegh, P.H., and A.R. Jameson, 1992: Observing precipitation through dual-polarization radar measurements. *Bull. Amer. Meteor. Soc.*, **73**, 1365-1374.

Hubbert, J., and V.N. Bringi, 1995: An iterative filtering technique for the analysis of copolar differential phase and dual-frequency radar measurements. *J. Atmos. Oceanic Technol.,* **12**, 643-648.

Hubbert, J., V.N. Bringi, L.D. Carey and S. Bolen, 1998: CSU-CHILL polarimetric radar measurements from a severe hail storm in eastern Colorado. *J. Appl. Meteor.*, **37**, 749–775.

Illingworth, A.J., J.W.F. Goddard, and S.M. Cherry, 1987: Polarization radar studies of precipitation development in convective storms. *Quart. J. Roy. Meteor. Soc.*, **113**, 469-489.

Klemp, J.B., R.B. Wilhelmson, and P.S. Ray, 1981: Observed and numerically simulated structure of a mature supercell thunderstorm. *J. Atmos. Sci.*, **38**, 1558-1580.

Knight, C.A., and N.C. Knight, 1973: Hailstone embryos and hailstone models. *Preprints, 8th Conf. Severe Local Storms*, Amer. Meteor. Soc., Boston, 77-79.

Knight, C.A., and K. Knupp, 1986: Precipitation growth trajectories in a CCOPE storm. *J. Atmos. Sci.*, **43**, 1057-1073.

Lang, T.J., and Coauthors, 2004: The Severe Thunderstorm Electrification and Precipitation Study. *Bull. Amer. Meteor. Soc.*, **85**, 1107-1125.

Liu, H., and V. Chandrasekar, 2000: Classification of hydrometeors based on polarimetric radar measurements: Development of fuzzy logic and neuro-fuzzy systems and in situ verification. *J. Atmos. Oceanic Technol.*, **17**, 140-164.

Miller, L.J., J.E. Dye, and B.E. Martner, 1983: Dynamical-microphysical evolution of a convective storm in a weakly-sheared environment. Part II: Airflow and precipitation trajectories from Doppler radar observations. *J. Atmos. Sci.*, **40**, 2097-2109.

Miller, L.J., C.G. Mohr, and A.J. Weinheimer, 1986: The simple rectification to Cartesian space of folded radial velocities from Doppler radar sampling. *J. Atmos. Oceanic. Technol.*, **3**, 162-174.

Miller, L.J., J.D. Tuttle, and C.K. Knight, 1988: Airflow and hail growth in a severe northern High Plains supercell. *J. Atmos. Sci.*, **45**, 736-762.

Miller, L.J., J.D. Tuttle, and G.B. Foote, 1990: Precipitation production in a large Montana hailstorm: Airflow and particle growth trajectories. *J. Atmos. Sci.*, **47**, 1619-1646.

Mohr, C.G., and R.L. Vaughn, 1979: An economical approach for Cartesian interpolation and display of reflectivity factor data in three-dimensional space. *J. Appl. Meteor.*, **18**, 661-670.

Mohr, C.G., L.J. Miller, R.L. Vaughn, and H.W. Frank, 1986: On the merger of mesoscale data sets into a common Cartesian format for efficient and systematic analysis. *J. Atmos. Oceanic. Technol.*, **3**, 143-161.

Moller, A.R., C.A. Doswell III, M.P. Foster, and G.R. Woodall, 1994: The operational recognition of supercell thunderstorm environments and storm structures. *Wea. Forecasting*, **9**, 327-347.

Nelson, S.P., 1983: The influence of storm flow structure on hail growth. *J. Atmos. Sci.*, **40**, 1965-1983.

Nelson, S.P.,1987: The hybrid multicellular-supercellular storm—an efficient hail producer. Part II: General characteristics and implications for hail growth. *J. Atmos. Sci.*, **44**, 2060-2073.

O'Brien, J.J., 1970: Alternative solutions to the classical vertical velocity problem. *J. Appl. Meteor.*, **9**, 197-203.

Pruppacher, H.R., and J.D. Klett, 1997: *Microphysics of Clouds and Precipitation.* Kluwer Academic, 954 pp.

Rotunno, R., and J.B. Klemp, 1982: The influence of the shear-induced pressure gradient on thunderstorm motion. *Mon. Wea. Rev.*, **110**, 136-151.

Rust, W.D., and D.R. MacGorman, 2002: Possibly inverted-polarity electrical structure in thunderstorms. *Geophys. Res. Lett.,* **29**, paper 10.1029/2001GL014303.

Ryzhkov, A.V. and D.S. Zrnic, 1998: Polarimetric rainfall estimation in the presence of anomalous propagation. *J. Atmos. Oceanic Technol.*, **15**, 1320-1330.

Smith, P.L., D.J. Musil, A.G. Detwiler, and R. Ramachandran, 1999: Observations of mixed-phase precipitation within a CaPE thunderstorm. *J. Appl. Meteor.*, **38**, 145-155.

Straka, J.M., D.S. Zrnic, and A.V. Ryzhkov, 2000: Bulk hydrometeor classification and quantification using polarimetric radar data: Synthesis of relations. *J. Appl. Meteor.*, **39**, 1341-1372.

Straka, J.M., E.N. Rasmussen, and S.E. Fredrickson, 1996: A mobile mesonet for finescale meteorological observations. *J. Atmos. Oceanic Technol.,* **13**, 921–936.

Wakimoto, R.M., and V.N. Bringi, 1988: Dual-polarization observations of microbursts associated with intense convection: The 20 July storm during the MIST project. *Mon. Wea. Rev.*, **116**, 1521–1539.

Weisman, M.L., and L.J. Miller, 2000: An overview of the severe thunderstorm electrification and precipitation study (STEPS). *Preprints, 20th Conf. Severe Local Storms*, Orlando, FL, Amer. Meteor. Soc., 654-656.

Wiens, K.C., S.A Rutledge, and S.A. Tessendorf, 2005: The 29 June 2000 supercell observed during STEPS. Part II: Lightning and charge structure. *J. Atmos. Sci.*, **62**, 4151-4177.

Williams E.R., 2001: The electrification of severe storms. *Severe Convective Storms*, C.A. Doswell, III, Ed., *Meteor. Monogr.*, No. 50, Amer. Meteor. Soc., 527-561.

PART II: RADAR AND LIGHTNING OBSERVATIONS OF AN INVERTED STORM OBSERVED DURING STEPS

CHAPTER 1

INTRODUCTION

Based on cloud-to-ground (CG) lightning climatologies, CG lightning lowering negative charge to the ground is far more common than positive CG lightning across the majority of the U.S. However, storms dominated (> 50%) by CG lightning that lower *positive* charge to ground are indeed observed, and appear to be most frequent in the High Plains of the U.S. (Orville and Huffines 2001, Carey and Rutledge 2003). The charge structure typically associated with storms producing negative CG lightning is often referred to as a 'normal' tripole, consisting of a main midlevel negative charge region below an upper-level positive charge layer, with a small lower positive charge layer below the negative region (Simpson and Scrase 1937).

While several hypotheses have emerged to explain the possible charge structure of positive CG-dominated storms (Brook et al. 1982, Seimon 1993, Carey and Rutledge 1998, Lang and Rutledge 2002), few studies have had three-dimensional lightning observations available to interpret internal charge structure. Hence, the Severe Thunderstorm Electrification and Precipitation Study (STEPS; Lang et al. 2004) was established. The STEPS field campaign took place between 17 May 2000 and 20 July 2000 in eastern Colorado and western Kansas. A goal of the STEPS campaign is to identify relationships between microphysics, dynamics and electrification in severe storms on the High Plains, and in particular, to investigate positive CG lightning

production. An unprecedented network of observing systems was deployed (see Lang et al. 2004 for a complete listing), including two dual-polarization Doppler radars and a three-dimensional Lightning Mapping Array (LMA; Rison et al. 1999).

In addition to the lack of three-dimensional charge structure observations as support, the positive CG charge structure hypotheses, such as the tilted dipole or inverted dipole (outlined in detail in Williams 2001), do not include a lower negative charge layer below the lowest positive charge region. For negative CG lightning, however, Williams et al. (1989) suggested that the lower positive charge layer of the normal tripole was required. Via model simulations of storm electrification, Mansell et al. (2002, 2005) also noted that lower *negative* charge regions may be necessary for *positive* CG flashes. Alternatively, studies of storms with low CG flash rates have suggested an 'elevated charge' mechanism, which implies as a storm kinematically intensifies its main charge dipole is lofted to higher altitudes, which enhances intra-cloud (IC) lightning while depressing CG flash rates (MacGorman et al. 1989, Lang et al. 2000, Lang and Rutledge 2002).

Several studies have already emerged from the STEPS dataset, primarily on the 29 June 2000 supercell that produced predominantly positive CG lightning (MacGorman et al. 2005, Tessendorf et al. 2005, Wiens et al. 2005, Kuhlman et al. 2006). The goal of this study is to document properties of a STEPS storm in which CG flashes were *not* detected, to be used as comparison to the other cases in which CGs were observed. By studying a broad spectrum of cases we hope to learn more about why some storms produce anomalous positive CG lightning.

On 3 June 2000, an isolated cell was observed in the far northeastern extent of the STEPS radar network between 2210 UTC[7] (3 June) and 0121 (4 June). It produced 2-cm hail and moderate IC lightning. Again, no CGs of either polarity were observed by the National Lightning Detection Network (NLDN). This study provides a discussion of the kinematic, microphysical, and electrical properties that characterized the 3 June storm.

[7] All times hereafter will be in UTC.

CHAPTER 2

DATA AND METHODS

2.1 Radar data and processing

Three S-band radars, the Colorado State University (CSU)-University of Chicago and Illinois State Water Survey (CHILL) polarimetric Doppler radar, the National Center for Atmospheric Research (NCAR) S-Pol polarimetric Doppler radar, and the Goodland, Kansas National Weather Service (NWS) WSR-88D radar (KGLD), comprised the triple-Doppler radar network. The three radars were arranged in a nearly equilateral triangle with approximately 60-km sides (Tessendorf et al. 2005; their Fig. 1).

Wind field syntheses were completed for 25 volume scans during the period 2301 (3 June)-0121 (4 June)[8]. The radar data were interpolated onto a Cartesian grid with 0.5 km horizontal and vertical resolution using NCAR's Sorted Position Radar INTerpolator (SPRINT). After the grid interpolation, the velocity data from S-Pol and KGLD were globally unfolded by means of NCAR's Custom Editing and Display of Reduced Information in Cartesian Space (CEDRIC) software (Mohr et al. 1986). The speed and direction of storm movement were manually calculated and used for the advection parameters. In the wind synthesis, the data from each radar were advected to a common time using a manually calculated storm motion vector, and the vertical velocities were obtained using a variational integration of the continuity equation (O'Brien 1970).

[8] The S-Pol radar went down for 20 minutes prior to the 0026 volume scan and therefore syntheses could not be performed during that period.

Polarimetric data were available from either CHILL or S-Pol between 2210 (3 June) and 0121 (4 June). The polarimetric data were edited, gridded and used in a fuzzy-logic hydrometeor classification scheme, (hereafter FHC), adapted from Liu and Chandrasekar (2000) and Straka et al. (2000), as in Tessendorf et al. (2005). The FHC algorithm used a temperature sounding from the 0013 (4 June) National Severe Storms Laboratory (NSSL) Electric Field Meter (EFM) balloon flight. As in Tessendorf et al. (2005), hydrometeor echo volumes were calculated for each radar scan time by multiplying the number of grid points that satisfied the FHC category of interest by the volume of a grid box (0.125 km^3).

2.2 Lightning data and processing

Two sources of lightning data used in this study were the NLDN (Cummins et al. 1998) and the New Mexico Institute of Mining and Technology (NMIMT) LMA (Rison et al. 1999). The NLDN provides the location, multiplicity, and peak current of CG flashes. The LMA provides measurements of the time and three-dimensional location of very high frequency (VHF) radiation sources emitted by lightning discharges. For a given lightning flash, the LMA may locate hundreds to thousands of such sources resulting in detailed maps of the total lightning activity.

To determine total (CG plus IC) flash rates, we used an algorithm developed at NMIMT (Thomas et al. 2003) that sorts the LMA sources into discrete flashes. To infer charge structure, we analyzed the LMA data on a flash-by-flash basis using the bi-directional discharge model (Kasemir 1960; Mazur and Ruhnke 1993), as in Wiens et al. (2005). For example, we assumed that flashes initiate in strong electric field between

regions of opposite net charge and propagate bi-directionally into the charge regions on either side. The negative breakdown component of a lightning flash is noisier at VHF, and thus is more readily detected by the LMA compared to the positive breakdown component. Assuming that negative (positive) breakdown traverses regions of net positive (negative) charge, we can infer the qualitative structure of the charge regions involved in the flash based on the temporal evolution of the flash and on the relative number of LMA sources on either side of the flash initiation location. Most IC flashes reveal distinct vertically separated "layers" of charge, with many more LMA sources in the inferred positive layer.

CHAPTER 3

OVERVIEW

3.1 Environmental conditions

The environment on 3 June 2000 was characterized by strong south-southwesterly surface winds between 8-10 m s^{-1} (gusts to near 13 m s^{-1}) ahead of a surface boundary (not shown). Weaker, northwesterly flow prevailed behind the boundary. Surface temperatures ahead of the boundary were near 32 °C, and dew points were near 12 °C. Behind the boundary the temperatures were similar, yet the dew points were as low as 0 °C. The surface boundary was likely a dry line that was moving in conjunction with a trough line. In the 0012 MGLASS sounding (Fig. 1), the CAPE was a marginal value of 700 J kg^{-1} and notable drying was evident above 500 hPa. The upper-level winds were westerly near 25 m s^{-1} (Fig. 1).

Near 1700, the surface boundary appeared as a convergence line in the radial velocity field and as a weak thin line echo in radar reflectivity (not shown). The boundary was oriented from southwest to northeast, and propagated southeastward. Just after 2200, two small cells, referred to as A and B, were observed in southwestern Nebraska along the northern end of this boundary (Fig. 2a). Near 2240, IC lightning was first detected in cell A. At 2301 (the first dual-Doppler analysis time available), mesocyclonic strength vertical vorticity (>10^{-2} s^{-1}; Moller et al. 1994) was observed in cell A (Fig. 2b). By 2330, cell B merged into the forward left flank of cell A. A visible

split in the upper-level radar reflectivity echo was observed at 2331, and the left-moving cell began to diminish soon thereafter (Fig. 2). By 0030, the maximum updraft in cell A had declined to near 5 m s^{-1} and after that the radar reflectivity echo continued to decrease over time until the storm had completely dissipated by 0121.

3.2 Kinematics and microphysics

At the time of the first dual-Doppler observations at 2301, updraft speeds were near 20 m s^{-1} and by 2350 reached a maximum of ~25 m s^{-1} (Fig. 3). During the gap in dual-Doppler scans, the updraft speeds measured by the T-28 aircraft (in pass 3) were 12.5 m s^{-1} (Holm 2005), though this may be an underestimate if the aircraft did not penetrate the strongest updraft core. When dual-Doppler observations were available again at 0026, peak updrafts were near 13 m s^{-1} and soon thereafter declined to 5 m s^{-1} and steadily decreased beyond that. However, the T-28 aircraft measured updraft speeds as high as 18 m s^{-1} between 0034-0037 (pass 7), but their scale was smaller than what could be resolved by the dual-Doppler analysis (Holm 2005).

The storm exhibited mesocyclonic strength vertical vorticity between 2301-0026 (Fig. 2b). At 2301, this vorticity was rather shallow, confined between 7-8 km, but by 2310 it lowered in altitude to as low as 4 km and persisted for at least another 20 minutes based on our dual-Doppler observations (not shown). This storm would be considered a supercell based on the criteria in Moller et al. (1994) that defines a supercell as having a deep, persistent (tens of minutes) mesocyclone. Notice that the updraft and cyclonic vorticity were collocated with the main reflectivity core for the duration of the dual-Doppler analysis (Fig. 2). Implications of this observation will be discussed further in

Chapter 5. Graupel was first detected by the FHC algorithm near 2235 in the midlevels of the storm and steadily increased in echo volume (EV) until near 2320, at which time graupel amounts leveled off until near 2350 (Figs. 3-4). After this time, the graupel EV attained its maximum value of near 1000 km^3 at 0002, most of which was centered near 7 km MSL[9] (Fig. 3).

Total hail EV was minimal and confined to 7-9 km between 0000 and 0020 (Fig. 3). According to NCDC Storm Data, there was only one large hail (> 2 cm) report associated with this storm. The report was at 0015, coincident with the FHC-inferred hail aloft. The hail EV contours in Figure 3 do not explicitly show this hail falling out, perhaps because the temporal resolution of the radar data was too coarse, or some of the hail became classified as graupel on its descent. However, it should be noted that most of the FHC-inferred low-level hail EV, shown in the contours between 2320 and 0026 that appear constrained to near 3 km, is suspect due to its horizontal stratification just below the melting level. It is possible that these hydrometeors could be melting graupel that has been misclassified as small hail (see Section 4.1). One other point to note is that the calculated total hail EV is comprised of the FHC small hail and large hail categories, and, for this storm, large hail was scarcely detected.

The trend in updraft volume greater than 10 m s^{-1} (hereafter, UV10) preceded the trends in graupel and hail EV. Shortly after the first synthesis time, UV10 rose sharply and then peaked just prior to 2320, which was just before the first peak in graupel EV (Fig. 4). By 2331, UV10 began to rise sharply again, and then peaked its maximum value at 2344. The absolute maximum in graupel EV happened within 15 minutes of this UV10 peak.

[9] All heights hereafter will be in kilometers above mean sea level (MSL).

This storm was most similar to a low-precipitation (LP) supercell because its radar echo was relatively small, it did not exhibit a low-level hook echo, nor did it have strong (> 60 dBZ) reflectivity (Fig. 2), indicating it had less overall precipitation than a "classic" supercell (Bluestein and Parks 1983). Furthermore, average radar-derived rain rates (using a R-K_{dp} relationship; Cifelli et al. 2002) on 3 June were very similar to those of the 29 June 2000 STEPS "classic" supercell *prior* to its intensification into a severe right-moving storm. However, compared to the intense phase of the 29 June storm, the 3 June storm had rain rates that were a factor of two lower (Fig. 5).

3.3 Charge structure

The relationship between lightning and graupel EV trends in this storm clearly reinforces the importance of active riming growth in the electrification process. There was no lightning until graupel was inferred to be present by radar. Furthermore, the trend in total lightning flash rate closely followed that of graupel EV (Fig. 4). This relationship was confirmed quantitatively by Wiens (2005), where a statistical correlation coefficient of 0.81 was found for the total flash rate and graupel EV trends. The maximum flash rate in this storm was near 36 min^{-1} and occurred at 0002 when the graupel EV reached its peak. This is below the 60 min^{-1} threshold that Williams et al. (1999) defined as a boundary between non-severe and severe storms.

Throughout the duration of the 3 June storm, the vast majority of lightning flashes occurred near the precipitation core of the storm and initiated downward from 9-11 km altitude with relatively dense LMA sources below the flash origin and relatively sparse LMA sources above (Fig. 6). This situation describes what could be termed an inverted

dipole, with a negative charge region near 10-12 km altitude (T < -40° C) and positive charge below. Some of these "inverted" IC flashes remained vertically confined to the upper part of the storm, with the positive charge centered near 10 km (T ~ -30° C) within strong (> 30 dBZ) lofted echo. However, most of the inverted flashes extended to much lower altitudes, with the positive charge sloping downward east of the updraft, apparently following the descent of the precipitation (see Chapter 4). Hence, the lower positive charge may have consisted of multiple layers or simply one deep charge layer. There were never any flashes that indicated an intervening negative charge region within the positive charge. As the time-height contours of total LMA sources in Figure 6b indicate, the bulk of the LMA sources were constrained between 5-10 km altitude, which is the same altitude range that we consistently identified as the positive charge region of an inverted dipole in our flash-by-flash analysis (see Chapter 4). The LMA source density contours also closely resemble the graupel EV contours in Figure 3, further emphasizing the relationship between riming ice and electrification.

Assuming non-inductive charging is responsible for electrification, the implication of this observed charge structure is that larger ice particles (e.g., graupel) received positive charge after rebounding collisions with smaller ice particles (e.g., ice crystals), the latter receiving negative charge. Furthermore, according to laboratory studies that base the sign of charge transferred on temperature and cloud liquid water content (LWC), effective LWC (a combination of the LWC and collision efficiency), or rime accretion rate (Takahashi 1978, Saunders et al. 1991, Saunders and Peck 1998), this would suggest that LWC or rime accretion rates were large enough in this storm in order for the graupel to acquire positive charge. The maximum *adiabatic* LWC (calculated

from the MGLASS sounding in Fig. 1) was 3.4 g kg^{-1} (at 8.9 km). It is well known that entrainment and mixing effects can dilute the LWC from adiabatic values, however aircraft observations in small cumulus have measured near adiabatic LWC in the cores of updrafts (Lawson and Blyth 1998). The South Dakota School of Mines and Technology (SDSMT) T-28 armored aircraft measured maximum *in situ* LWC in the range of 2-3 g m^{-3} at an altitude near 6 km (Holm 2005). Holm (2005) performed a LWC analysis that compared adiabatic LWC calculations from a composite EFM/MGLASS sounding at the height of the aircraft track to the actual SDSMT T-28 LWC measurements. Using the ratio of measured LWC to adiabatic LWC, Holm then adjusted the adiabatic LWC for the inferred regions of non-inductive charging and found that the graupel would acquire *negative* charge using the Takahashi (1978) results, while it would be in a positive charging regime using the Saunders et al. (1991) parameters. This reveals the discrepancies between the laboratory studies of non-inductive charging, as well as their extreme sensitivity to LWC, and perhaps lends support to *effective* LWC being an important non-inductive charging parameter, rather than just LWC alone. Electrification simulations by Mansell et al. (2005) and Kuhlman et al. (2006) have also shown that different charging schemes (based on the different laboratory results) can yield opposite polarity charging, and the rime accretion rate schemes (Saunders and Peck 1998) are more versatile and capable of producing inverted charge structures. Clearly, improvements in our knowledge of non-inductive charging parameters are still needed before any conclusions can be made about how the observed charge structures developed.

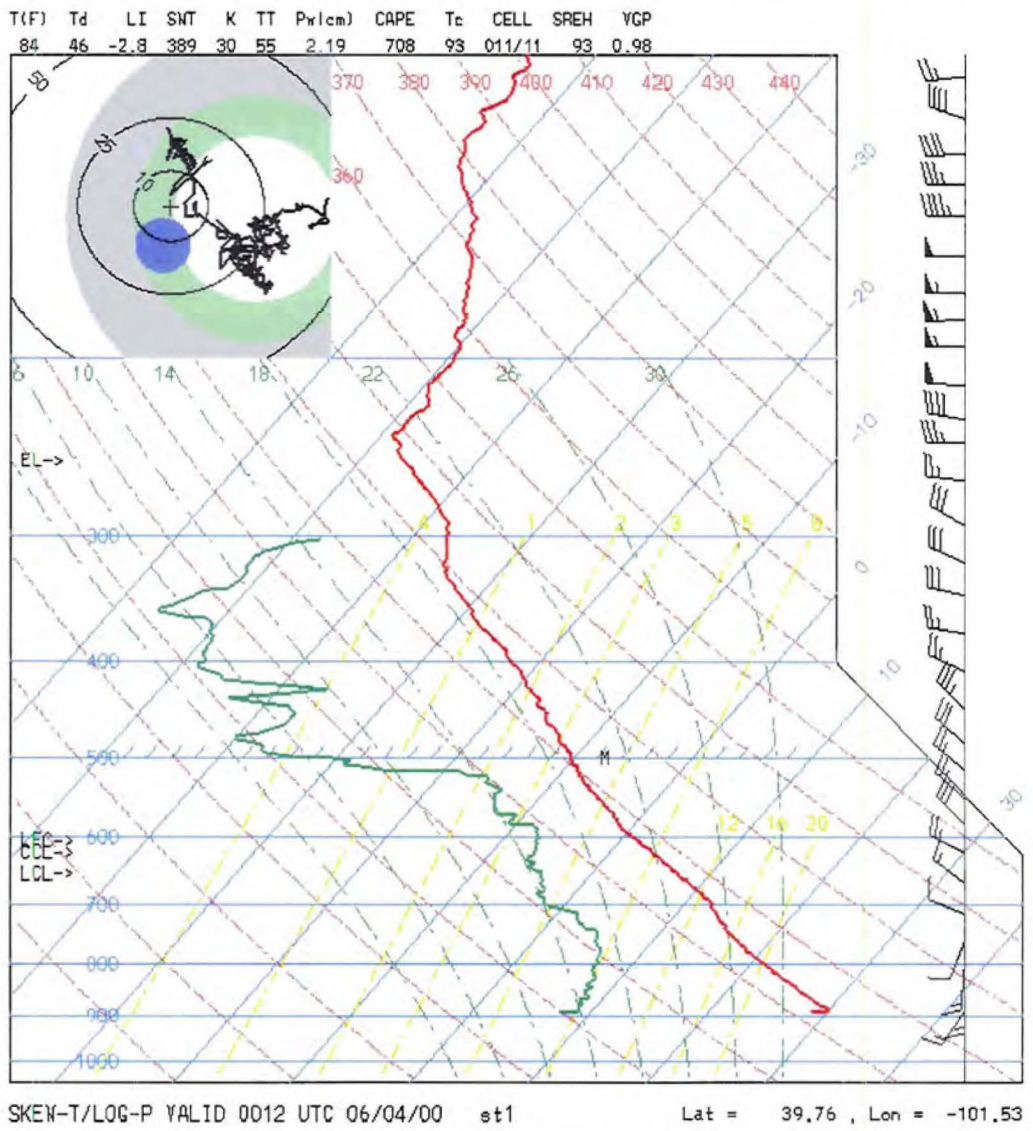

Figure 1. MGLASS sounding at 0012 UTC on 4 June 2000 near Bird City, KS.

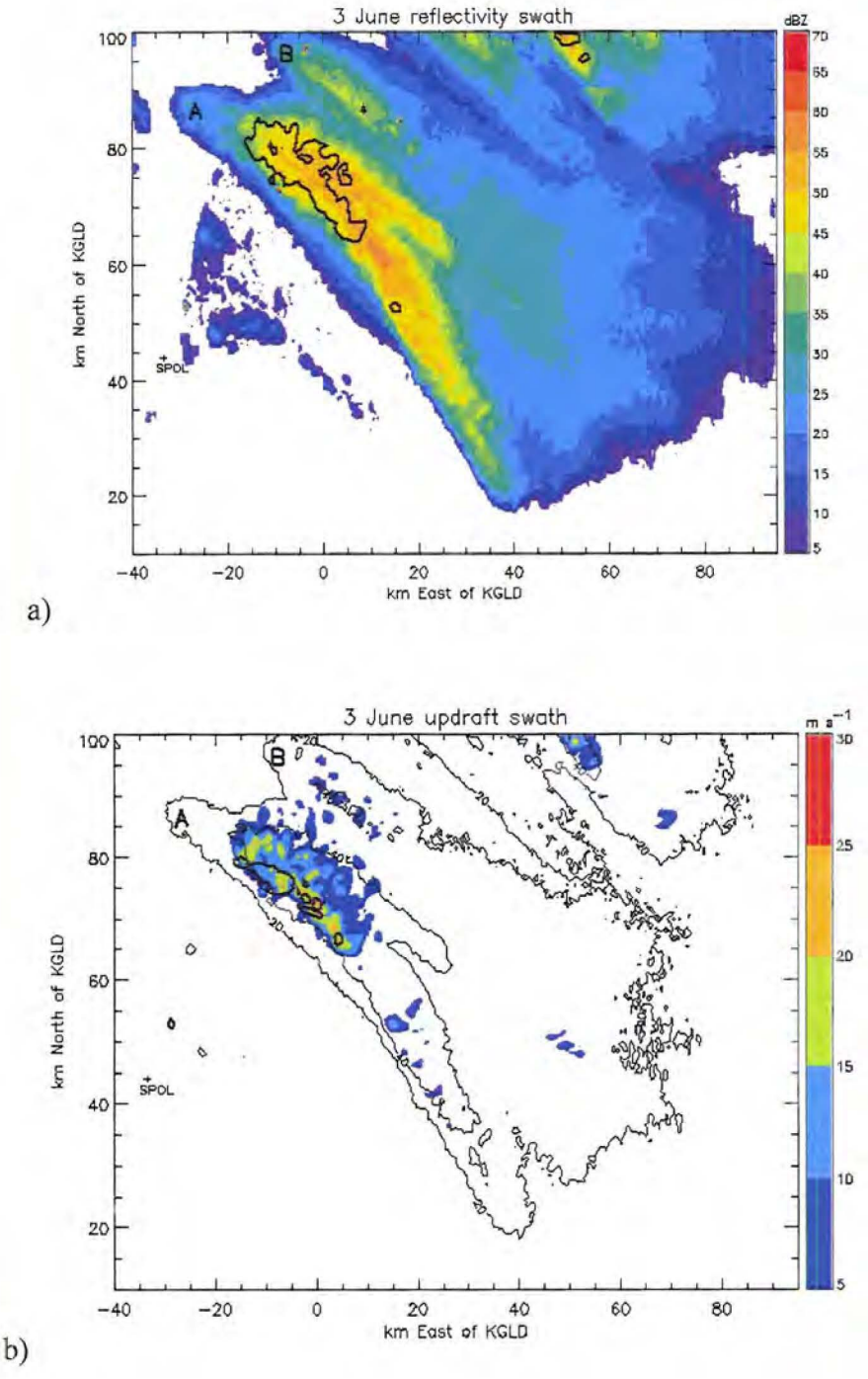

Figure 2. Swath of (a) KGLD composite reflectivity (dBZ) color contours for the period 2210-0121 UTC with a black contour overlaid indicating the regions with updrafts greater than 10 m s^{-1}, and (b) maximum updraft color contours during the dual-Doppler analysis period with a thick black contour overlaid indicating the regions with vertical vorticity greater than 10^{-2} s^{-1}. Thin black contours at 20 and 40 dBZ from (a) are overlaid (b) for reference. Radar locations are denoted with a '+' symbol.

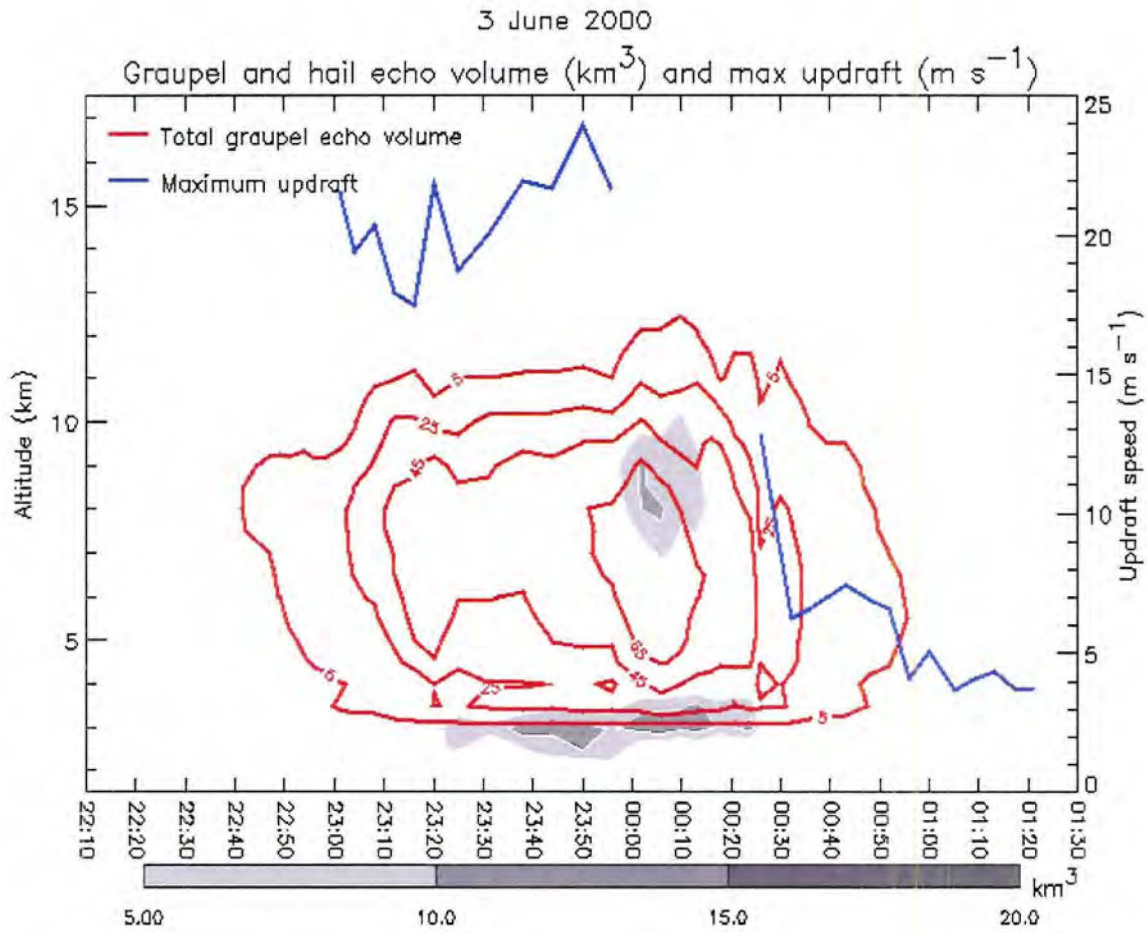

Figure 3. Time-height contours of total graupel echo volume and total hail echo volume (gray shaded contours), and maximum updraft time series (values on right axis) for 3 June 2000.

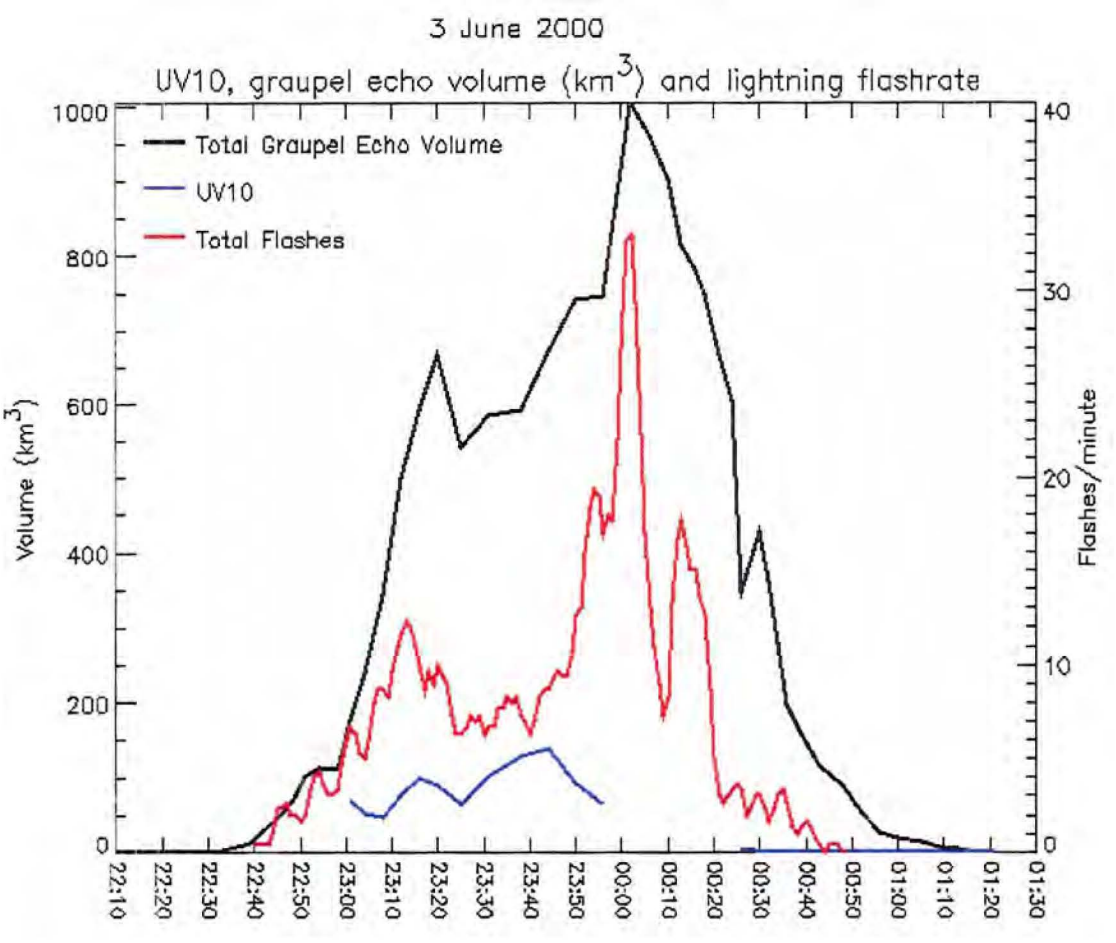

Figure 4. Time series of updraft volume greater than 10 m s^{-1} (multiplied by 10 to fit on left axis), total graupel echo volume (values on left axis), and the counted flash rate from the LMA data (values on right axis) for 3 June 2000.

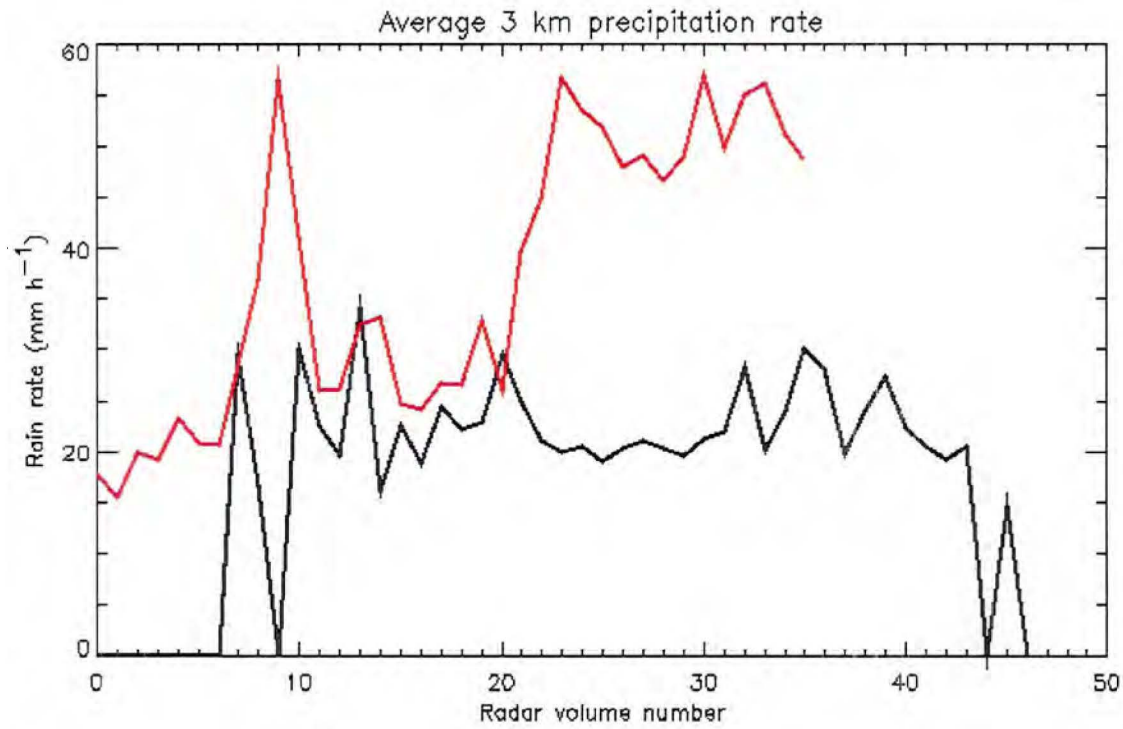

Figure 5. The average precipitation rate calculated at 3 km MSL for 3 June (black) and 29 June (red) for each sequential radar volume in their respective analysis period. The analysis period for 3 June was 2210-0121 (with 3-5 min spacing) and for 29 June was 2130-0115 (with 5-7 min spacing).

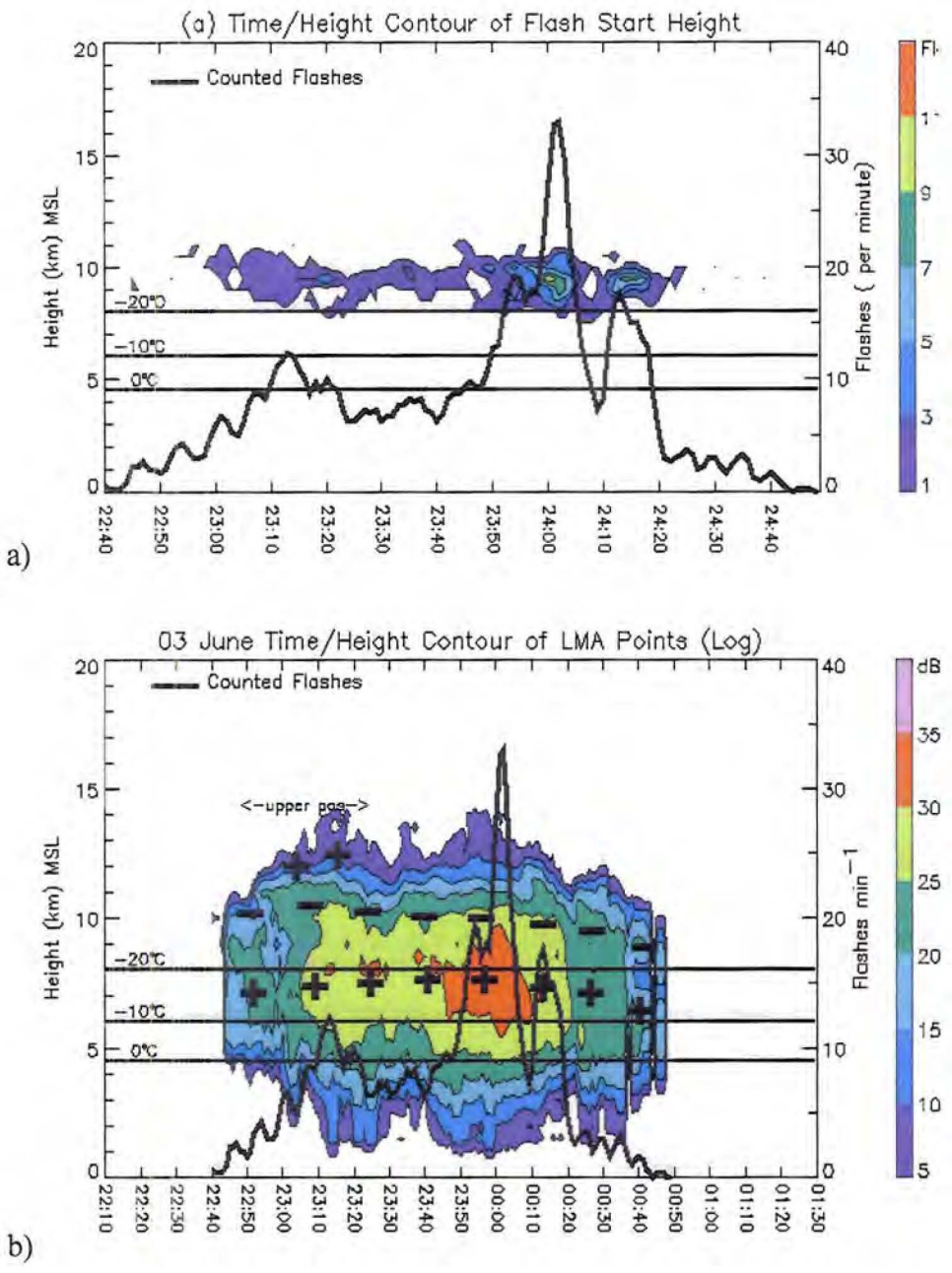

Figure 6. Time-height contours of (a) flash start height and (b) total LMA sources (color-shaded in logarithmic units) with total flash rate overlaid in black for 3 June 2000. Plus and minus symbols indicate gross LMA-inferred charge structure in (b). Isotherms at 0, −10, and −20 °C are overlaid for reference.

CHAPTER 4

DETAILED EVOLUTION

Using the UV10, graupel EV, and lightning flash rate trends in Figure 4, we have identified three main phases of the storm's evolution: a developing phase (2210-2310), a mature phase (2310-0010), and a dissipating phase (0010-0120). These three phases of the storm's life-cycle follow the three-stage classification defined by Byers and Braham (1949). We will make reference to these phases as we discuss the detailed observations.

4.1 Developing phase (2210-2310)

Near 2210, the 3 June storm (cell A in Fig. 2) was characterized by a high-based (< 10 dBZ below 5 km), shallow (< 10 dBZ above 9 km) radar echo structure with maximum reflectivity no higher than 30 dBZ (not shown). The storm was not in a location for optimal dual-Doppler analysis throughout most of the developing phase, so diagnosis of the updraft velocity during this time was not possible. The echo base (~10 dBZ) lowered to near 1.5 km by 2226, and reflectivity > 30 dBZ, inferred to be graupel by FHC, was first observed at 2233 between 7-8 km on the west side of the low-level reflectivity echo (not shown). This perhaps indicated the presence of a new and stronger updraft on the west flank of the storm, beneath this lofted echo. After this time, the storm continually exhibited a larger volume of reflectivity > 30 dBZ and FHC-inferred graupel echo (recall Fig. 4). Soon thereafter, near 2240, the first lightning flashes were observed

by the LMA. A second, weaker cell (B in Fig. 2) was first observed on radar at 2239 to the northeast of cell A.

Dual-Doppler observations of the storm were available by 2301, near the end of the developing phase. At 2301, both cells A and B had relatively weak reflectivity, with cell A still containing reflectivity just greater than 30 dBZ and some FHC-inferred graupel, while cell B did not exhibit any reflectivity greater than 30 dBZ (Fig. 7). Cell A had two updraft cores at this time: one near the west flank of the reflectivity core, as strong as 20 m s^{-1}, and a shallow and narrow 10 m s^{-1} updraft in the center of the echo (Fig. 7). Without dual-Doppler observations prior to this time we cannot diagnose the evolution of the second, smaller updraft, but perhaps it was an older updraft that was dissipating, while the stronger updraft on the west flank was a newer, developing updraft. Low-level inflow at this time was weak and south-southeasterly, with upper-level flow from the northwest (Fig. 7a-b).

The charge structure associated with the initial flashes, beginning at 2243 through 2255, could be characterized as an inverted dipole, involving a positive charge layer near 8-9 km and an upper-level negative charge layer at 10-11 km (not shown). In addition to the persistent nature of this inverted dipole, there was a roughly 30 minute time-span (2255-2325) during which several flashes initiated upward from 10-12 km into an inferred upper positive charge region that lay near the upper radar echo boundary of the storm (Figs. 7-8). Flashes involving the upper positive charge were generally within the anvil, further downwind (east) of the core. These upper flashes migrated further from the core with time. At 2301, this upper positive charge layer was above the inverted dipole and extended downwind into the anvil, centered on 11 km (Fig. 7). Also at this time, the

LMA sources were only in the vicinity of the second, smaller updraft, suggesting that the charge separation mechanisms in the stronger (perhaps newer) updraft had not yet advanced to the point of generating lightning. The charge layers sloped downward away from the updraft core, and most of the midlevel positive charge was in a region of FHC-inferred graupel, while the negative charge aloft was in FHC-inferred snow and vertically oriented ice crystals (Fig. 7). The extreme upper positive layer was also in FHC-inferred snow and ice crystals.

Though the mechanism that generated the extreme upper positive layer cannot be identified with certainty, it is possible that graupel charged positively in the updraft core, where one might expect higher LWC, and ice crystals then carried negative charge aloft to create the main inverted dipole. The upper positive was either a screening layer, or possibly the result of non-inductive charging on either the periphery of the current updraft or in a weaker, older convective updraft causing the riming ice to receive negative charge while the smaller ice crystals carried positive charge further aloft to create the extreme upper positive charge. Since this feature moved further downwind over time, it is likely that the precipitation being exhausted into the anvil and falling out downwind was carrying the charge, rather than it being a screening layer atop the main inverted dipole.

4.2 Mature phase (2310-0010)

During the mature phase of cell A, maximum updraft velocities were near 20 m s^{-1} and UV10 reached 100 km^3 (recall Figs. 3-4). By 2325, cell B had merged into the northern flank of cell A and three 10 m s^{-1} updraft cores were resolved at 7 km (as seen in

Fig. 8a-b). The low-level inflow at this time was still south-southeasterly with northwesterly upper-level flow. The two larger updraft areas (to the west and south) became one broad updraft region by 2331 (not shown), while the northern updraft core remained separate and even developed its own upper-level reflectivity core by 2331, creating a split in the storm reflectivity echo (also seen at 2344 in Fig. 9b). Due to the enhanced cyclonic vorticity collocated with the updraft during the mature phase of this storm, there is some cyclonic curvature in the flow around the south side of the southern, larger updraft (Fig. 8a-b). The location of this curvature in the flow relative to the updraft, however, carries growing particles in the updraft around to the downwind and northern side of the updraft where it will fallout away from the storm inflow, thus preventing them from reentering the updraft for further growth.

A modest overhang can be seen in the reflectivity and FHC fields at 2325 (Fig. 8c-d), with graupel inferred in the upper levels of the updraft. The small hail classified by FHC in Figure 8c near 3 km is likely a misclassification of melting graupel. In this figure, the hydrometeors directly above the region classified as small hail (SH) are high-density graupel (HG) and low-density graupel (LG). As the LG particles fall through the melting level at 4.5 km, the meltwater on their surfaces returns a higher radar returned power (i.e. radar reflectivity), and due to the increasing radar reflectivity the LG particle is classified as HG, and then as SH, based on the radar variable thresholds in the FHC algorithm (Tessendorf et al. 2005).

The charge structure in the mature phase of this storm was still characterized as an inverted dipole nearest the precipitation core (Fig. 8d). Most of the inferred positive charge was again in the region of FHC-inferred graupel, while the negative charge was in

the upper levels where snow and ice crystals were identified by FHC. The flash in the eastern anvil in Figure 8 was the last flash that clearly involved the upper positive charge, and it is much farther downwind from the precipitation core at this time. Both the negative and positive charge layers were in regions of FHC-inferred snow and ice crystals in the anvil.

By 2344, the updraft was at its all-time maximum intensity (at least based on the dual-Doppler observations available) in the main updraft along the southwest flank of the storm (Fig. 9). The northern flank updraft now had a distinct reflectivity core that was diverging from the southern updraft over time and responsible for the northern branch of the V-shaped low-level reflectivity. Persistent south-southeasterly inflow and upper-level northwesterly flow was still evident, as well as some cyclonic curvature around the south side of the main updraft (Fig. 9a-b). The persistent inverted dipole (now without the extreme upper positive layer) was still the dominant charge structure and, within the updraft region, FHC-inferred graupel (ice crystals) was (were) observed where the LMA indicated positive (negative) charge.

4.3 Dissipating phase (0010-0120)

Though the dual-Doppler observations were not available for the 20-minute period prior to 0026, it is apparent that the storm entered its dissipating phase during this time. The graupel EV and total lightning flash rates rapidly diminished near 0010, and by 0026 dramatically weaker maximum updraft speeds and UV10 were observed (recall Figs. 3-4). At 0026 two distinct cores were observed in the low-level reflectivity field, each corresponding to the northern and southern updraft cores previously discussed at

2344. The upper-level reflectivity in the northern core had greatly diminished by 0026, while the southern upper-level reflectivity core was still greater than 30 dBZ. The updraft in the southern core was still 10 m s^{-1} at 0026, but quickly weakened to near 5 m s^{-1} in the subsequent radar volume. The low-level inflow was now more southerly, and the upper-level flow was west-southwesterly (Fig. 10a-b).

The charge structure during this phase was still representative of an inverted dipole, with a very deep main positive charge region below an upper-level negative charge layer (Fig. 10d). The charge layers were observed higher within the updraft core, and they sloped downward away from the updraft into the precipitation core. As in the previous figures, FHC-inferred graupel was observed in regions with positive charge and ice crystals were inferred aloft where the negative charge was detected (Fig. 10). The inverted dipole was still persistent up until the last observed flash at 0046 (not shown).

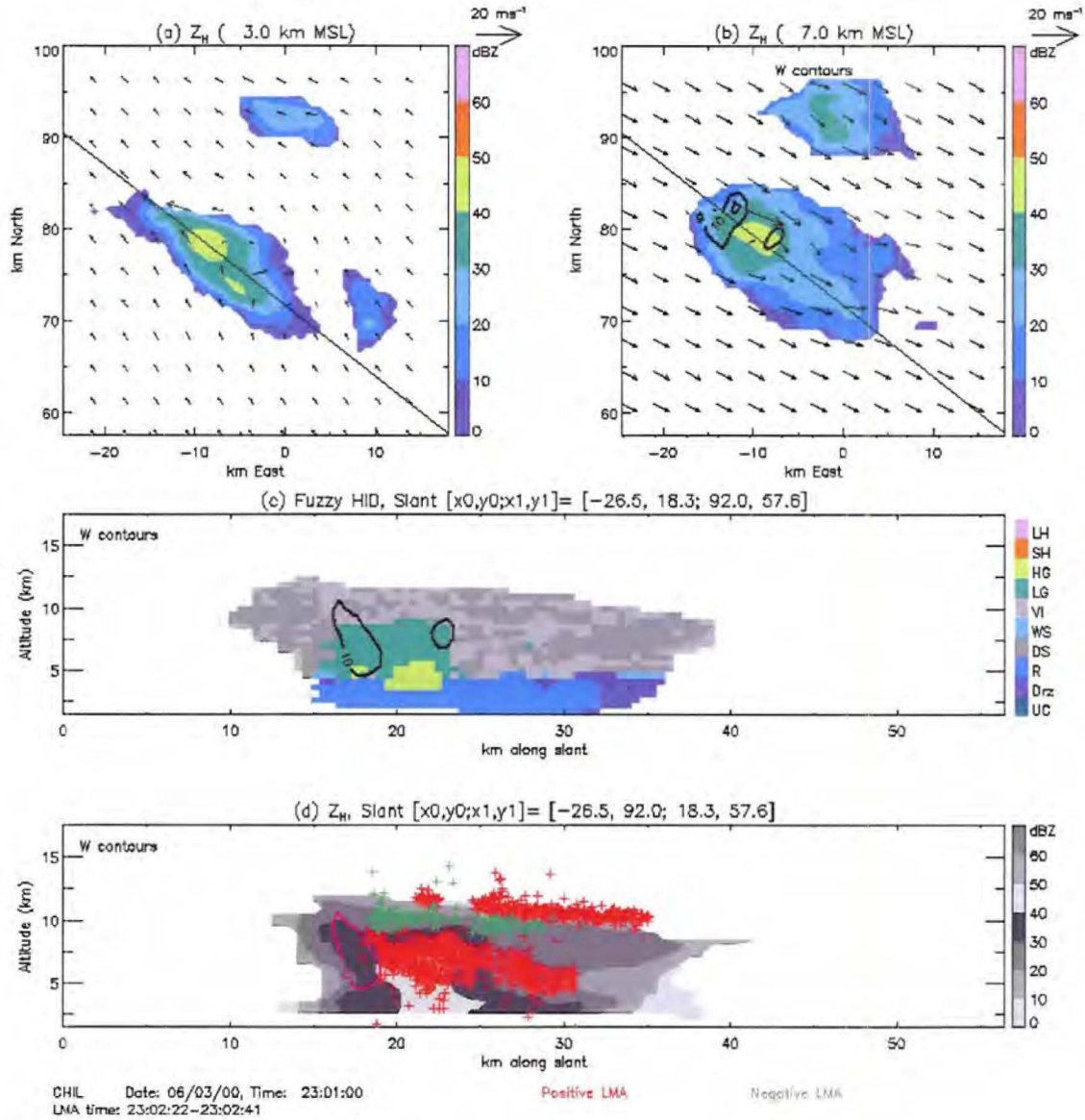

Figure 7. KGLD horizontal radar reflectivity (Z_h) at 2301 at (a) z = 3 km and (b) z = 7 km; fuzzy logic hydrometeor classification (FHC; using polarimetric data from CHILL along slanted black line in (a) and (b) is in (c), and grayscale contours of KGLD Z_h along slanted black line in (a) and (b) is in (d). Updraft velocity contours beginning at 10 m s^{-1} (with a 10 m s^{-1} contour interval) are overlaid in black in (b) and (c) and in pink in (d). LMA data of four representative flashes between 23:02:22-23:02:41 has been overlaid as small plus symbols onto (d) by inferred charge (red = positive, green = negative). Storm relative wind vectors have been overlaid onto (a) and (b). FHC categories are: large hail (LH), small hail (SH), high-density graupel (HG), low-density graupel (LG), vertically oriented ice crystals (VI), wet snow (WS), dry snow (DS), rain (R), drizzle (Drz), and unclassified (UC). Note: the LMA sources atop the storm appear to not be within reflectivity echo, but the 0 and 10 dBZ contours around the periphery of the storm are partially missing, either due to scanning/gridding geometry or the editing algorithms deleting echo in low signal-to-noise regions.

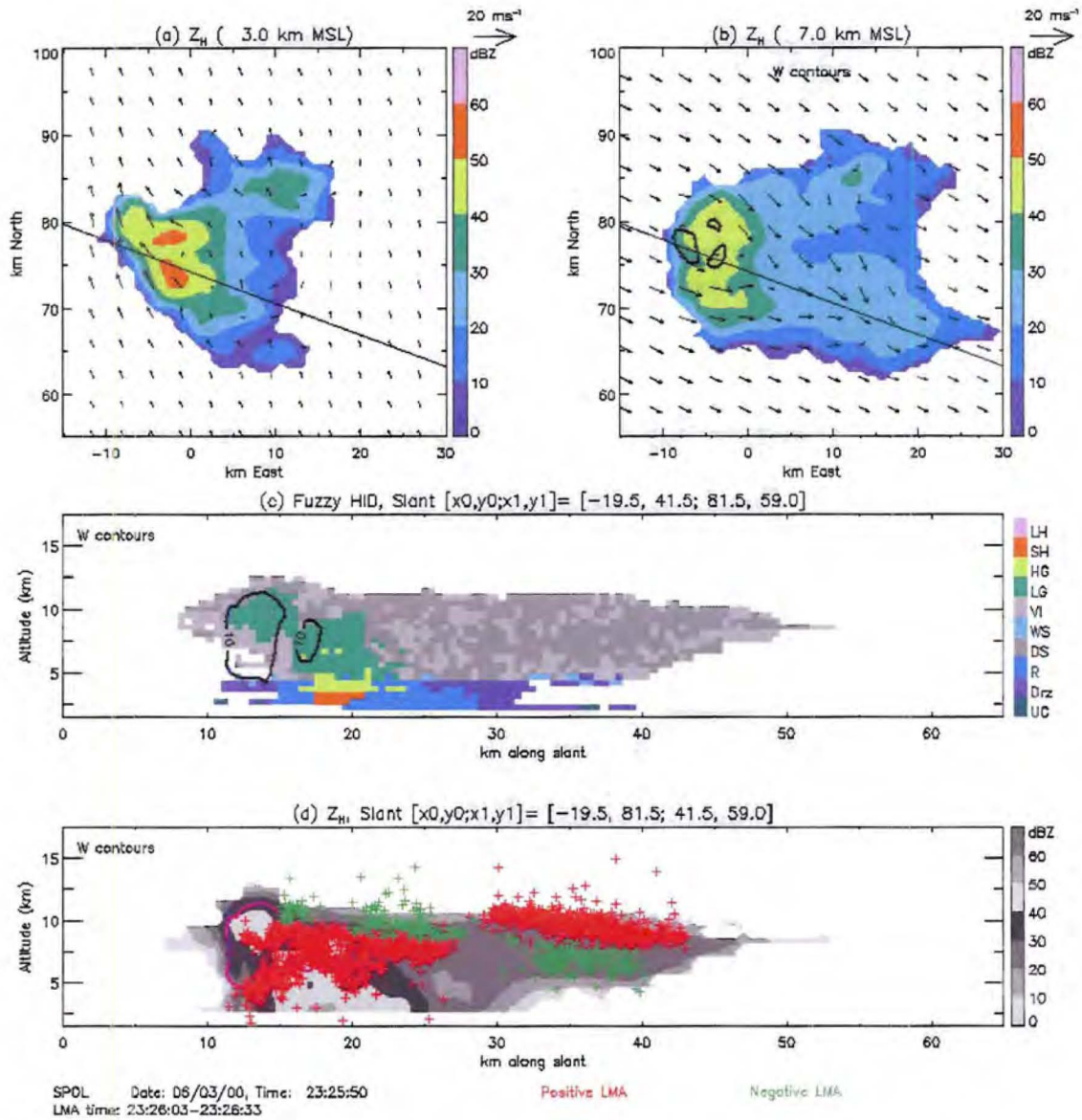

Figure 8. Same as Fig. 7, except for at 2325, the vertical cross-sections in (c) and (d) are at a slanted line shown in (a) and (b), and the FHC used polarimetric data from SPOL. LMA data of four representative flashes from 23:26:03-23:26:33 is overlaid in (d).

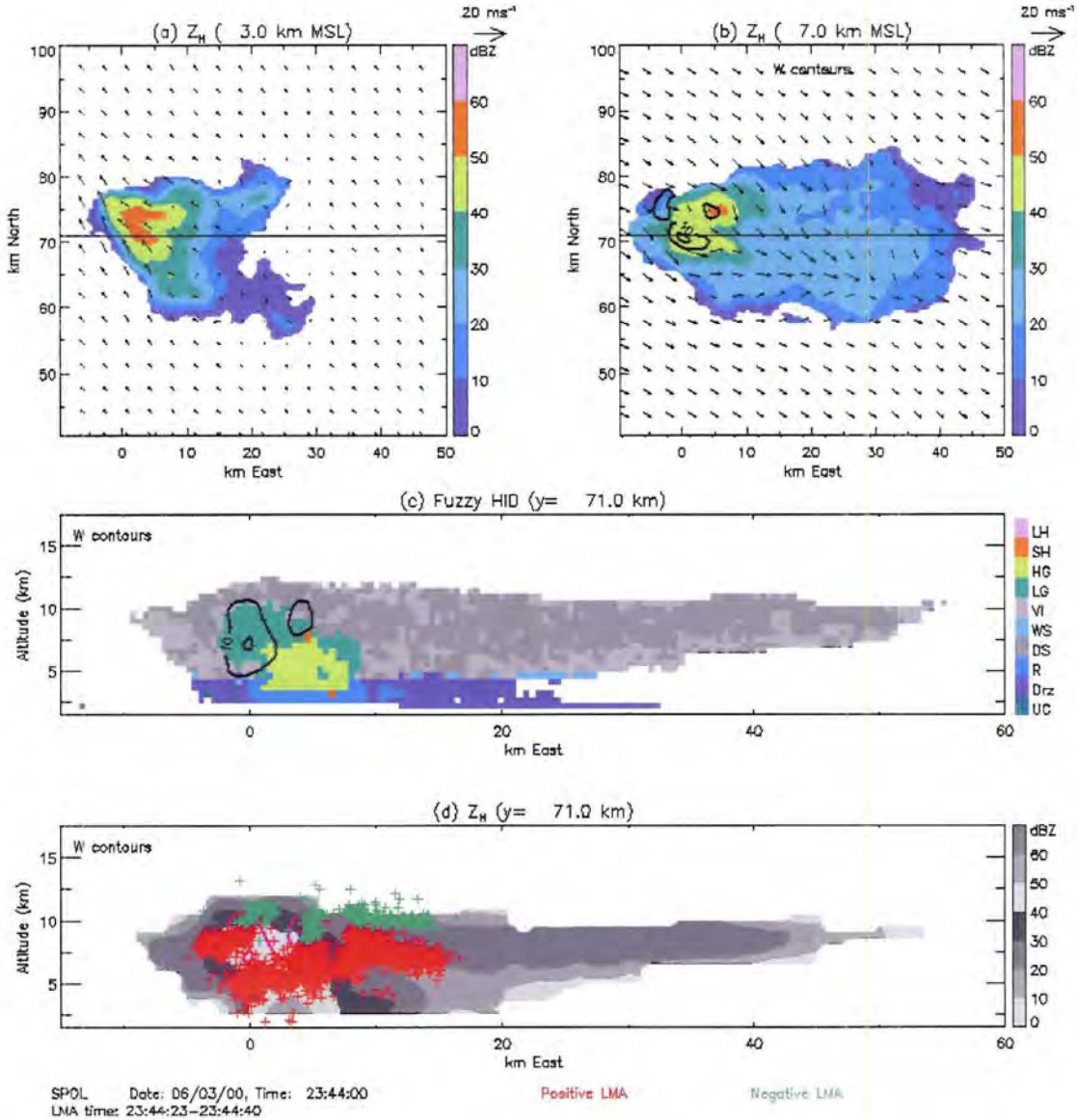

Figure 9. Same as Fig. 7, except for at 2344, the vertical cross-sections in (c) and (d) are at y = 71 km, and the FHC used polarimetric data from SPOL. LMA data of three representative flashes from 23:44:23-23:44:40 is overlaid in (d).

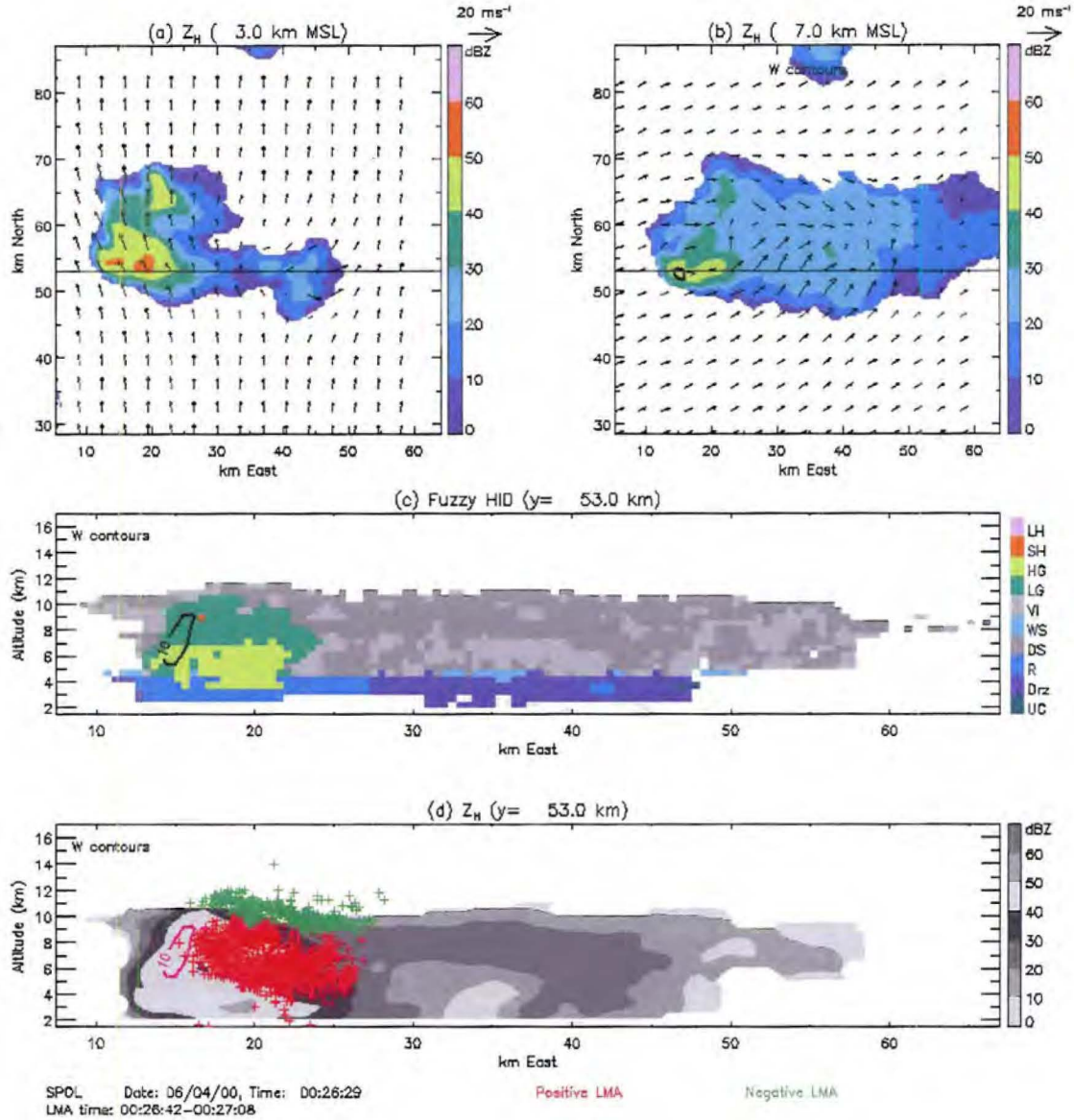

Figure 10. Same as Fig. 7, except for at 0026, the vertical cross-sections in (c) and (d) are at y = 53 km, and the FHC used polarimetric data from SPOL. LMA data of two representative flashes from 00:26:42-00:27:08 is overlaid in (d).

CHAPTER 5

DISCUSSION

The 3 June storm had moderate updraft speeds (20-25 m s^{-1}), as well as moderate FHC-inferred graupel and small hail, with limited large hail. Compared to the 29 June STEPS supercell (Tessendorf et al. 2005), this storm had half the maximum updraft speeds and nearly an order of magnitude less graupel and hail EV. A few possible reasons for the lack of (large) hail in this storm were the weaker, narrower updrafts and the collocation of the updraft and cyclonic vorticity (see Fig. 2b). Tessendorf et al. (2005) showed that cyclonically curved flow on the *right flank* of the updraft was an important ingredient, in addition to sufficient updraft size and intensity, in the production of large (> 2 cm) hail, by allowing embryonic particles, which had likely fallen from the upper-level stagnation zone upwind of the updraft, to reenter the updraft for continued growth. With the cyclonic vorticity collocated with the updraft in 3 June, the particles grown from scratch were likely exhausted into the anvil or along the north side of the updraft, certainly not in a position to reenter the southeasterly inflow for continued growth (see Fig. 8). Nonetheless, this storm was very similar to the early kinematic, microphysical, and electrical evolution of the 29 June storm, at least prior to its right turn and dramatic intensification (Tessendorf et al. 2005, Wiens et al. 2005).

Maximum total flash rates in this storm were near 30 flashes min^{-1}, which is below the 60 flashes min^{-1} threshold found by Williams et al. (1999) to distinguish non-

severe from severe storms. Thus, even though this storm did have an isolated severe hail report, which technically classifies it as a severe storm, its flash rates were low compared to typical severe storms. Furthermore, no CG flashes of either polarity were detected by NLDN, but based on the LMA data, the storm exhibited a persistent inverted dipole charge structure from its very first IC flash through the last. Prior to its right turn and onset of its severe phase, the total flash rates in 29 June were on the same order of magnitude as those in 3 June, but afterwards, flash rates in 29 June gained an order of magnitude and frequent positive CG flash activity began (Wiens et al. 2005). The 29 June storm also exhibited an inverted charge structure, but a lower negative charge region was also inferred below the inverted dipole by LMA observations (Wiens et al. 2005). The LMA data never indicated the presence of a lower negative charge layer below the inverted dipole in 3 June.

The right flank development of the 29 June storm, that manifested itself as a right turn, was a key factor in distinguishing the 29 June storm from that of 3 June. How might have the processes responsible for the right turn led to the dramatic difference in these storms' microphysical and electrical behaviors? It was clear in 29 June that, after the right turn, the cyclonic vorticity became more offset from the updraft, and as mentioned above, this likely enabled the storm to produce large hail (Tessendorf et al. 2005). Perhaps the low-precipitation character of the 3 June storm reduced the magnitude of the rear flank downdraft (via reduced evaporative cooling to enhance the negative buoyancy), and inhibited low-level convergence along the gust front, which has been shown to facilitate right flank updraft development (Klemp et al. 1981). Furthermore, it has been suggested that a lower positive charge layer provides the

downward bias for negative CG flashes (Williams et al. 1989, Mansell et al. 2002). Additionally, Kuhlman et al. (2006) simulated the electrification in the 29 June supercell and suggested that the observed and simulated lower negative charge layer was crucial to the production of positive CGs. Perhaps the lack of a lower *negative* charge layer in 3 June inhibited the production of positive CG flashes.

In the simulation by Kuhlman et al. (2006), the lower negative charge formed by a combination of negative non-inductive charging of graupel outside the updraft core, precipitation fallout and recycling, and inductive charging. Based on additional storm electrification simulations, Mansell et al. (2005) suggested that non-inductive charging could account for the lower charge layer without inductive charging processes, if the ice crystal concentrations at lower altitudes (i.e. warmer temperatures) were high enough (> 50 L^{-1} in their simulations), but for all other cases, inductive charging was deemed important. The reason for the apparent lack of a lower negative charge layer in 3 June is difficult to pinpoint, but may have been attributed to the following factors: 1) perhaps there was a lower negative charge layer, but it was too weak to initiate a discharge without which the LMA cannot observe it (this is supported by the 0013 EFM sounding that indicated a weak lower negative charge layer may have been present; Rust et al. 2005), 2) inductive charging processes were inhibited, perhaps due to less liquid precipitation in this LP storm, 3) the lack of precipitation recycling reduced the quantity of riming ice growing at lower altitudes, which suppressed (non-inductive or inductive) precipitation-based charge separation processes needed to generate the low-level charge layer.

We feel it is important to make the distinction between storms studied in the literature with low-CG, high-IC flash rates, or high IC:CG ratios (MacGorman et al. 1989, MacGorman and Burgess 1994, Lang et al. 2000, Lang and Rutledge 2002), and the present storm that exhibited *no* CG flashes, since the reasons for each type of behavior could be due to different mechanisms. For example, the proposed 'elevated charge' hypothesis (MacGorman et al. 1989), which has been previously used to explain low-CG storms, still seems to be a plausible reason for keeping CG flash rates low, while maintaining or enhancing IC flash rates, in kinematically intense storms. In fact, even in this storm nearest the strongest updraft, the LMA sources and inferred charge layers were observed at higher altitudes than the rest of the storm (see Figs. 7-10). However, we speculate that the absence of a lower charge layer, both opposite in polarity to the charge region sending charge to ground and of appropriate strength to provide the downward bias for the discharge, is perhaps a key reason for the complete lack of CG flashes in otherwise electrically-active storms. This suggestion is based upon the data that indicates no CG flashes were detected, nor a lower negative charge layer inferred, in the 3 June storm.

CHAPTER 6

CONCLUSIONS

The objective of this study was to examine relationships between the kinematic, microphysical, and electrical aspects of the 3 June non-CG-producing supercell. The radar coverage on this day was suitable for studying the storm structure evolution; however, the dual-Doppler coverage was not optimal, and therefore we were unable to estimate vertical velocities over the entire storm's evolution. Nonetheless, the isolated nature to this storm, in addition to its modest flash rates, gave us a unique opportunity to study the evolution of charge structure for an inverted storm using the LMA data.

No CG flashes of either polarity were detected in this storm, but based on the LMA data it exhibited a persistent inverted dipole charge structure. Moreover, the LMA data never indicated the presence of a lower negative charge layer below the inverted dipole. Much like the lower positive charge layer has been deemed important in producing negative CG flashes, we suggest that the lack of the lower *negative* charge layer, which completes the *inverted* tripole and may provide the downward bias for positive CG flashes, was a key factor in preventing this storm from producing positive CG flashes. Certainly, more storms that produce IC, but not CG, lightning need to be examined to evaluate this claim.

REFERENCES

Bluestein, H.B, and C.R. Parks, 1983: A synoptic and photographic climatology of low-precipitation severe thunderstorms in the Southern Plains. *Mon. Wea. Rev.*, **111**, 2034-2046.

Brook, M., M. Nakano, P. Krehbiel, and T. Takeuti, 1982: The electrical structure of the Hokuriku winter thunderstorms. *J. Geophys. Res.*, **87**, 1207-1215.

Byers, H.R., and R.R. Braham, 1949: *The Thunderstorm.* U.S. Gov't Printing Office, Washington D.C., 287 pp. [NTIS PB-234-515.]

Carey, L.D. and S.A. Rutledge, 1998: Electrical and multiparameter radar observations of a severe hailstorm. *J. Geophys. Res.*, **103**, 13,979-14,000.

Carey, L,D., and S.A. Rutledge, 2003: Characteristics of cloud-to-ground lightning in severe and nonsevere storms over the central United States from 1989-1998. *J. Geophys. Res.*, **108**, doi: 10.1029/2002JD002951.

Cifelli, R., W. A. Petersen, L. D. Carey, S. A. Rutledge, and M.A.F. da Silva Dias, 2002: Radar observations of the kinematic, microphysical, and precipitation characteristics of two MCSs in TRMM-LBA. *J. Geophys. Res.*, **107**, doi: 10.1029/2000JD0000264.

Cummins, K. L., M. J. Murphy, E. A. Bardo, W. L. Hiscox, R. B. Pyle, and A. E. Pifer, 1998: A combined TOA/MDF technology upgrade of the U.S. National Lightning Detection Network. *J. Geophys. Res.*, **103** (D8), 9035–9044.

Holm, M.L., 2005: *A case study of the 3 June 2000 STEPS storm: The electrification of a low precipitation supercell.* M.S. Thesis, South Dakota School of Mines and Tech., Rapid City, SD, 87 pp.

Kasemir, H. W., 1960: A contribution to the electrostatic theory of lightning discharge. *J. Geophys. Res.*, **65**, 1873-1878.

Klemp, J.B., R.B. Wilhelmson, and P.S. Ray, 1981: Observed and numerically simulated structure of a mature supercell thunderstorm. *J. Atmos. Sci.*, **38**, 1558-1580.

Kuhlman, K.M., C.L. Ziegler, E.R. Mansell, D.R. MacGorman, and J.M. Straka, 2006: Numerical simulations of the 29 June 2000 STEPS supercell: Microphysics, electrification, and lightning. *Mon. Wea. Rev.,* in review.

Lang, T.J., and S.A. Rutledge, 2002: Relationships between convective storm kinematics, precipitation, and lightning. *Mon. Wea. Rev.*, **130**, 2492-2506.

Lang, T.J., S.A. Rutledge, J.E. Dye, M. Venticinque, P. Laroche, and E. Defer, 2000: Anomalously low negative cloud-to-ground lightning flash rates in intense convective storms observed during STERAO-A. *Mon. Wea. Rev.*, **128**, 160-173.

Lang, T.J., and Coauthors, 2004: The Severe Thunderstorm Electrification and Precipitation Study. *Bull. Amer. Meteor. Soc.*, **85**, 1107-1125.

Lawson, R.P., and A.M. Blyth, 1998: A comparison of optical measurements of liquid water content and drop size distribution in adiabatic regions of Florida cumuli. *Atmos. Res.*, **48**, 671-690.

Liu, H., and V. Chandrasekar, 2000: Classification of hydrometeors based on polarimetric radar measurements: Development of fuzzy logic and neuro-fuzzy systems and in situ verification. *J. Atmos. Oceanic Technol.*, **17**, 140-164.

MacGorman, D.R., and D.W. Burgess, 1994: Positive cloud-to-ground lightning in tornadic storms and hailstorms. *Mon. Wea. Rev.*, **122**, 1671-1697.

MacGorman, D.R., D.W. Burgess, V. Mazur, W.D. Rust, W.L. Taylor, and B.C. Johnson, 1989: Lightning rates relative to tornadic storm evolution on 22 May 1981. *J. Atmos. Sci.*, **46**, 221-250.

MacGorman, D.R., W.D. Rust, P. Krehbiel, E. Bruning, and K. Wiens, 2005: The electrical structure of two supercell storms during STEPS. *Mon. Wea. Rev.*, **133**, 2583-2607.

Mansell, E.R., D.R. MacGorman, C. Ziegler, and J.M. Straka, 2002: Simulated three-dimensional branched lightning in a numerical thunderstorm model. *J. Geophys. Res.*, **107**, doi: 10.1029/2000JD00244.

Mansell, E.R., D.R. MacGorman, C.L. Ziegler, and J.M. Straka, 2005: Charge structure and lightning sensitivity in a simulated multicell thunderstorm. *J. Geophys. Res.*, **110**, doi: 10.1029/2004/JD005287.

Mazur, V. and L. H. Ruhnke, 1993: Common physical processes in natural and artificially triggered lightning. *J. Geophys. Res.*, **98**, 12,913-12,930.

Mohr, C.G., L.J. Miller, R.L. Vaughn, and H.W. Frank, 1986: On the merger of mesoscale data sets into a common Cartesian format for efficient and systematic analysis. *J. Atmos. Oceanic. Technol.*, **3**, 143-161.

Moller, A.R., C.A. Doswell III, M.P. Foster, and G.R. Woodall, 1994: The operational recognition of supercell thunderstorm environments and storm structures. *Wea. Forecasting*, **9**, 327-347.

O'Brien, J.J., 1970: Alternative solutions to the classical vertical velocity problem. *J. Appl. Meteor.*, **9**, 197-203.

Orville, R.E., and G.R. Huffines, 2001: Cloud-to-ground lightning in the United States: NLDN results in the first decade, 1989-98. *Mon. Wea. Rev.*, **129**, 1179-1193.

Rison, W., R. J. Thomas, P. R. Krehbiel, T. Hamlin, and J. Harlin, 1999: A GPS-based three-dimensional lightning mapping system: Initial observations in Central New Mexico. *Geophys. Res. Lett.*, **26**, 3573-3576.

Rust, W.D., D.R. MacGorman, E.C. Bruning, S.A. Weiss, P.R. Krehbiel, R.J. Thomas, W. Rison, T. Hamlin, and J. Harlin, 2005: Inverted-polarity electrical structure in thunderstorms in the Severe Thunderstorm Electrification and Precipitation Study (STEPS). *Atmos. Res.*, **76**, 247-271.

Saunders, C.P.R., and S.L. Peck, 1998: Laboratory studies of the influence of the rime accretion rate on charge transfer during graupel/crystal collisions. *J. Geophys. Res.*, **103**, 13,949-13,956.

Saunders, C.P.R., W.D. Keith, and R.P. Mitzeva, 1991: The effect of liquid water on thunderstorm charging. *J. Geophys. Res.*, **96**, 11,007-11,017.

Seimon, A., 1993: Anomalous cloud-to-ground lightning in an F5-tornado-producing supercell thunderstorm on 28 August 1990. *Bull. Amer. Meteor. Soc.*, **74**, 189-203.

Simpson, G.C., and F.J. Scrase, 1937: The distribution of electricity in thunderclouds. *Proc. Roy. Soc. London, Ser. A*, **161**, 309-352.

Straka, J.M., D.S. Zrnic, and A.V. Ryzhkov, 2000: Bulk hydrometeor classification and quantification using polarimetric radar data: Synthesis of relations. *J. Appl. Meteor.*, **39**, 1341-1372.

Takahashi, T., 1978: Riming electrification as a charge generation mechanism in thunderstorms. *J. Atmos. Sci.*, **35**, 1536-1548.

Tessendorf, S.A., L.J. Miller, K.C. Wiens, and S.A. Rutledge, 2005: The 29 June 2000 supercell observed during STEPS. Part I: Kinematics and microphysics. *J. Atmos. Sci.*, **62**, 4127-4150.

Thomas, R., P. Krehbiel, W. Rison, J. Harlin, T. Hamlin, and N. Campbell, 2003: The LMA flash algorithm. Abstract C4-23, *Proc. 12th Intl. Conf. On Atmos. Elect.*, 655-656, Versailles, France.

Wiens, K.C., 2005: *Kinematic, microphysical, and electrical structure and evolution of thunderstorms during the Severe Thunderstorm Electrification and Precipitation Study (STEPS).* Ph.D. thesis, Colorado State University, Fort Collins, CO, 295 pp.

Wiens, K.C., S.A. Rutledge, and S.A Tessendorf, 2005: The 29 June 2000 supercell observed during STEPS. Part II: Lightning and charge structure. *J. Atmos. Sci.*, **62**, 4151-4177.

Williams E.R., 2001: The electrification of severe storms. *Severe Convective Storms*, C.A. Doswell, III, Ed., *Meteor. Monogr.*, No. 50, Amer. Meteor. Soc., 527-561.

Williams, E.R., M.E. Weber, and R.E. Orville, 1989: The relationship between lightning type and convective state of thunderclouds. *J. Geophys. Res.*, **94**, 13,213-13,220.

Williams, E.R., and Coauthors, 1999: The behavior of total lightning activity in severe Florida thunderstorms. *Atmos. Res.*, **51**, 245-264.

PART III: CLOUD-TO-GROUND ACTIVITY IN TWO MULTICELLULAR STORMS OBSERVED DURING STEPS

CHAPTER 1

INTRODUCTION

Positive cloud-to-ground (CG) lightning is fairly uncommon compared to negative polarity CG lightning based on lightning climatologies for the U.S. (Orville and Huffines 2001). However, several studies have documented storms that produced predominantly (> 50%) positive CG (PPCG) lightning, which also tended to have severe weather characteristics (e.g. Rust et al. 1981, Branick and Doswell 1992, Seimon 1993, MacGorman and Burgess 1994, Carey et al. 2003). While the link between storm severity and PPCG lightning has yet to be fully revealed given that all severe storms do not exhibit PPCG characteristics, there is a general tendency for PPCG storms to be severe. Furthermore, anomalous positive CG lightning has been documented to occur most frequently in the U.S. High Plains, which might suggest that a regional characteristic of the High Plains may affect CG polarity (Orville and Huffines 2001, Carey and Rutledge 2003).

An obvious research question that arises from these observations is what storm processes are responsible for PPCG lightning behavior and secondarily, how might those processes relate to storm severity, if at all? In order to assess this question, we must first look at the charge structure from which positive CG lightning originates. Williams (2001) summarized several hypothesized charge structures that might lead to positive CG lightning, such as the tilted dipole, precipitation unshielding, and the inverted dipole.

Several studies have evaluated those hypotheses (MacGorman and Burgess 1994, Carey and Rutledge 1998, Lang and Rutledge 2002), but none have had the benefit of three-dimensional lightning mapping data to infer the actual charge structure throughout the entire storm. The Severe Thunderstorm Electrification and Precipitation Study (STEPS; Lang et al. 2004) provided a unique dataset to assess this question for thunderstorms on the High Plains. To date, the 29 June 2000 supercell from STEPS has been studied extensively (MacGorman et al. 2005, Tessendorf et al. 2005, Wiens et al. 2005, Kuhlman et al. 2006). The goal of the present study is to determine the charge structure of two *multicellular* storms from STEPS that exhibited opposite dominant CG polarity (positive versus negative), especially during the production of CG flashes, and to speculate on the kinematic and microphysical differences between the two cases that might lead to the opposite CG polarity behavior.

CHAPTER 2

DATA AND METHODS

Instrumentation and observing systems operated during STEPS are outlined in detail in Lang et al. (2004). This study uses radar data from the triple-Doppler S-band radar network and lightning data from the National Lightning Detection Network (NLDN; Cummins et al. 1998), and the three-dimensional Lightning Mapping Array (LMA; Rison et al. 1999) operated by the New Mexico Institute of Mining and Technology.

2.1 Radar data processing

The CSU-CHILL polarimetric Doppler radar, the National Center for Atmospheric Research (NCAR) S-Pol polarimetric Doppler radar, and the Goodland, Kansas National Weather Service (NWS) WSR-88D radar (KGLD) comprised the triple-Doppler radar network in which each radar was located approximately 60 km apart forming a rough equilateral triangle configuration (Tessendorf et al. 2005; their Figure 1).

Wind field syntheses were completed for 27 volume scans during the period 2318 UTC (19 June)-0213 UTC[10] (20 June) and 11 volume scans during the period 2356 (22 June)-0108 (23 June). The radar data were interpolated onto a Cartesian grid using NCAR's Sorted Position Radar INTerpolator (SPRINT) with a grid resolution of 0.5 km

[10] All times hereafter are listed in UTC.

in both the horizontal and vertical directions. After the grid interpolation, the velocity data were globally unfolded by means of NCAR's Custom Editing and Display of Reduced Information in Cartesian Space (CEDRIC) software (Mohr et al. 1986). The three dimensional wind fields were computed using the radial velocities from S-Pol and KGLD between 2318-0059[11] and from S-Pol and CHILL between 0106-0213 on 19 June. For all analysis times on 22 June, radial velocities from CHILL and KGLD were used in the wind synthesis. The speed and direction of storm movement were manually calculated for each case and used for the advection parameters in the synthesis. The vertical velocities in both cases were obtained using a variational integration of the continuity equation (O'Brien 1970).

The polarimetric data from CHILL and S-POL were edited, gridded, and used in a fuzzy-logic hydrometeor classification algorithm (hereafter FHC), adapted from Liu and Chandrasekar (2000) and Straka et al. (2000), using the same methodology as in Tessendorf et al. (2005). The temperature sounding used in the FHC for 19 June was from the 0145 (20 June) National Severe Storms Laboratory (NSSL) Electric Field Meter (EFM) balloon sounding, and from the 0038 (23 June) NSSL EFM sounding for 22 June. As in Tessendorf et al. (2005), hydrometeor echo volumes were also calculated for each radar scan time by multiplying the number of grid points that satisfied the FHC category of interest by the volume of a grid box (0.125 km^3).

2.2 Lightning data processing

The New Mexico Tech LMA measures the time and three-dimensional location of very high frequency (VHF) radiation sources emitted by lightning discharges. For a

[11] Except at 0019, when S-Pol and CHILL were used in the absence of a KGLD volume scan near that time.

given lightning flash, the LMA may locate hundreds to thousands of such sources resulting in detailed maps of the total lightning activity. To interpret these data, we use the bi-directional discharge model (Kasemir 1960, Mazur and Ruhnke 1993), as described in Wiens et al. (2005). To determine total (intra-cloud plus CG) flash rates from the LMA data, we used an algorithm developed at New Mexico Tech (Thomas et al. 2003) that sorts the LMA sources into discrete flashes.

CHAPTER 3

ENVIRONMENTAL CONDITIONS AND CASE OVERVIEWS

3.1 19 June 2000

A dry line had set up along the Colorado-Kansas border by 1000 the morning of 19 June 2000 with surface dew points 10-15 °C to the east of the dry line, and near 7 °C to the west of the line (not shown). A 500 hPa trough was situated over Utah, giving way to mid-to-upper-level southwesterly flow into the STEPS region. Surface temperatures were near 30 °C, but due to a very dry boundary layer the CAPE was near zero west of the dry line (Fig. 1). Surface winds were relatively weak, but mostly southerly ahead of the dry line, and westerly rearward of the dry line. A ridge in surface equivalent potential temperature was situated in north-central Kansas and into south-central Nebraska, further east of the STEPS domain (not shown).

By 2200 on 19 June 2000, a multicellular storm system developed near Colorado Springs, CO and was traveling to the northeast toward the STEPS domain. A new cell developed southwest of the CSU-CHILL radar around 2300 and was targeted by the STEPS operations center as a storm of interest (Fig. 2; hereafter storm 19A). By the beginning of the analysis period at 2318, this storm was already producing intra-cloud (IC) and mostly negative CG lightning (Fig. 2). The storm rapidly evolved while propagating to the northeast and was in its mature phase (see section 4.1) by 0000. It passed over the CSU-CHILL radar near 0030 and dissipated shortly thereafter. Near the

time of its dissipation, another group of cells was developing west of KGLD (hereafter storm 19B). These cells quickly began producing IC and mostly negative CG lightning, as they propagated to the northeast (Fig. 2). The cells of storm 19B eventually merged into an elongated storm by 0122, and between 0124-0154 there were three reports[12] of severe winds greater than 25 m s^{-1} associated with this storm, the latter of which was as high as 33 m s^{-1}. Storm 19B's peak in maximum updraft and graupel echo volume was observed around 0200 (see Fig. 6). Shortly after this time, the storm quickly dissipated, however, CG flash rates peaked right before dissipation.

3.2 22 June 2000

A trough line had set up in eastern Colorado by 1400 on 22 June 2000. Around 1900 a line of convection was observed on radar situated along the trough line and extending from northeastern Colorado into the Nebraska panhandle (not shown). A surface wind shift line was evident in the 2100 surface observations, in conjunction with the trough line, with southerly winds east of the line and northerly winds to the west of it. Surface temperatures in the STEPS domain were near 32 °C, with surface dew point temperatures near 10 °C (not shown). CAPE values, based on MGLASS soundings taken in the area, were near 500 J kg^{-1} (Fig. 3), which are modest for the region given the mean CAPE in June ranges between 800-1200 J kg^{-1} according to Grumm et al. (2005).

Near 2330 on 22 June 2000, a cell on the southern end of the line of convection entered the western portion of the STEPS radar network. This cell dissipated by 0000, but a new cell directly to its southeast developed by 2356 (Fig. 4; hereafter cell 22A). No CG flashes of either polarity were observed in cell 22A. Another convective cell was

[12] Storm reports were retrieved from Storm Data online, maintained by the National Climatic Data Center.

also observed at this time just north of the CSU-CHILL radar, propagating to the northeast (hereafter cell 22B). A few positive and negative CG strikes were observed with cell 22B (Fig. 4). These two cells began to merge at 0009 (hereafter the product of cells 22A and 22B will be referred to as cell 22AB). During the merger process, the storm only produced negative CGs on its far eastern flank, but about 10 minutes after their merger, a peak positive CG flash rate near 10 min^{-1} was observed (see Fig. 8). Just after the peak in positive CG flash rate, the peak total flash rate was observed near 500 min^{-1}. Between 0000-0030, hail up to 1 inch and surface winds near 30 m s^{-1} were reported with this storm, according to Storm Data online. Beyond 0030, the storm remained a predominantly positive CG-producer until dissipation. Near the time of the merger, a new cell (hereafter cell 22C) developed to the south of cell 22AB. Beyond that time, cells 22AB and 22C continued to propagate to the east-northeast and evolved into a linear convective system (hereafter line 22ABC) near 0108. Another group of cells developed to the southeast of line 22ABC as it was dissipating near 0150. These new cells formed a linear convective system that propagated northeastward out of the STEPS radar network. The discussion from 22 June will focus on cells 22A, 22B, 22AB, and 22C.

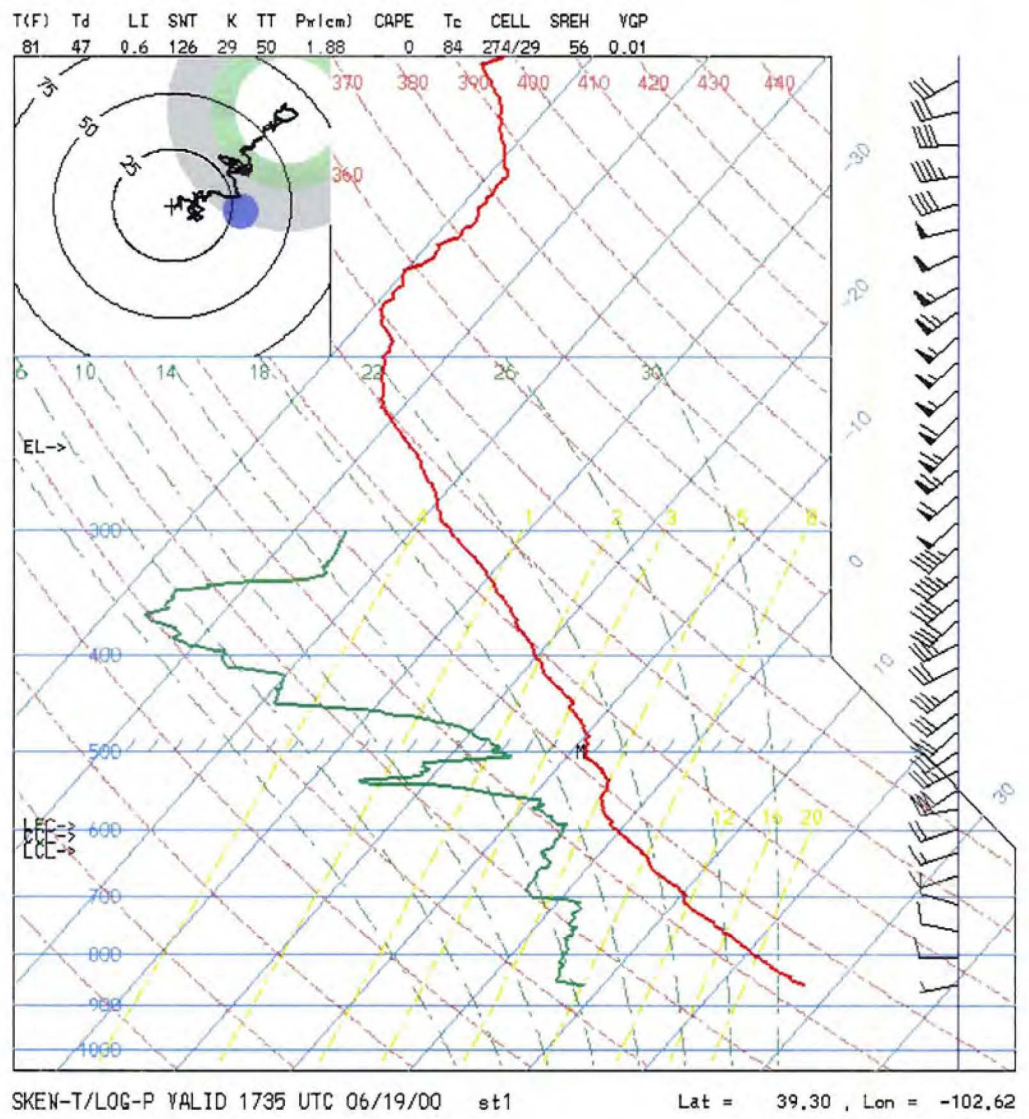

Figure 1. MGLASS thermodynamic sounding taken near Stratton, Colorado at 1735 UTC 19 June 2000.

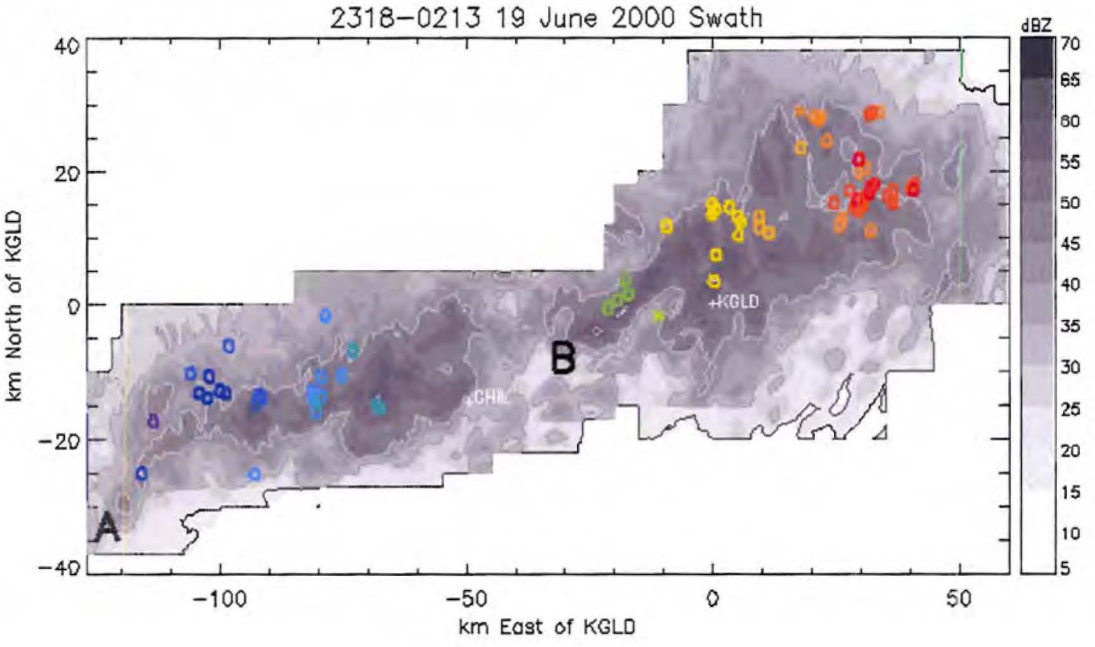

Figure 2. Swath of composite reflectivity (grayscale) from the S-Pol radar accumulated over the analysis period 2318-0213 on 19 June 2000. NLDN cloud-to-ground lightning strikes are overlaid with 'O' for negative strikes and 'X' for positive strikes and color-coded by time (progressing from blues to reds). The '+' symbol represents the locations of the radars. Cells A and B have been labeled for reference.

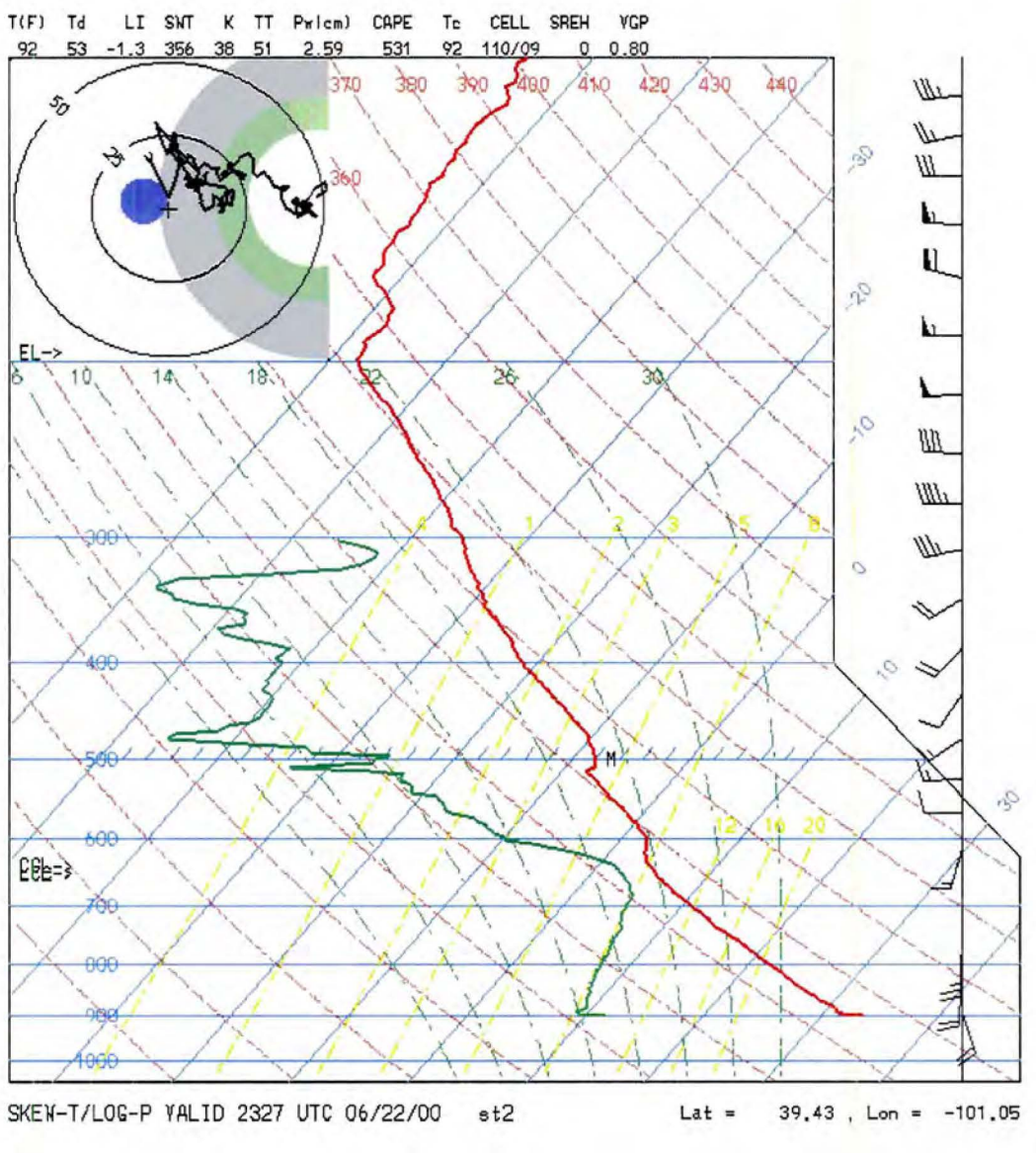

Figure 3. MGLASS sounding at 2327 UTC 22 June 2000 from near Goodland, Kansas.

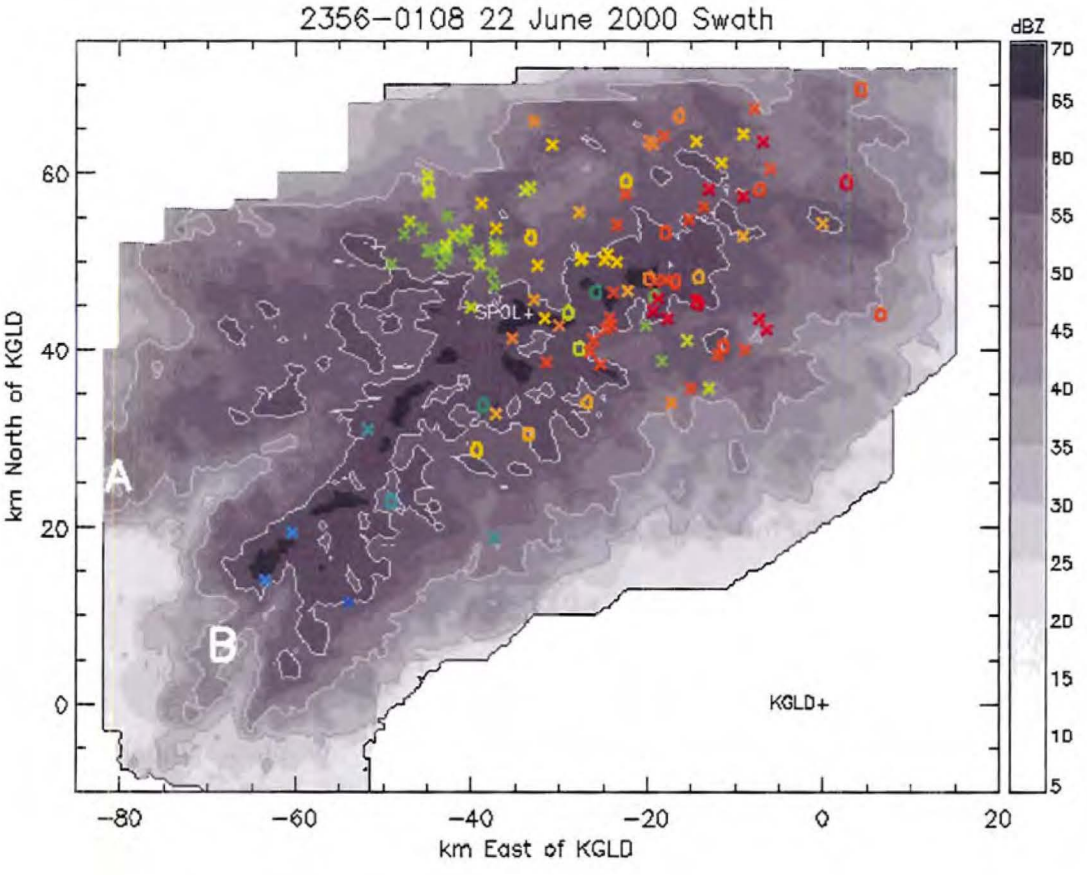

Figure 4. Same as Fig. 2, except of CSU-CHILL radar data accumulated over the analysis period 2356-0108 on 22 June 2000. Cells A and B are labeled for reference.

CHAPTER 4

KINEMATIC AND MICROPHYSICAL OBSERVATIONS

4.1 19 June 2000

Using the maximum updraft curve illustrated in Fig. 5, we define phases in each storm's lifecycle on 19 June, which we will refer to later in the text. Between the beginning of the analysis period at 2318 and approximately 0000, storm 19A was in a developing phase, with the maximum updraft in this phase around 10 m s^{-1} (Fig. 5). After this point, the maximum updraft began to increase indicating the beginning of storm 19A's mature phase, with a peak updraft of 15 m s^{-1} at 0025 (Fig. 5). After 0030, storm 19A entered its dissipating phase as the maximum updraft began to decline to around 6 m s^{-1} (Fig. 5). The maximum downdraft remained near 10 m s^{-1} into the dissipating phase (not shown). Storm 19A had essentially dissipated by 0052.

At 0044, storm 19B began to develop and was targeted by the STEPS radar network. It remained in its developing phase until 0142 when its maximum updraft quickly increased to near 10 m s^{-1} (Fig. 5). Storm 19B's mature phase (from ~0142-0208) was fairly short-lived, and had a brief maximum updraft of 18 m s^{-1} just after 0200 (Fig. 5). The maximum downdraft in storm 19B peaked at 11 m s^{-1} during its mature phase, and was also short-lived (not shown). Storm 19B rapidly dissipated after 0208. The storm updraft volume exceeding 10 m s^{-1} (hereafter, UV10) was very small in these

storms, comprising no more than four percent of the total storm volume greater than 0 dBZ, and peaking during the mature phases of each storm (Fig. 6).

Graupel was already detected at the beginning of the analysis period in storm 19A by the FHC algorithm, and graupel echo volume (hereafter, graupel EV) continually increased until 0025, during storm 19A's mature phase (Fig. 6). After this point, the total graupel EV dramatically declined[13]. Most of the graupel EV was centered around 6 km MSL[14] (corresponding to a temperature near –10 °C) until around 0030 (Fig. 5). After that time, during the dissipating phase of storm 19A, the center of the graupel echo lowered to near 5 km. In the developing phase of storm 19B, the graupel echo was centered around 4 km (T ~0 °C) and the total graupel EV began to rapidly increase (Figs. 5-6). This rapid increase began ~30 minutes prior to the beginning of the mature phase of storm 19B (indicated by increased UV10 or maximum updraft), suggesting that at least part of the graupel EV detected within the boundaries of storm 19B at those times might have been from graupel grown in nearby convection and advected (or seeded) into the storm. This is suggested because the kinematics of storm 19B at that time were likely not sufficient to support growth of hydrometeors into the observed quantities of graupel, and the convection on this day was multicellular making it both difficult to isolate the storm volume of storm 19B from nearby convection and more likely that hydrometeors could be advected from one storm to another. The total graupel EV reached its greatest peak at

[13] The dramatic decline is partially an effect of how the volumetric statistics were calculated. The two storms (19A and 19B) overlapped for about 20 minutes between 0044 and 0052 UTC. Thus, at 0044 UTC the total volume in which statistics are calculated increased to include the newly developing cells. At 0059, storm 19A had dissipated such that its volume was no longer included in the statistics calculations, resulting in a dramatic reduction in total volume since the new cells were still quite small. Nonetheless, storm 19B rapidly grew and attained volumetric statistics in par with storm 19A a short time later.

[14] All heights hereafter will be in kilometers above Mean Sea Level (MSL).

0155 during the mature phase of storm 19B, by which time the center of the graupel EV had also risen to 5 km.

The total hail echo volume (dominantly small hail) was negligible in this storm except for limited amounts detected near 7 km at 0010-0020 during storm 19A's mature phase, coincident with the local maximum in updraft speed of 14 m s^{-1} and peak in UV10 (Figs. 5-6). For the most part, hail echo volume (hereafter, hail EV) was only detected near 3 km in the lowest portions of the storm, which is somewhat suspect due to possible bright band (surface wetting) effects (Fig. 5). As graupel particles fall through the melting level near 5 km and begin to melt, the wet coating on the ice enhances the backscattered power, giving the graupel just below the melting level higher radar reflectivity. This FHC algorithm could possibly misclassify these melting graupel particles as small hail.

The total lightning flash rate (hereafter LFR) was around 10 min^{-1} at the beginning of the analysis period, and increased to near 60 min^{-1} by 0019 during storm 19A's mature phase, coinciding to the time when graupel EV peaked (Fig. 6). LFR declined for about 10 minutes around 2350, though a similar decline was not seen in the graupel EV trend (see Fig. 6). Both graupel EV and LFR decreased after 0019, and then the LFR began to rise again in storm 19B around 0052, when the total hail EV was also beginning to rise again (Figs. 5-6). Graupel EV rapidly increased a short time later and peaked at the same time as the LFR and hail EV at 0122, but the graupel EV continued to rise beyond this time, while LFR and hail EV both declined until the end of the period. Considering that this storm system was quite complex and rapidly evolving, it is difficult to rigorously interpret the relationships presented in these time series. Nonetheless, the

observations indicate that, for the most part, LFR followed the behavior of graupel EV in storm 19A, while LFR seemed to follow the behavior of hail EV in storm 19B.

The CG flash rate was relatively low, but steady, throughout storm 19A and storm 19B, until the demise of storm 19B when it approached 4 min^{-1} (Fig. 6). There were, however, a few periods that lacked CG flashes: 0014-0021, 0040-0100, and near 0140 (Fig. 6). These periods will be discussed in more detail in Chapter 5.

4.2 22 June 2000

The storms on 22 June 2000 were already nearing their mature phase in the beginning of the analysis period (when radar observations became available), and they remained in a mature phase for the duration of the analysis period, therefore we will not make reference to storm evolutionary phases in the following discussion. At the beginning of the analysis period at 2356, the maximum updraft was already 30 m s^{-1} in both cells 22A and 22B (Fig. 7). By 0010 when cells 22A and 22B were beginning to merge, the maximum updraft quickly increased to 45 m s^{-1} near the apex of the merger, and maintained these speeds for almost an hour. By the end of the analysis period, the maximum updraft was observed near 50 m s^{-1} in cell 22C, while it had weakened to near 30 m s^{-1} in cell 22AB. The graupel EV maximum was centered around 6 km (T ~ -10 °C) until 0050, when its maximum deepened to between 5-9 km (Fig. 7). Graupel EV reached its maximum at the end of the analysis period, at the same time the updraft was also at its maximum speed. Graupel EV reached heights up to 16 km at times, indicating a very deep convective storm with substantial updrafts. The hail EV maximum was centered around 8-9 km and peaked between 0010-0050 (Fig. 7).

Graupel was already indicated by the FHC algorithm at the beginning of the analysis period (Fig. 8). As mentioned above, graupel EV peaked at the end of the analysis period and was not coincident with the peak in UV10, which peaked near 0025 (Fig. 8). The peak in UV10 was coincident with the peak in CG flash rate (mostly positive CGs) and hail EV. UV10 decreased after 0025 until the end of the analysis period. What appears to have happened is that as cell 22AB began to dissipate and lose UV10, the hail fell out. However, during this same time, the maximum updraft in cell 22C was very high, but its updraft volume was lower relative to cell 22AB. Thus, the total hail EV seems to relate more to UV10 than maximum updraft. This is consistent with studies by Nelson (1987) and Tessendorf et al. (2005) who show that the area of strong updraft is also important for hail growth, in addition to the maximum updraft speed that typically governs the maximum hail size.

The total LFR was already near 150 min^{-1} at the beginning of the analysis period, and rapidly increased to around 400 min^{-1} by 0010, coincident with the beginning of the cell merger process (Fig. 8). The LFR peak, which occurred just after 0030, within 10 minutes after the cell merger, was very impressive at approximately 500 min^{-1}. LFR had a very similar trend as graupel EV (Fig. 8), which would be expected since ice-ice collisions have been shown to be important in charging processes (Takahashi 1978). The lower temporal resolution of the radar data to that of the LMA lightning data likely contributes to the smoother appearance of the graupel EV curve relative to the LFR trend.

The positive CG flash rate was typically 1-3 min^{-1}, except during its peak at 0025 (just after cells 22A and 22B merged) when it reached 10 min^{-1} (Fig. 8). This is similar to the Spencer, SD storm studied by Carey et al. (2003), where CG flash rates increased

dramatically immediately following the merger of two storms. Between 0011-0022, during the cell merger, the positive CG flash rate was zero, and only negative CG flashes were observed. The negative CG flash rate during this time was at its peak (3-4 min^{-1}; (Fig. 8). The negative CG flash rate was typically 1-2 min^{-1} before and after this time period (Fig. 8). More details on the charge structure and the location of the negative CGs between 0011-0022 and the positive CGs in the positive CG flash rate peak near 0025 will be discussed in Chapter 5.

4.3 Summary

The most dramatic differences between 19 June and 22 June were the disparity in updraft strength, and updraft volume (UV10), and hail EV. The 22 June storm exhibited maximum updrafts as high as 50 m s^{-1}, greater than twice the strength of 19 June (see Figs. 5, 7). The UV10 values in 22 June were also two orders of magnitude larger than in 19 June for two reasons: 19 June rarely exhibited updraft speeds greater than 10 m s^{-1} and were comparatively narrow in width compared to 22 June (see Figs. 6, 8). The 22 June storm exhibited similar maximum updraft speeds and UV10 values on the same order of magnitude as the 29 June PPCG STEPS supercell (Tessendorf et al. 2005). The hail EV in 22 June had a strong maximum near 8-9 km indicating the presence of large precipitation ice in the mixed-phase region of the storm, whereas in 19 June the hail EV was negligible throughout the storm. The 19 June convection was also not as deep as that on 22 June or 29 June (Tessendorf et al. 2005). Graupel EV typically was observed as

high as 15 km in the two PPCG storms of 22 and 29 June, whereas it was never observed above 10 km in 19 June (Figs. 5, 7).

The lack of hail in the 19 June storm can most likely be attributed to the lack of sufficient kinematics (i.e. updraft > 10 m s^{-1}) to support hail growth. Thermodynamic conditions may have prevented the 19 June storm from achieving stronger updrafts necessary for hail growth, since the CAPE west of the dry line (in the region where the 19 June storms formed) was near zero, compared to being near 500 J kg^{-1} on 22 June (see Figs. 1, 3). Furthermore, the surface inflow on 22 June was southerly to southeasterly bringing in much more humid air, compared to the surface westerlies on 19 June. Lastly, in addition to the weaker updrafts, the lower equilibrium level on 19 June could be another reason for the shallower convection that was observed.

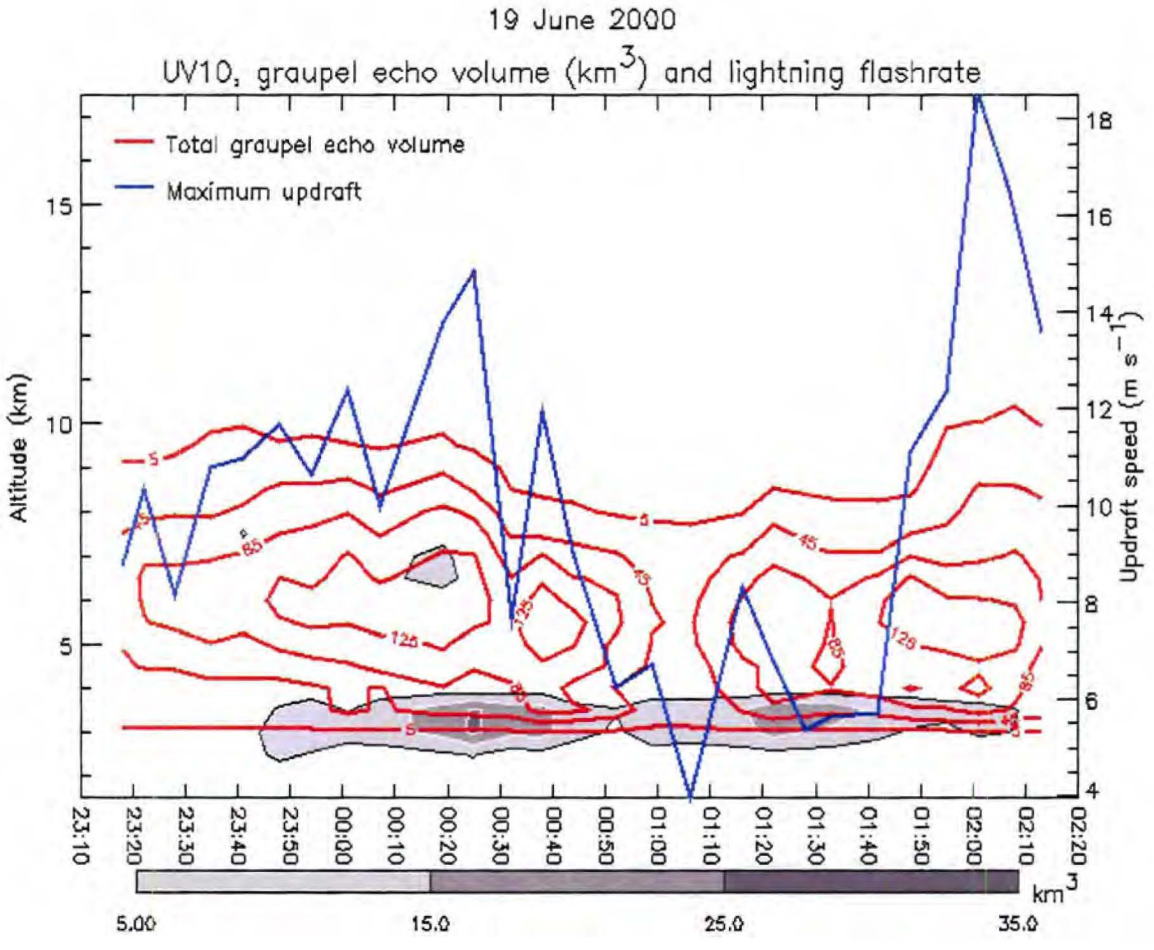

Figure 5. Time-height contours of total graupel echo volume (red contours) and total hail echo volume (gray shaded contours), and maximum updraft time series (values on right axis) for 19 June 2000. For reference, Storm A was observed from 2318-0052 UTC, and Storm B from 0044-0213 UTC.

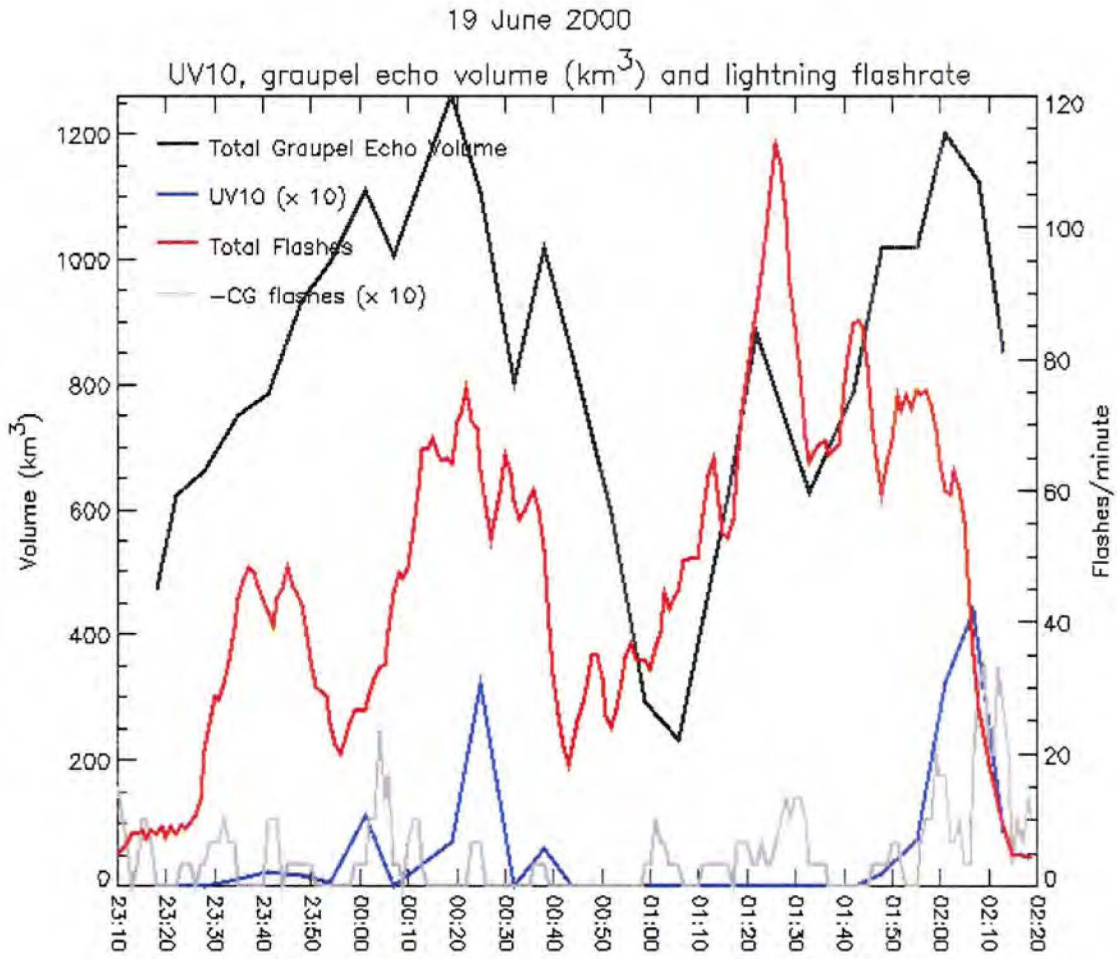

Figure 6. Time series of updraft volume greater than 10 m s^{-1} (multiplied by 10 to fit on left axis), total graupel echo volume (values on left axis), the counted lightning flash rate from the LMA data (values on right axis), and the CG flash rate (multiplied by 10 to fit on right axis) for 19 June 2000.

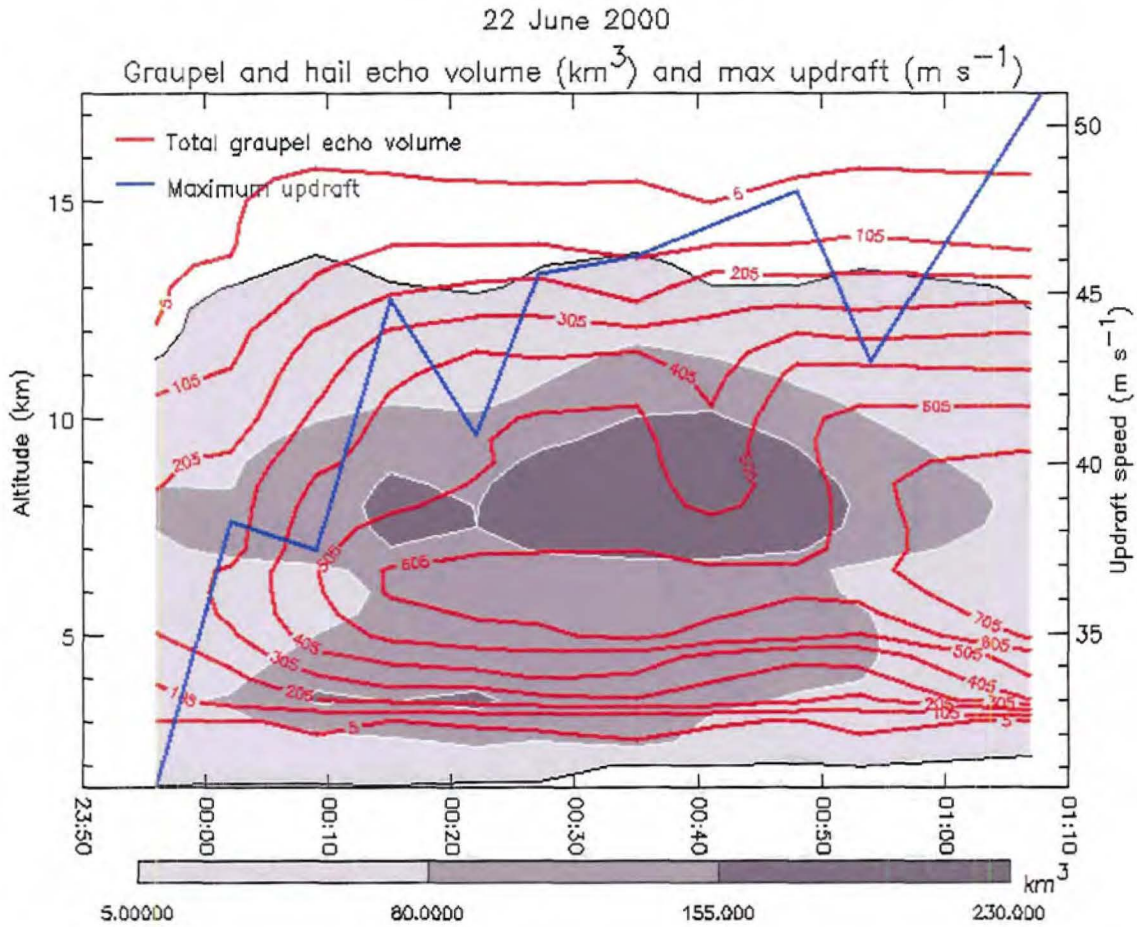

Figure 7. Time-height contours of total graupel echo volume (red contours) and total hail echo volume (gray shaded contours), and maximum updraft time series (values on right axis) for 22 June 2000. The statistics calculated in this time series include the volumes of both Cells A and B at 2356 and 0002, and of Cells AB and C for 0009-0108.

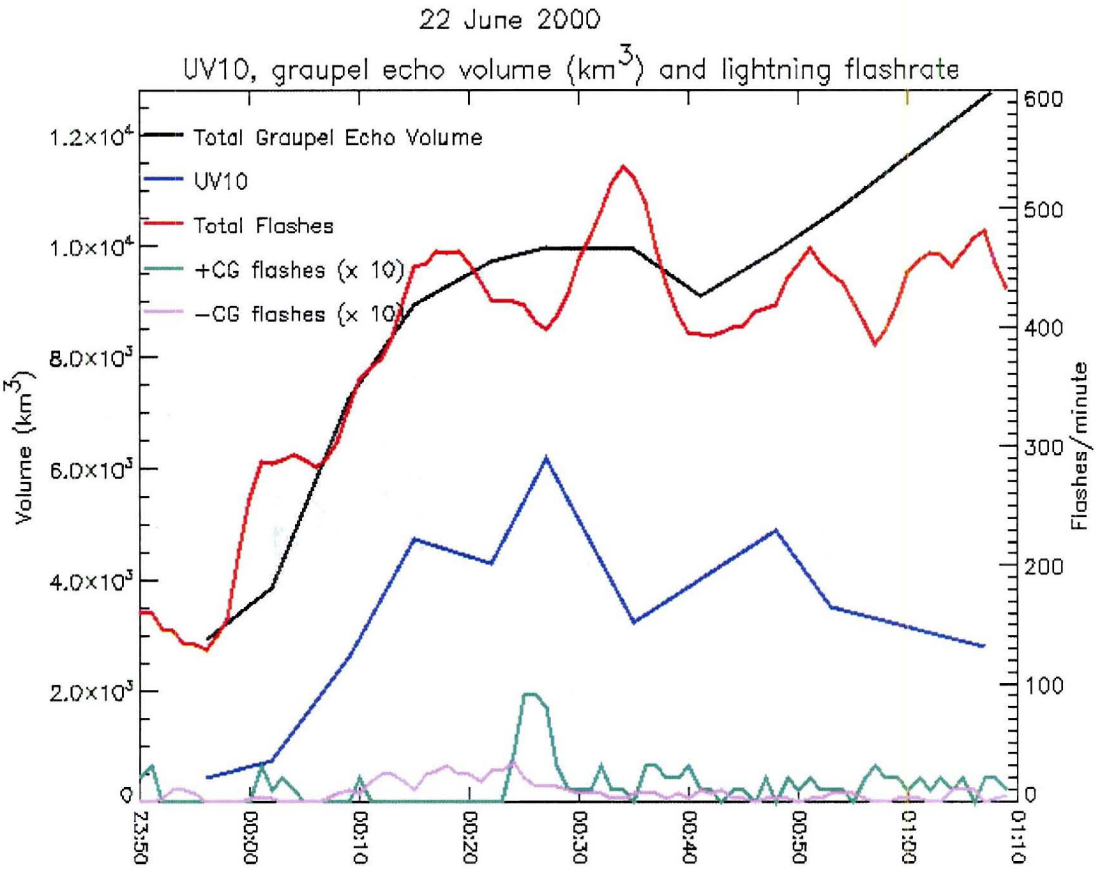

Figure 8. Time series of updraft volume greater than 10 m s^{-1} and graupel echo volume (left axis), total lightning flash rate from the LMA data (right axis), and the positive and negative CG flash rates (multiplied by 10 to fit on right axis) for 22 June 2000. The statistics include the same storm cell volumes as in Fig. 4.

CHAPTER 5

LIGHTNING AND CHARGE STRUCTURE

5.1 19 June 2000

In both storms 19A and 19B, IC flashes were most often observed by the LMA near the reflectivity core, initiating both at a height of 8 km and 5 km (not shown). Those initiating near 8 km typically propagated upward, with many more LMA sources above the initial height, than below. The IC flashes originating near 5 km typically propagated downward, with the majority of LMA sources below the initial height. This indicates a likely region of positive charge around 8-11 km, a main negative charge region around 5-8 km, and a lower positive charge layer below 5 km. This pattern is consistent with a "normal tripole" charge structure (illustrated in Fig. 9; Williams 1989). In Figure 9, the bulk of the LMA sources (which are most often associated with positive charge) were found distributed throughout the entire storm depth between 2-11 km (Fig. 9). This depiction of the charge structure is somewhat vague, given that some of those LMA sources are in an inferred negative layer near 7 km. In the less electrically active phases of the time series a dearth of LMA sources near 7 km is visible, however, coinciding with the height of the inferred negative charge region (Fig. 9). Nonetheless, flash-by-flash analysis is needed to better detect the true complexity of this storm's charge structure, in particular to identify that there was indeed an intervening negative charge layer near 7 km.

Figure 10 therefore illustrates the radar observations and charge structure during three flashes near 0019 in the mature phase of storm 19A, which were deemed representative of the charge structure in both storms. Horizontal cross-sections of reflectivity and vertical velocity show that the storm was multicellular, with multiple reflectivity cores, and the low-level updraft was east (ahead) of the advancing storm (Fig. 10). The vertical reflectivity structure of the storm 19A (which is similar to that of storm 19B) is shown in Figure 10c-d. The main updraft was east (ahead) of the storm and under an overhang in reflectivity. The charge structure in the reflectivity overhang (and main updraft) resembled a "normal dipole" with a main negative charge region centered around 7-8 km, and an upper positive charge region above at 9 km (Fig. 10c). In the core of the storm, a normal polarity tripole structure can be seen, with the additional lower positive region below 6 km (Fig. 10c). Once more in this projection, it is clear that most of the LMA sources were contained in a region with precipitation ice, such as graupel and small hail (Fig. 10d).

In the LMA data, negative CG lightning flashes usually initiated around 4-5 km and then propagated downward into what is inferred to be a lower positive charge region below the main negative region (the lower positive charge can be seen in Fig. 10, even though this figure only includes LMA sources from IC flashes). The presence of a lower positive charge region involved in the CG flashes supports the idea that a lower charge region, of opposite sign, may be needed to initiate CG lightning toward the ground[15]

[15] The few positive CG flashes associated with this storm system initiated around 5 km MSL and propagated upwards into a region of numerous LMA sources (and thus inferred positive charge) just above 5 km MSL, with relatively few LMA sources below yielding an inferred region of lower negative charge below 5 km MSL. This is also consistent with the aforementioned notion that CG lightning needs an oppositely charged lower charge region to initiate CG lightning toward the ground. These CG flashes occurred outside the storm core, and may have been the result of a lowering of the normal dipole charge structure in the storm periphery.

(Williams 1989, Williams et al. 1989, Williams 2001, Mansell et al. 2002, Marshall and Stolzenburg 2002, Wiens et al 2005).

No CG flashes were observed in the mature phase of storm 19A between 0014-0021; rather there were numerous IC discharges between the lower positive and main negative regions (see Figs. 6, 10). The LMA sources in the inferred lower positive charge region appeared vertically deeper and larger in area at this time as well. It is possible that since many more IC discharges were detected between the main negative region and the lower positive region, that there was an energetic preference for IC discharges around that time. We presume a similar explanation for the absence of CG flashes near 0140 in the mature phase of storm 19B.

Between 0017-0018, there was also a lightning hole observed in the LMA data (not shown), which has been associated with stronger updrafts and bounded weak echo regions (BWERs) in horizontal cross-sections of radar reflectivity (Krehbiel et al. 2000, Wiens et al. 2005). A weak echo region and the core updraft were coincident with this lightning hole (not shown), and it was also during the peak period of the maximum updraft (see Fig. 5).

For the period between 0040-0100, when there was no CG activity, the lower positive region was much less evident and thus the storm exhibited more of a normal dipole structure (see Figs. 6, 9). Again, this supports the notion that in order for there to be CG lightning, a lower charge region is needed.

5.2 22 June 2000

On 22 June, as seen in Figure 11, a maximum of LMA sources around 9 km was evident from the beginning of the analysis period. This generally corresponded to a relatively well-defined and persistent inferred positive charge layer at this height during this time period. After 0010, near the time of the cell merger, this maximum in LMA sources deepened and was more centered around 8 km, corresponding to a temperature of approximately −20 °C (Fig. 11). Flash rates at this point exceeded 400 min^{-1}.

As might be expected from the extraordinary flash rates on 22 June, the charge structure of this storm system was very complex, and discrete charge layers representative of the entire storm at any given time could not be realistically deciphered. However, we will attempt to describe the general charge structure that was seen in the LMA data, especially during periods of interesting CG activity. It is easier to do this if we discuss the charge structure of individual regions of the storm, in particular the eastern flank (i.e. overhang and anvil region), the northern and central portions (formerly cells 22A and 22B, respectively), and the southern portion (cell 22C; Fig. 12).

The eastern flank of the 22 June storm (i.e. the anvil area and reflectivity overhang) consistently exhibited an area of inferred positive charge between 7-10 km, with inferred negative charge above that at 10-12 km (Fig. 13c). The negative CGs associated with this storm, especially in the period between 0011-0022 when negative CG lightning dominated, were primarily located in the far eastern flank of the storm, under this inverted dipole. The CG flashes typically originated from 9-10 km, tapping the upper negative charge. Reflectivity in the anvil area was fairly low (less than 20 dBZ; Fig. 13c), and unfortunately the scan sector from CSU-CHILL did not include this

portion of the storm to identify hydrometeors via polarimetric radar observations (specifically vertically oriented ice would have been of particular interest). However, the core of the storm was mostly graupel echo with some small and large hail (Fig. 13d).

Figure 13 also shows the time when cells 22A and 22B had just begun to merge, and when cell 22C was originally detected south of the cell 22AB merger (near x = -55, y = 10). The low-level wind vectors clearly show a region of convergence along the apex of the cell merger, with westerly motion in Cell 22A and southerly winds in Cell 22B (Fig. 13a). The updrafts are also organizing along this convergence line, and a broad region of updraft greater than 10 m s^{-1} is evident at 7 km (Fig. 13b).

Cell 22A (the northern portion of the 22 June multicell) had multiple charge layers, and no CG activity until 0024. A generalization of this charge structure from 2350-0020 could be termed a double dipole or a normal tripole with an extra upper negative layer. More specifically, inferred negative charge was present above 10 km, inferred positive charge resided between 8-10 km, another layer of inferred negative charge was observed between 6-8 km, and a second layer of positive charge resided between 4-6 km (Fig. 14c). Four-layer charge structures have also been documented by Stolzenburg et al. (1998) within convective updraft regions. By 0010 (the beginning of the merger with cell 22B), the charge layers in the eastern portion of cell 22A became more complex and difficult to discern. However, positive charge was observed over a considerable depth (between 4-10 km) in the eastern portion of the storm core, where the broad new updraft was developing and ingesting mm-sized drops (see Figs. 14-15). A four-layer structure was still evident in the western portion of the cell during this time. Also notice the similarities between the horizontal cross-sections of radar reflectivity

seen in Figure 14 and the LMA source density in Figure 12. This implies that, to some degree, the LMA source density could be a proxy for radar reflectivity.

By 0024, the cell merger was complete and the northern portion of cell 22AB (formerly cell 22A) was producing abundant positive CG lightning (Fig. 16). These positive CGs typically originated around 7 km and typically came to ground below a region of inferred lower negative charge[16]. Figure 16 illustrates the radar structure during the time of peak positive CG lightning production. In Fig. 16a, it is apparent that cells 22A and 22B have merged into a large cell, with cell 22C at the southernmost tip. The updraft is on the eastern (leading) flank, still in a region of low-level wind convergence, and the positive CG lightning activity is clustered in the northernmost region of this storm (formerly cell 22A). Very high reflectivities (> 60 dBZ) are now evident aloft (at 7 km in Fig. 16b), indicating substantial precipitation ice aloft (also corroborated by FHC; not shown). A reflectivity overhang is still apparent, surrounding the main updraft (greater than 25 m s^{-1}), in Figure 16c. In a vertical projection, it is clear that the cluster of positive CG strikes comes to ground below the main reflectivity core, where lower negative charge was observed and hail was detected to be falling out of the storm (Fig. 16c-d).

The central portion of the analysis area (and formerly cell 22B) had a general inverted charge structure (see Fig. 13c). Upper negative charge was inferred between 9-12 km, with a region of main positive charge between 6-9 km, and lower negative charge

[16] As described in Wiens et al. (2005), positive breakdown is less noisy at LMA frequencies and therefore is not detected as well with the LMA. In addition, with the high flash rates observed in this storm system, it was difficult to assess the initiation height and charge layers associated with each positive CG flash. Negative breakdown associated with negative CG flashes was detected much better with the LMA and thus we are much more confident with our estimates of flash initiation height and associated charge layers in those cases.

from 4-6 km (the lower negative charge is not evident in the flashes shown in Fig. 13). Few CGs were observed within this portion of the storm, but those that were observed (in the first 20 minutes of the analysis period) were of positive polarity. By 0015, shortly after cell 22B merged into cell 22A, the charge layers were much more complex. Nonetheless, as in the former region of cell 22A, there seemed to be a much deeper positive charge region at this point (from 5-10 km).

Cell 22C exhibited a fairly persistent inverted tripole charge structure throughout the analysis period. Upper negative charge was inferred between 10-12 km, main positive charge between 6-10 km, and lower negative charge between 4-6 km (not shown). The charge structure of cell 22C and the eastern flank/anvil of this storm system exhibited much more straightforward and persistent charge layers. Even cells 22A and 22B exhibited relatively simple charge layers prior to their merger. It was evident that the charge layers in cells 22A and 22B became more complex after they merged into cell 22AB, perhaps because the total LFR nearly doubled during this time and charge deposition from lightning can add complexity to observed charge structures (Coleman et al. 2003), but overall a much deeper layer of positive charge was observed. In addition, flash start heights (indicating the height between two opposite charge layers where the electric field is enhanced and bi-directional breakdown initiates) broadened after the merger, possibly suggesting that there were more dipoles present to initiate IC flashes post-merger (not shown).

5.3 *Summary*

The 19 June storm consisted of weaker, shallow convection and produced little-to-no hail and average total flash rates on the order of 10 min^{-1}. The cells in the 22 June storm were more vigorous, exhibited strong, broad updrafts, and produced large quantities of hail, as well as having extraordinary total flash rates on the order of 100 min^{-1}.

The LMA data indicate that the charge structure of the 19 June storms was consistent with a normal polarity tripole, and both storms 19A and 19B produced predominantly negative CG lightning. The negative CG lightning in these storms typically originated near 5 km, between an inferred main negative region and a lower positive charge region. Furthermore, during the mature phases of 19A and 19B, brief lulls in the (negative) CG flash rate were observed, causing the IC:CG ratio to become infinite. These lulls appeared to have excess IC flashing in between the lower positive and main negative charge regions. The LMA-inferred charge structure in the 22 June cells was typically an inverted tripole, and the positive CG lightning on 22 June generally occurred in regions with a midlevel layer of positive charge and a lower layer of negative charge, though not all positive CGs on this day could be identified in the LMA data with confidence (see section 5.2).

The negative CG lightning observed in the 22 June cells was typically under the anvil in a region with an *inverted* dipole charge structure. The negative CGs originated around 9 km between the upper negative and main positive charge layers of the inverted dipole. Though having CG flashes come to ground below the main dipole, rather than just having IC flashes within it, is somewhat contrary to our statement that lower opposite

charge below the dipole (i.e. a tripolar structure) is needed for a CG flash (see Section 5.1), there is still some consistency. Primarily, the bottom layer of the dipole was a layer of positive charge, which was detected below the negative charge in these *negative* CGs, suggesting a "lower" opposite charge layer was present. Secondarily, perhaps the reason that these flashes came to ground, instead of remaining an IC flash, was because the strength or depth of the "lower" positive charge was weak relative to that of the upper negative charge, such that the positive charge was quickly neutralized and the discharge continued to propagate to ground. This latter condition may have been more common in the anvil than in the core of the storm, explaining the prevalence of negative CGs under the anvil.

In cell 22A's early charge structure, four alternating layers of charge (with positive charge as the lowest layer) were observed, such that this could be termed a 'double dipole' or normal tripole plus an additional negative layer at the top (Fig. 14). This charge structure was also seen in the early developing phase of the 29 June supercell (Wiens et al. 2005). In the 19 June case, we observed the normal tripole, but we did not observe the fourth (upper negative) layer, perhaps because the storm was too shallow. The heights of the charge layers between the normal tripole of 19 June and the lowest three layers of the four-layer structure in 22 June were very similar. It appears that the four-layer charge structure of the positive CG cases (22 June and 29 June) evolved into a more general inverted tripole just prior to the onset of frequent positive CG activity. One might consider that the 22A storm charged normally and then, by some means, evolved into an inverted tripolar structure (see Chapter 6 for speculation on the processes

affecting this evolution). In cells 22B and 22C, however, an inverted tripole structure was observed from the beginning of the analysis period.

Stolzenburg et al. (1998) showed observations of four charge layers in convective updrafts and six layers outside of updraft regions. The charge layers outside the updraft were certainly not as organized (or perhaps just more complex) than in the updraft regions, especially in the high flash rate cases of 22 June and 29 June (see Wiens et al. 2005), and therefore the six plus layer model might still be valid. However, the LMA observations show a general tripole charge structure in each of the cases outside of the updraft, especially once the storms became mature, while inside the updraft region the lowest charge layer of the tripole was either absent or not involved in any lightning flashes and the remaining dipole was somewhat elevated compared to the layers observed outside the updraft (see Figs. 10, 13, 14, 16). One possible explanation for this difference in our observations is that the local electric field can be altered by the actual lightning activity (via charge deposition) and the charge structures inferred from EFM balloon soundings may reflect those transient changes (Coleman et al. 2003). The LMA observations indicate the heights of the radiation sources involved in each flash, and the charge structure is then inferred following the methods outlined in section 2.2. Thus, in our opinion, the LMA charge structure observations give a more general picture of the charge structure than the EFM balloon soundings alone.

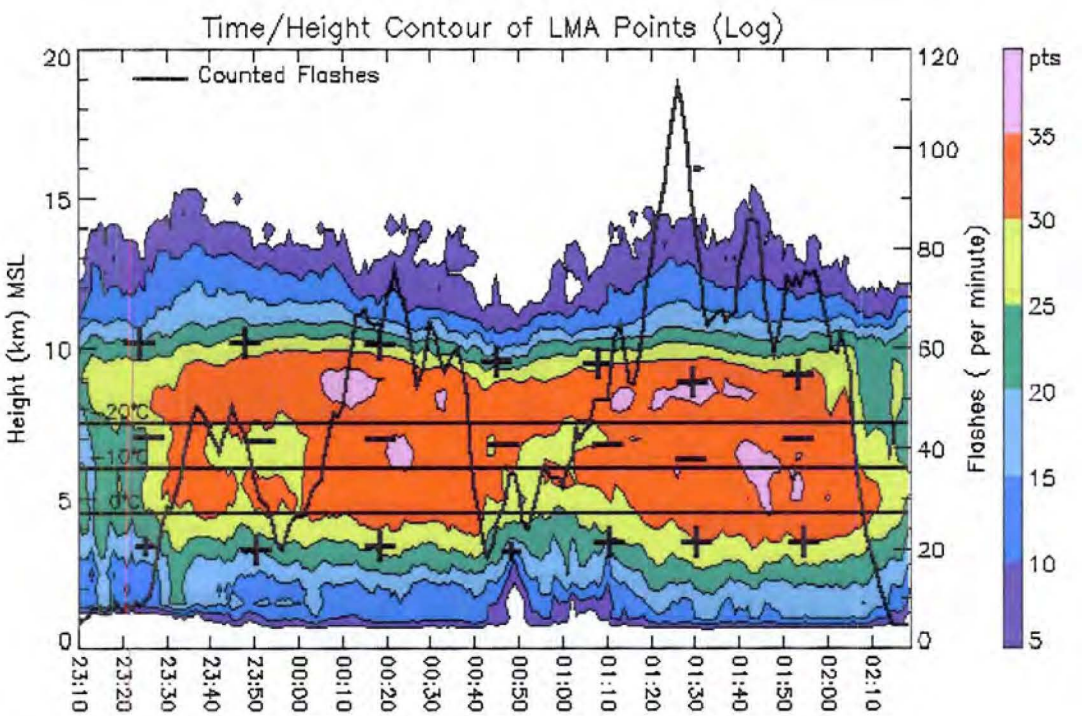

Figure 9. Time-height contours of the total number of LMA sources (color-shaded in logarithmic units) with the total flash rate time series overlaid in black for 19 June 2000. Plus and minus symbols indicate LMA-inferred gross charge structure. Smaller plus symbols indicate a smaller region of lower positive charge, versus a relatively larger region during times with a larger lower plus symbol.

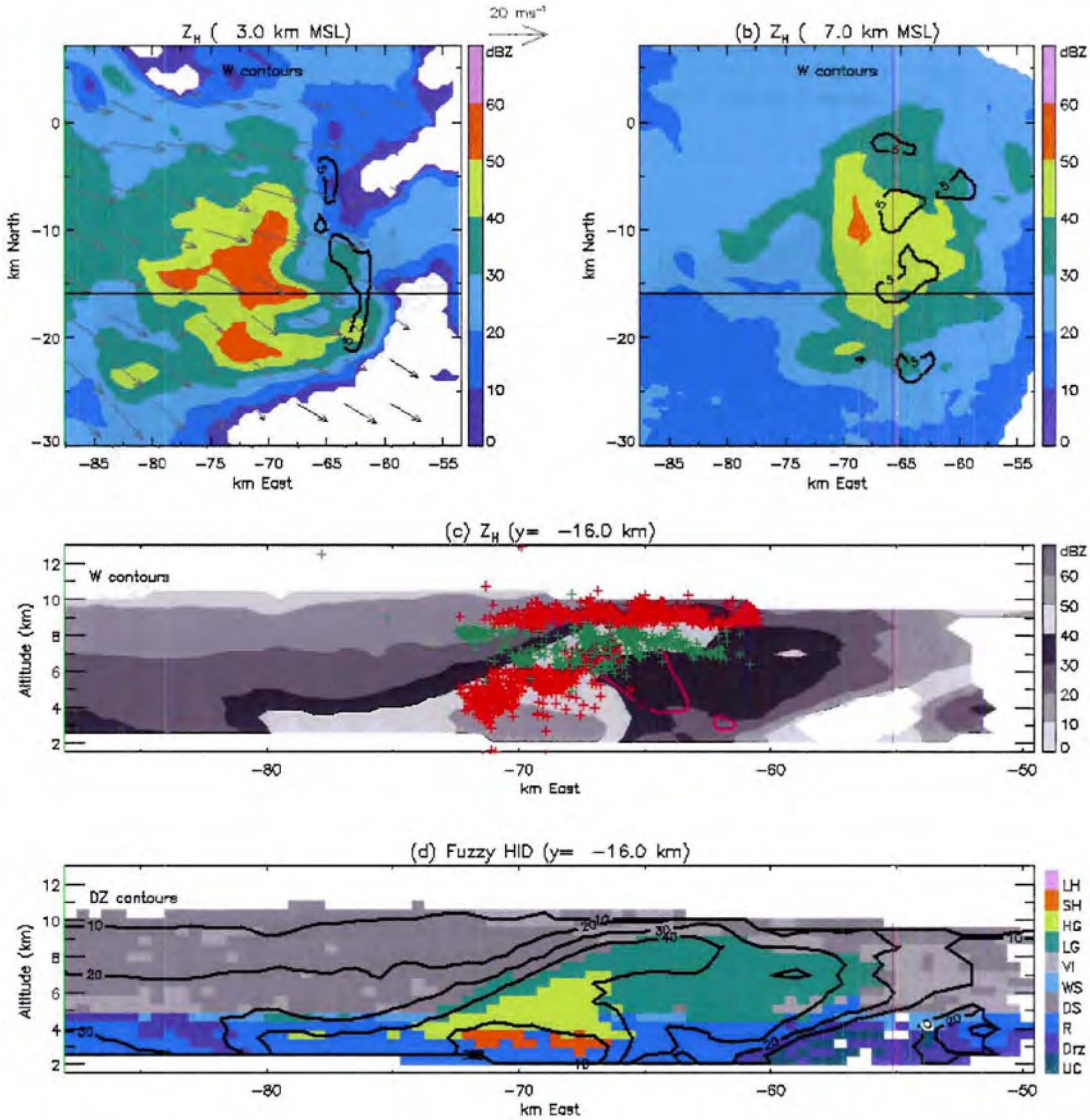

Figure 10. S-Pol reflectivity at 0019 on 20 June 2000 at (a) z = 3 km MSL and (b) z = 7 km MSL, with updraft contours at 5 m s^{-1} overlaid in black, and (c) y = -16 km in grayscale with updraft contours at 5 m s^{-1} overlaid in pink. FHC at y = -16 km with reflectivity contours every 10 dBZ, beginning with 10 dBZ, overlaid in black is displayed in (d). Ground relative wind vectors are overlaid in gray in (a). LMA sources from three representative flashes between 00:19:14-00:19:17 are overlaid as positive (red) and negative (green) charge in (c).

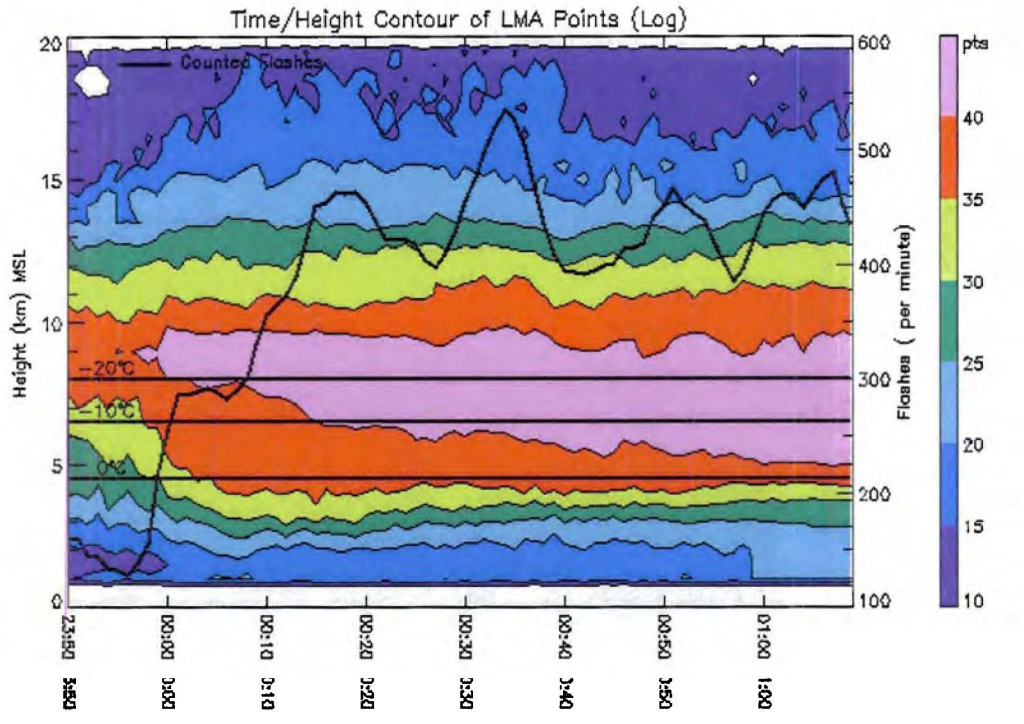

Figure 11. Time-height contours of the total number of LMA sources (color-shaded in logarithmic units) with the total flash rate time series overlaid in black for 22 June 2000.

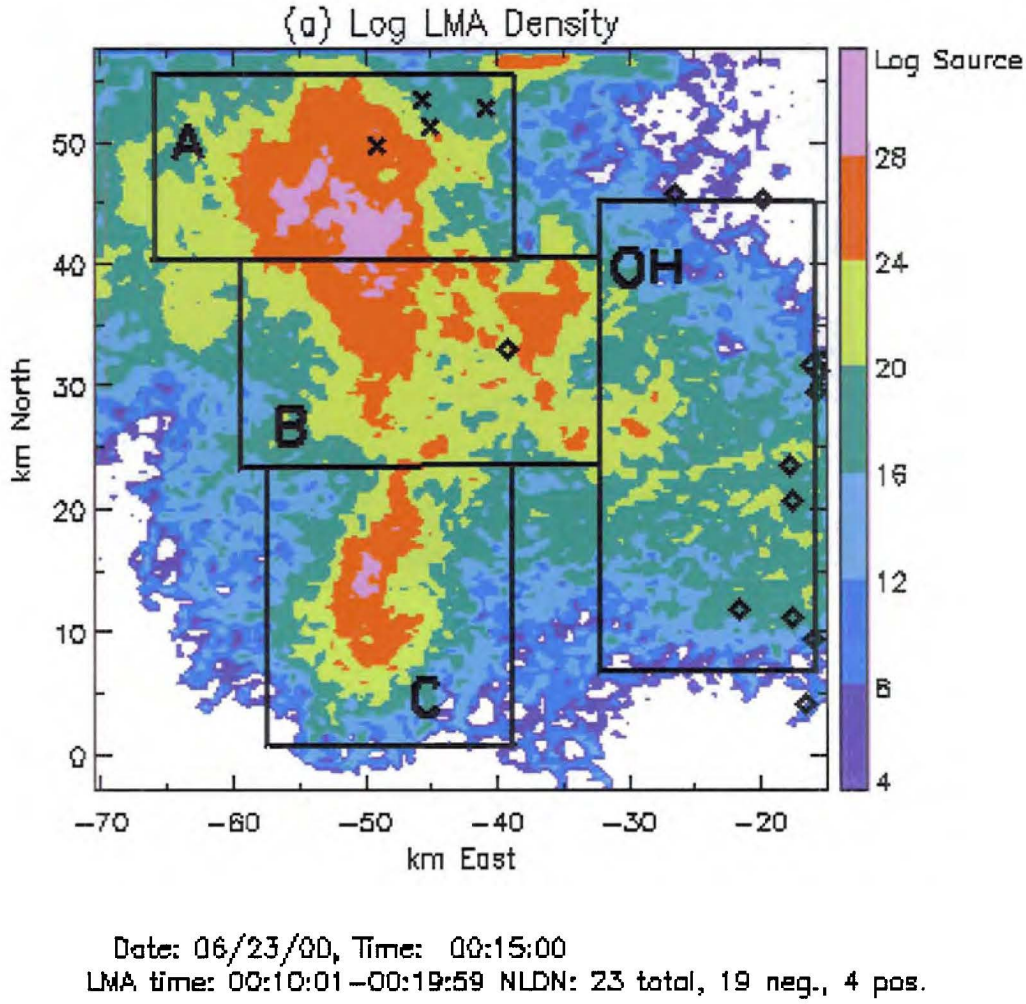

Figure 12. Plan view of LMA source (log) density between 0010-0020 on 23 June 2000. NLDN strikes during this 10-minute period are overlaid in black as 'x' for positive and a diamond for negative. Regions are labeled as cells A, B, C, and the overhang (OH) for reference to the discussion in the text. Cells A and B are merging during this time period.

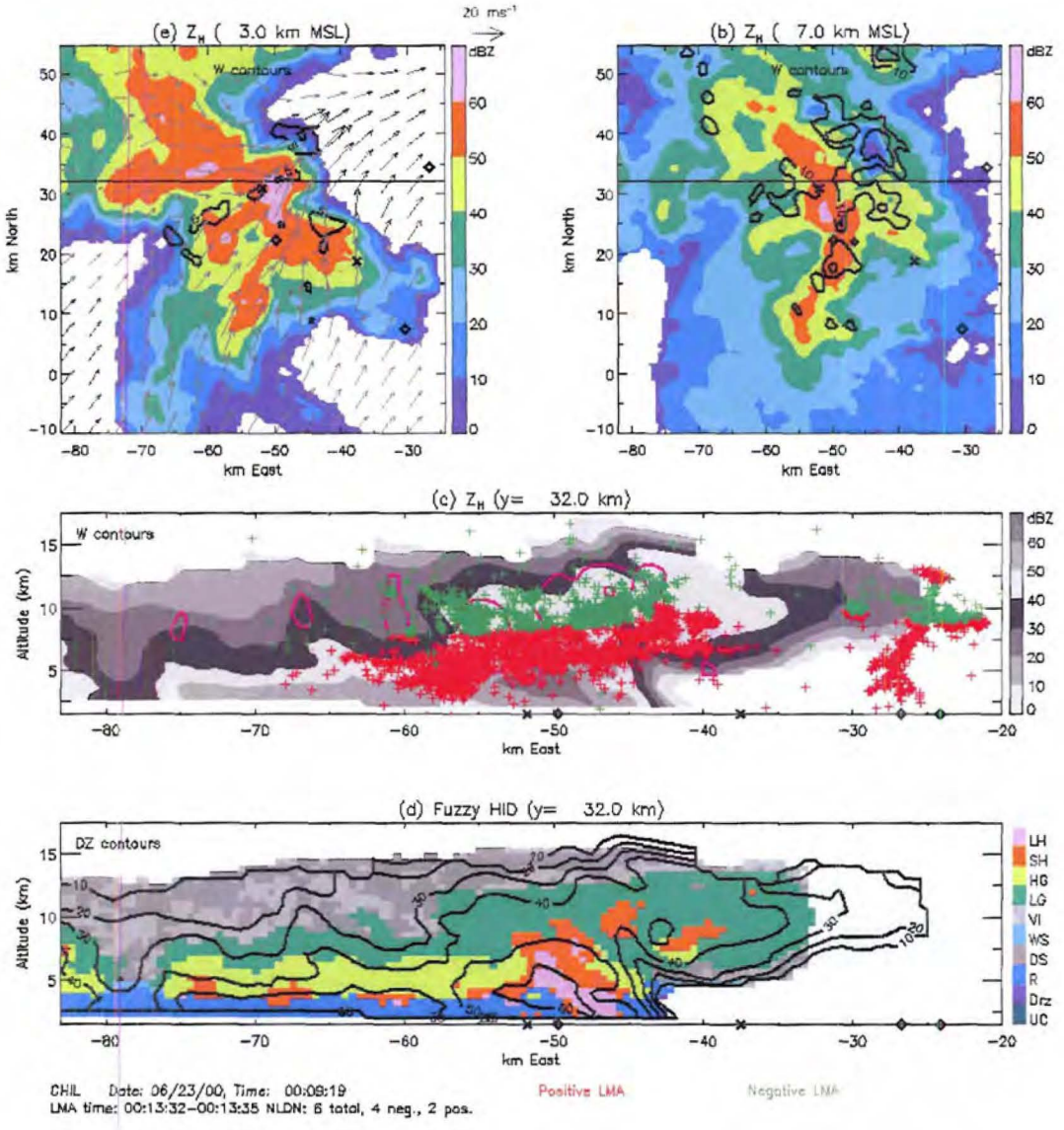

Figure 13. KGLD reflectivity at 0009 on 23 June 2000 at (a) z = 3.5 km MSL with black updraft contours at 5 m s^{-1}, (b) z = 8 km MSL with a black updraft contours every 10 m s^{-1}, beginning with 10 m s^{-1}, and (c) y = 32 km in grayscale with pink updraft contours every 10 m s^{-1}, beginning with 10 m s^{-1}. FHC (from CSU-CHILL) at y = 32 km with KGLD reflectivity contours every 10 dBZ, beginning with 10 dBZ, overlaid in black is displayed in (d). Ground relative wind vectors are overlaid in gray in (a). LMA sources from approximately 7 flashes (including one negative CG) between 00:13:32-00:13:35 as positive (red) and negative (green) charge are overlaid in (c). NLDN strikes between 0009-0014 are overlaid in all panels, with a black 'x' for positive and black diamond for negative CG flashes.

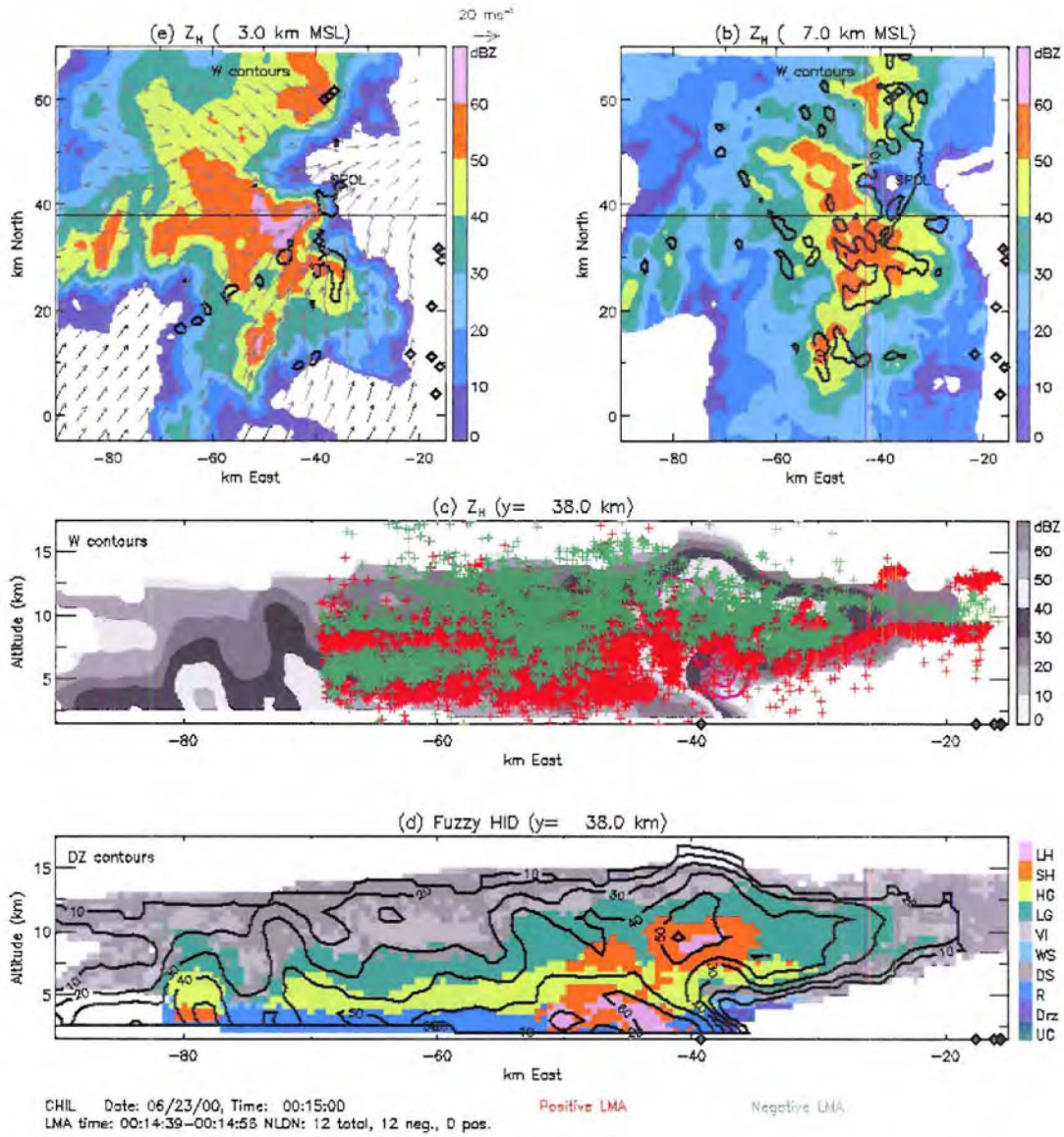

Figure 14. Same as Figure 13, except for at 0015 on 23 June 2000, only 10 m s^{-1} and 30 m s^{-1} contours are overlaid in (b), and y = 38 km in (c) and (d). LMA sources from approximately 30 flashes between 00:14:39-00:14:56 as positive (red) and negative (green) charge are overlaid in (c). NLDN strikes between 0015-0020 are overlaid in all panels, as in Figure 13.

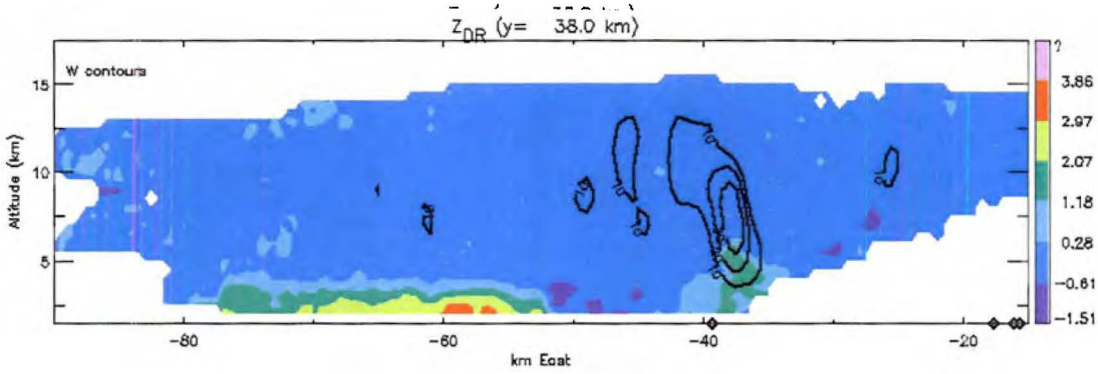

Figure 15. Vertical cross-section at y = 38 km (same as in Fig. 13) of differential reflectivity (Zdr) at 0015 on 23 June 2000, with black updraft contours every 10 m s^{-1}, beginning with 10 m s^{-1}.

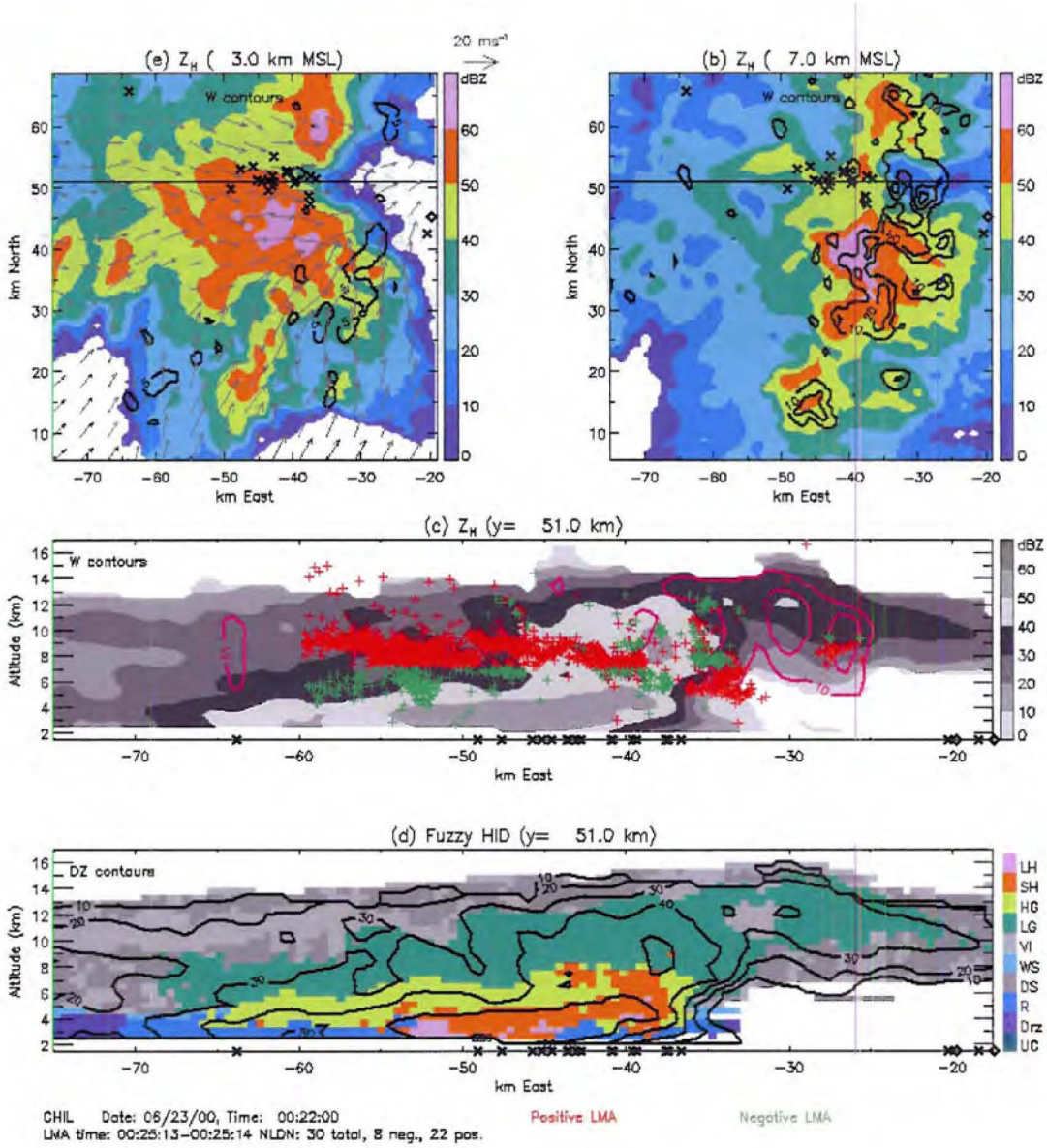

Figure 16. Same and Figure 13 except for at 0022 on 23 June 2000, and y = 51 km in (c) and (d). LMA sources from approximately 6 flashes (including one positive CG) between 00:25:13-00:25:14 as positive (red) and negative (green) charge are overlaid in (c). NLDN strikes between 0022-0027 are overlaid in all panels, as in Figure 13.

CHAPTER 6

DISCUSSION

Regardless of the polarity of the CG lightning observed in these two cases, and to the extent of our ability to detect the charge layers involved and/or present during the time of the CG flashes, a lower[17] charge layer of opposite polarity was present at all times when CG flashes were observed. This lower charge layer was also typically not seen in the updraft regions, but in the region of the precipitation (reflectivity) core in the vertical cross sections. When this lower opposite charge layer was not present, we did not observe CG flashes. Therefore, following the conclusions of Williams (1989), Williams et al. (1989), and Mansell et al. (2002, 2005), we conclude that the lower opposite charge layer may be necessary for a CG flash to come to ground.

However, CG flashes were not always observed when the lower opposite charge layer was detected. In some cases, during the mature phases of cells 19A and 19B in particular, there were lulls in the CG flash rate while the IC flashing between the main charge layer and this lower opposite charge layer became very active, thus causing the IC:CG ratio to become infinite. High IC:CG ratios have been observed by MacGorman et al. (1989) coincident with peak IC flash rates and kinematic strength in severe

[17] The use of the term "lower" here does not only refer to the lowest charge layer in a tripole configuration, but also to the layer of opposite (positive) charge that was located below the upper (negative) charge region of the (inverted) dipole involved in the 22 June negative CG flashes under the anvil. In general, we are referring to a layer of opposite charge being present below the charge layer being discharged by the CG flashes.

Oklahoma storms, and Lang and Rutledge (2002) showed, for a broader spectrum of storms, that increased kinematic intensity (updraft strength and volume) was common to low-CG (high IC:CG ratio) storms.

MacGorman et al. (1989) proposed an elevated charge mechanism, which suggests that intense updrafts elevate the charge layers in thunderstorms. This causes there to be greater distance between the ground and the charge layers and reduces the potential for ground flashes, while enhancing the IC flash rate. In partial agreement with this idea, we found a dipole charge structure within (strong) updraft regions and the charge was elevated (see Fig. 17b), and yet CG flashes were still occasionally observed below the somewhat elevated dipole (see Section 5.3). Generally, however, the majority of CG flashes were located outside the updraft below a tripolar charge structure in the reflectivity core. When the majority of CG lightning comes to ground outside the updraft, and when CGs are still observed below an elevated dipole, it casts doubt upon whether the elevated charge mechanism is actually affecting the CG flash rate. Perhaps during the intensification of the storm, coincident with peak IC flash rates and increasing kinematic intensity, the mechanism responsible for the generation of the lower charge layer is enhanced. This initial enhancement of the lower charge layer may then make IC flashes more energetically favorable than CG flashes, and thus might temporarily reduce the CG flash rate.

Dramatic differences in storm kinematics were observed between the 19 June and 22 June storms. The 22 June PPCG multicellular storm had similar maximum updraft speeds and UV10 as the 29 June PPCG supercell (Tessendorf et al. 2005), while the 19 June negative CG multicellular storm had two orders of magnitude less UV10 and less

than half of the maximum updrafts speeds as the two PPCG storms. How might the kinematic intensity affect the resultant charge structure and polarity of CGs produced?

Lang and Rutledge (2002) showed that enhanced kinematic intensity was a distinguishing factor of PPCG storms compared to non-PPCG storms. Williams et al. (2005) suggested that intense, broad updrafts, which are less susceptible to entrainment, should have higher supercooled liquid water contents (LWC) in the mixed-phase region. Enhanced LWC has been shown to cause the rimer (i.e. graupel) to acquire positive charge after an ice-ice collision (Takahashi 1978) and could perhaps explain the inverted (or opposite) sign of charge in the mixed-phase regions of these kinematically intense storms (around -10 to -20 °C).

We should point out that both of the PPCG storms did not have a clear inverted charge structure from the beginning (recall the four-layer structures of cell 22A and the 29 June supercell; Wiens et al. 2005), but it appeared that after some event in the storm's evolution, perhaps surges in updraft speed and increases in UV10, the storms became more inverted. Furthermore, the evolution of cell 22A into an inverted storm seems to be in conjunction with the development of the broad, strong updraft on the eastern flank of the cell. Recall that the four-layer, perhaps normal, charge structure was initially observed in cell 22A, and then as it merged with cell 22B a new broad updraft developed on the eastern flank, during which time a deep region of positive charge began to appear in the vicinity of that new updraft. The original four-layer charge structure was still evident, however, only the western flank of the storm (Fig. 14). This may give further evidence in favor of the kinematic argument as at least part of the reason for inverted storms.

Nonetheless, kinematic intensity cannot be the only factor leading to inverted charge structures, given that kinematically intense (severe) storms are observed in other regions of the U.S. and yet they still produce mostly negative CG lightning (Perez et al. 1997, Carey and Rutledge 2003). Therefore, we ask ourselves what other factor(s) could be aiding in the development of inverted charge structures, and subsequent PPCG lightning?

Williams et al. (2005) showed that climatologically higher cloud base heights, in combination with enhanced instability, are a unique feature of the High Plains. They suggest that higher cloud bases, relative to the melting level, reduce the warm cloud depth, and therefore lessen the opportunity for warm rain processes to deplete liquid water before it can reach the mixed-phase region of a storm. Wiens (2005) suggested that enhanced shear can offset the precipitation core from the updraft, and therefore allow the cloud base under the updraft to remain higher. This may have a similar effect on mixed-phase LWC as the idea proposed by Williams et al. (2005). Furthermore, we speculate that perhaps enhanced vertical wind shear elevates mixed-phase LWC if horizontal wind flow in the storm is curved such that precipitation grown in the storm can be re-ingested by the updraft. Elevated Z_{dr} values below the updraft are evidence of mm-sized drops (larger than can be grown from scratch below cloud base) being ingested into the updraft. Both the 22 June storm (see Fig. 15), as well as the 29 June supercell (Tessendorf et al. 2005), exhibited 'Z_{dr} columns'. The details of the microphysical processes that these recirculated drops undergo is quite complex, however, and both in situ observations and numerical simulations would be needed to further assess their potential for affecting non-inductive charging.

The High Plains region has a high frequency for hail (Changnon 2000) as well as PPCG storms, so how might hail affect the polarity of CG lightning? Hail production was also a distinguishing factor between the 19 June and 22 June storms (as well as the 29 June supercell; Tessendorf et al. 2005). It is possible that we commonly see hail in PPCG storms because higher LWC and strong kinematics are also conditions favorable for hail growth. At present, it is unclear whether the hail carries charge or is involved in charging that may invert the charge structure. Some studies suggest that hail is not an active participant in non-inductive charging collisions, due to its low number concentration relative to graupel it may carry less charge, and/or its tendency to grow wet or spongy, which may cause ice crystals to stick, rather than rebound, after a collision (Carey and Rutledge 1998, MacGorman et al. 2002, Kuhlman et al. 2006). Nonetheless, hail was present in the precipitation cores of the PPCG storms discussed herein. Whether it was actively involved in creating the inverted charge structure, or whether it had a role in the development of the lower negative charge layer involved in the positive CG flashes is beyond the scope of this paper, but warrants further study.

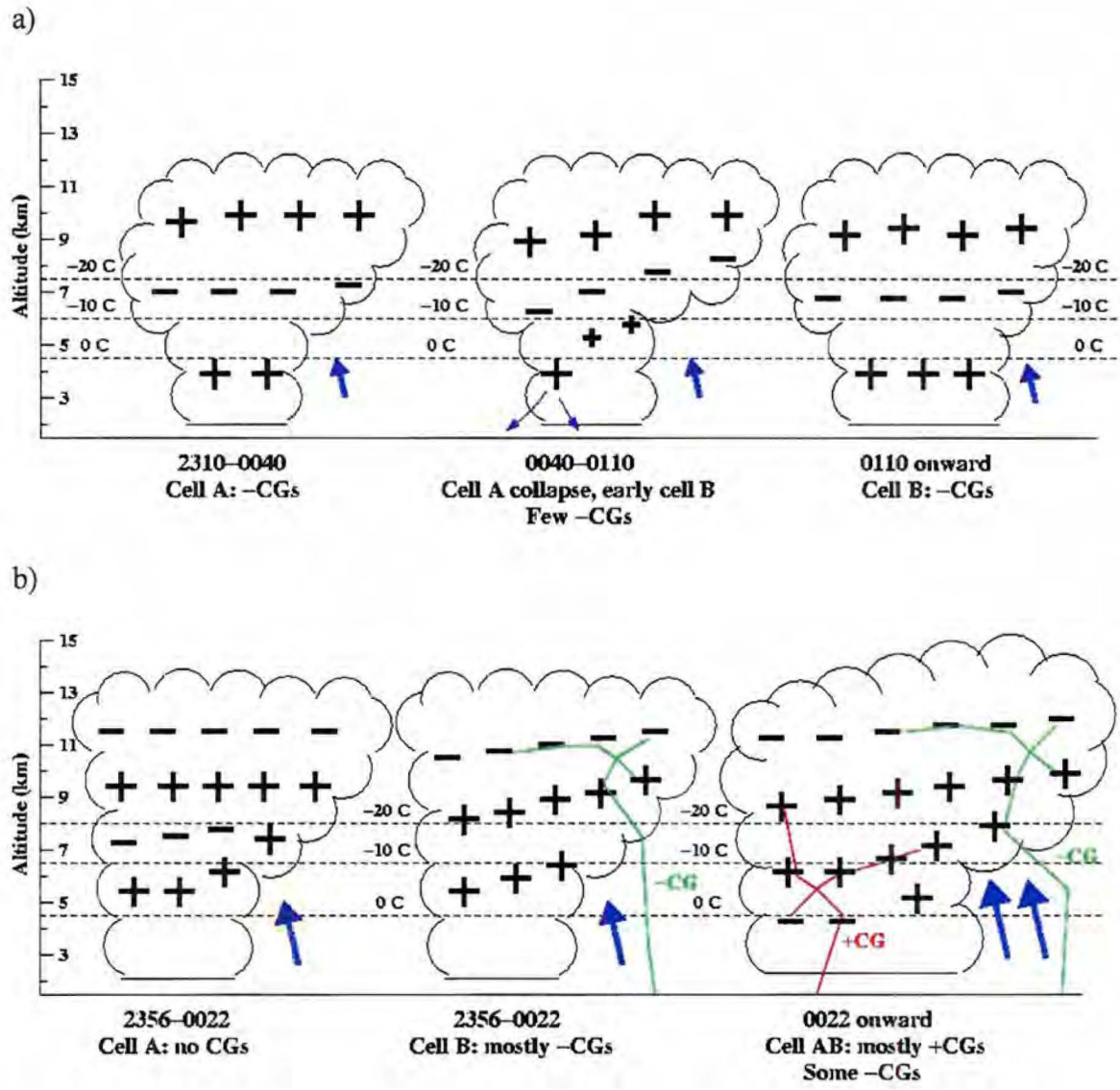

Figure 17. Schematic drawings of the general charge structure evolution for the (a) 19 June and (b) 22 June storms. Bold blue arrows are a proxy for updraft, and thus their size and width scales accordingly.

CHAPTER 7

CONCLUSIONS

The occurrence of inverted charge structures has now been documented in several storms, and enhanced kinematic intensity has continually been a distinguishing factor in PPCG storms, supporting Lang and Rutledge (2002), Williams et al. (2005), and Wiens et al. (2005). Secondly, the importance of the lower positive (negative) charge layer in the production of negative (positive) CGs is reemphasized. CG lightning that was detected in these two cases were observed in the presence of a lower opposite charge layer and/or the LMA-mapped flash involved a lower opposite charge layer. When the lower charge layer was not detected or had few LMA sources (indicating few flashes involved this layer), CG flashes were more rarely observed. Moreover, a temporarily enhanced lower charge layer is suggested as an alternative to the elevated charge mechanism to explain lulls in CG flash rates during periods of high IC flashing. In order to validate these ideas, further research is needed to better identify and understand the specific storm processes that are involved in generating inverted charge structures and in the development of the lower charge layer. This needs to be done by incorporating numerical models of cloud thermodynamics, microphysics, and electrification and by acquiring more in situ observations of particle charge and LWC within the electrified regions of thunderstorms.

REFERENCES

Branick, M.L., and C.A. Doswell III, 1992: An observation of the relationship between supercell structure and lightning ground strike polarity. *Wea. Forecasting*, **7**, 143-149.

Carey, L.D. and S.A. Rutledge, 1998: Electrical and multiparameter radar observations of a severe hailstorm. *J. Geophys. Res.*, **103**, 13,979-14,000.

Carey, L,D., and S.A. Rutledge, 2003: Characteristics of cloud-to-ground lightning in severe and nonsevere storms over the central United States from 1989-1998. *J. Geophys. Res.*, **108**, doi: 10.1029/2002JD002951.

Carey, L.D., W.A. Petersen, and S.A. Rutledge, 2003: Evolution of cloud-to-ground lightning and storm structure in the Spencer, South Dakota, tornadic supercell of 30 May 1998. *Mon. Wea. Rev.*, **131**, 1811-1831.

Changnon, S.A., 2000: The impacts of hail in the United States. *Storms*, Routledge Press, 163-191.

Coleman, L.M., T.C. Marshall, M. Stolzenburg, T. Hamlin, P.R. Krehbiel, W. Rison, and R.J. Thomas, 2003: Effects of charge and electrostatic potential on lightning propagation. *J. Geophys. Res.*, **108**, doi: 10.1029/2002JD002718.

Cummins, K. L., M. J. Murphy, E. A. Bardo, W. L. Hiscox, R. B. Pyle, and A. E. Pifer, 1998: A combined TOA/MDF technology upgrade of the U.S. National Lightning Detection Network. *J. Geophys. Res.*, **103** (D8), 9035–9044.

Grumm, R.H., J. Ross, and P. Knight, 2005: Examining severe weather events using reanalysis datasets. Preprints, 21st Conf on Weather Analysis and Forecasting/17th Conf. on Numerical Weather Prediction, Washington, DC.

Kasemir, H.W., 1960: A contribution to the electrostatic theory of lightning discharge. *J. Geophys. Res.*, **65**, 1873-1878.

Krehbiel, P.R., R.J. Thomas, W. Rison, T. Hamlin, J. Harlin, and M. Davis, 2000: GPS-based mapping system reveals lightning inside storms. *Eso, Trans. Amer. Geophys. Union*, **81**, 21-25.

Kuhlman, K.M., C.L. Ziegler, E.R. Mansell, D.R. MacGorman, and J.M. Straka, 2006: Numerical simulations of the 29 June 2000 STEPS supercell: Microphysics, electrification, and lightning. *Mon. Wea. Rev.,* in review.

Lang, T.J., and S.A. Rutledge, 2002: Relationships between convective storm kinematics, precipitation, and lightning. *Mon. Wea. Rev.*, **130**, 2492-2506.

Lang, T.J., and Coauthors, 2004: The Severe Thunderstorm Electrification and Precipitation Study. *Bull. Amer. Meteor. Soc.*, **85**, 1107-1125.

Liu, H., and V. Chandrasekar, 2000: Classification of hydrometeors based on polarimetric radar measurements: Development of fuzzy logic and neuro-fuzzy systems and in situ verification. *J. Atmos. Oceanic Technol.*, **17**, 140-164.

MacGorman, D.R., and D.W. Burgess, 1994: Positive cloud-to-ground lightning in tornadic storms and hailstorms. *Mon. Wea. Rev.*, **122**, 1671-1697.

MacGorman, D.R., D.W. Burgess, V. Mazur, W.D. Rust, W.L. Taylor, and B.C. Johnson, 1989: Lightning rates relative to tornadic storm evolution on 22 May 1981. *J. Atmos. Sci.*, **46**, 221-250.

MacGorman, D., and coauthors: 2002: Lightning relative to precipitation and tornadoes in a supercell storm during MEaPRS. Preprints, 21st Conf. on Severe Local Storms, San Antonio, TX, 423-426.

MacGorman, D.R., W.D. Rust, P. Krehbiel, E. Bruning, and K. Wiens, 2005: The electrical structure of two supercell storms during STEPS. *Mon. Wea. Rev.*, **133**, 2583-2607.

Mansell, E.R., D.R. MacGorman, C. Ziegler, and J.M. Straka, 2002: Simulated three-dimensional branched lightning in a numerical thunderstorm model. *J. Geophys. Res.*, **107**, doi: 10.1029/2000JD00244.

Mansell, E.R., D.R. MacGorman, C.L. Ziegler, and J.M. Straka, 2005: Charge structure and lightning sensitivity in a simulated multicell thunderstorm. *J. Geophys. Res.*, **110**, doi: 10.1029/2004/JD005287.

Marshall, T.C., and M. Stolzenburg, 2002: Electrical energy constraints on lightning. *J. Geophys. Res.,* **107**, doi: 10.1029/2000JD000024.

Mazur, V. and L. H. Ruhnke, 1993: Common physical processes in natural and artificially triggered lightning. *J. Geophys. Res.*, **98**, 12,913-12,930.

Mohr, C.G., L.J. Miller, R.L. Vaughn, and H.W. Frank, 1986: On the merger of mesoscale data sets into a common Cartesian format for efficient and systematic analysis. *J. Atmos. Oceanic. Technol.*, **3**, 143-161.

Nelson, S.P., 1987: The hybrid multicellular-supercellular storm—An efficient hail producer. Part II: General characteristics and implications for hail growth. *J. Atmos. Sci.*, **44**, 2060-2073.

O'Brien, J.J., 1970: Alternative solutions to the classical vertical velocity problem. *J. Appl. Meteor.*, **9**, 197-203.

Orville, R.E., and G.R. Huffines, 2001: Cloud-to-ground lightning in the United States: NLDN results in the first decade, 1989-98. *Mon. Wea. Rev.*, **129**, 1179-1193.

Perez, A.H., L.J. Wicker, and R.E. Orville, 1997: Characteristics of cloud-to-ground lightning associated with violent tornadoes. *Wea. Forecasting*, **12**, 428-437.

Rison, W., R. J. Thomas, P. R. Krehbiel, T. Hamlin, and J. Harlin, 1999: A GPS-based three-dimensional lightning mapping system: Initial observations in Central New Mexico. *Geophys. Res. Lett.*, **26**, 3573-3576.

Rust, W.D., D.R. MacGorman, and R. T. Arnold, 1981: Positive cloud-to-ground flashes in severe storms. *Geophys. Res. Lett.*, **8**, 791-794.

Seimon, A., 1993: Anomalous cloud-to-ground lightning in an F5-tornado-producing supercell thunderstorm on 28 August 1990. *Bull. Amer. Meteor. Soc.*, **74**, 189-203.

Stolzenburg, M., W.D. Rust, and T.C. Marshall, 1998: Electrical structure in thunderstorm convective regions, 3. Synthesis. *J. Geophys. Res.*, **103**, 14,097-14,108.

Straka, J.M., D.S. Zrnic, and A.V. Ryzhkov, 2000: Bulk hydrometeor classification and quantification using polarimetric radar data: Synthesis of relations. *J. Appl. Meteor.*, **39**, 1341-1372.

Takahashi, T., 1978: Riming electrification as a charge generation mechanism in thunderstorms. *J. Atmos. Sci.*, **35**, 1536-1548.

Tessendorf, S.A., L.J. Miller, K.C. Wiens, and S.A. Rutledge, 2005: The 29 June 2000 supercell observed during STEPS. Part I: Kinematics and microphysics. *J. Atmos. Sci.*, **62**, 4127-4150.

Thomas, R., P. Krehbiel, W. Rison, J. Harlin, T. Hamlin, and N. Campbell, 2003: The LMA flash algorithm. Abstract C4-23, *Proc. 12th Intl. Conf. On Atmos. Elect.*, 655-656, Versailles, France.

Wiens, K.C., 2005: *Kinematic, microphysical, and electrical structure and evolution of thunderstorms during the Severe Thunderstorm Electrification and Precipitation Study (STEPS).* Ph.D. thesis, Colorado State University, Fort Collins, CO, 295 pp.

Wiens, K.C., S.A. Rutledge, and S.A Tessendorf, 2005: The 29 June 2000 supercell observed during STEPS. Part II: Lightning and charge structure. *J. Atmos. Sci.,* **62**, 4151-4177.

Williams, E.R., 1989: The tripole structure of thunderstorms. *J. Geophys. Res.,* **94**, 13,151-13,167.

Williams, E.R., M.E. Weber, and R.E. Orville, 1989: The relationship between lightning type and convective state of thunderclouds. *J. Geophys. Res.*, **94**, 213-220.

Williams E.R., 2001: The electrification of severe storms. *Severe Convective Storms*, C.A. Doswell, III, Ed., *Meteor. Monogr.*, No. 50, Amer. Meteor. Soc., 527-561.

Williams, E., V. Mushtak, D. Rosenfeld, S. Goodman, and D. Boccippio, 2005: Thermodynamics conditions favorable to superlative thunderstorm updraft, mixed phase microphysics and lightning flash rate. *Atmos. Res.,* **76**, 288-306.

PART IV: OVERALL SUMMARY AND CONCLUSIONS

CHAPTER 1

SUMMARY

In this dissertation, four cases from the STEPS field campaign have been studied in detail: one negative CG-dominated storm, a storm where no CGs (of either polarity) were observed, and two positive CG-dominated (or PPCG) storms. This part of the dissertation provides an overall summary of the observations presented in Parts I-III, and highlights the main conclusions from these studies.

The objective of this dissertation was to analyze Doppler and polarimetric radar observations, in addition to LMA total lightning data, to determine the charge structure of each storm, especially in relation to the polarity of cloud-to-ground lightning, and assess the kinematic and microphysical processes in each storm that relate to the observed electrification and lightning. In Part I, kinematics and microphysics of the 29 June 2000 PPCG supercell were presented, with a special focus on the mechanisms related to hail production. The electrification and lightning observations of the 29 June 2000 supercell are summarized in Wiens et al. (2005). In Part II, the radar and lightning observations of the 3 June 2000 LP supercell, where no CG lightning was detected, were discussed. In Part III, radar and lightning observations of two multicellular storms were presented: the 19 June 2000 negative CG-dominated storm and the PPCG storm on 22 June 2000.

1.1 Kinematic and microphysical relationships

The four cases studied in this dissertation fall onto distinct locations on a spectrum of kinematic intensity (via UV10 in Figure 1). The kinematically weakest storm was that of 19 June, with UV10 on the order of 10 km^3 (Fig. 1) and maximum updraft speeds near 15 m s^{-1} (see Part III). The UV10 on 3 June (O ~ 10^2 km^3) was on order of magnitude higher than on 19 June, and the UV10 on 29 and 22 June were even an order of magnitude larger than 3 June at 10^3 km^3. Maximum updraft velocities on 3 June were near 25 m s^{-1} (see Part II), while they were twice as high (near 50 m s^{-1}) on 29 and 22 June (see Parts I and III), further supporting the observation that the overall kinematic intensity (UV10 and maximum updraft) was highest in the PPCG storms (Lang and Rutledge 2002).

The graupel EV related to UV10 such that for high UV10 (greater than 10^4 km^3), graupel EV increased, yet for lower UV10, the graupel EV seemed nearly constant at around 10^3 km^3 (Fig. 1). The data points from 19 June (in the lower end of the UV10 spectrum) might be influenced by seeding of graupel particles grown in nearby convection, especially in storm 19 B, such that the graupel EV values may be higher than they would have been without seeding and based only on the kinematic intensity of the storm itself (see Part III). Thus, the graupel EV and UV10 relationship might be more linear in the absence of these possible seeding effects.

Figure 2 shows that as UV10 increases, the *maximum* hail EV observed at each UV10 interval increases (Fig. 2), but the remaining hail EV values can vary below that maximum value for all UV10 magnitudes. These variations indicate that although UV10 may constrain the maximum hail EV that can be produced, it alone does not govern the

quantity of hail produced by a storm, which more likely is a combination of other factors that also include maximum updraft and vertical vorticity. In Part I, four criteria for (large) hail growth were outlined: (1) small near-mm to mm-sized embryonic particles must be present, (2) there must be a mechanism for transporting these particles into the updraft, (3) the updraft must be of sufficient size and intensity to grow these embryonic particles into hail, and (4) the horizontal winds must keep the growing particles within favored hail growth conditions. In particular, it was shown that UV10 was required to produce hail, but that a large region of cyclonically curved flow around the *right flank* of the updraft was apparently critical for the production of any hail larger than 20 mm. The lack of cyclonic vorticity on the right flank of the updraft in 3 June may have prevented that storm from producing large hail as 29 June did. It is noteworthy that the 3 June storm was very similar to the 29 June storm, prior to its right turn, especially in their magnitudes of UV10, graupel EV, and total lightning flash rate (Figs. 1, 3). It is unclear, however, exactly why the 29 June storm became so much more intense, other than that the beginning of its intensification was coincident with the right turn. Furthermore, the cyclonic vorticity in 29 June was collocated with the updraft (as it was during in the 3 June storm) prior to its right turn, and then it became more offset on the right flank of the updraft after the right turn, allowing for large hail growth (see Parts I and II).

1.2 Kinematic and microphysical relationships with lightning

It has been well established that riming ice (i.e. graupel) is important in charge separation based on precipitation charging theory (Takahashi 1978, Saunders and Peck 1998). The relationship between graupel EV and total lightning flash rate in these four

cases further supports this important relationship. As seen in Figure 3, the total lightning flash rate increases as the quantity of graupel EV increases. It is also clear in this figure that the 22 June storm had the highest flash rates and graupel EV, followed by 29 June, where in both cases the total flash rates were on the order of 100 min^{-1}. The 19 June storm had more moderate flash rates and graupel EV, while the 3 June storm had very low flash rates (none greater than 30 min^{-1}) and graupel EV. There are a few data points in Figure 3 from 29 June where the flash rates were as low as those on 3 June, and the graupel EV was lower than any of the other cases. These points are from the early evolution of the 29 June storm *prior* to its severe right mature phase, during which time it exhibited flash rates and graupel EV near the same magnitude as the 3 June storm. The extraordinary flash rates as high as 300 $min^{-1}$and high quantities of graupel EV in 29 June were observed during its severe right mature phase.

It has also been shown that total flash rate tends to scale with kinematic intensity (Lang et al. 2000, Lang and Rutledge 2002), however in these observations, the 3 June storm is an outlier for both the relationships between UV10 and total flash rate (Fig. 4), in addition to maximum updraft velocity versus total flash rate (see section 1.1 for discussion of maximum updraft between the four cases). The flash rates in 3 June are particularly low for the kinematic strength of the storm, perhaps because it produced less graupel compared to storms with similar UV10 and maximum updraft (see section 1.1). Graupel has been shown to be important for electrification processes, as shown in Fig. 3, and the 3 June data follows this relationship (graupel EV and total flash rate) much better than for kinematic intensity versus total flash rate. It is also important to note that the storms with the highest flash rates and UV10 were the two PPCG storms (29 June and 22

June). Consistent with Lang and Rutledge (2002) and Williams et al. (2005), the PPCG storms have very strong kinematic intensity, perhaps allowing enhanced positive charging of graupel (via large supercooled liquid water contents in the storm) and leading to inverted charge structures.

1.3 Charge structure

The negative CG-dominated storms on 19 June had characteristic normal polarity charge structures. Midlevel negative charge was observed at 7-8 km (-10 to -15 °C), with upper level positive charge near 10 km, making up a "normal dipole" in the storm (Fig. 5a). In the precipitation core (particularly *not* in the updraft region), a lower level positive charge layer was commonly observed below 5 km, making the charge structure consistent with a "normal tripole" (Williams 1989).

The 3 June storm exhibited an "inverted dipole" charge structure, with a deep midlevel region of positive charge from 6-8 km (-10 to -20 °C) and an upper level layer of negative charge at 10-11 km (Fig. 5b). There were never any flashes indicating a lower level negative charge throughout the evolution of this storm. The PPCG storms of 29 June and 22 June both exhibited characteristic "inverted tripole" charge structures, especially once they had entered their intense phases and were producing frequent positive CG lightning (Fig. 5c-d). These charge structures consisted of a midlevel positive chare region and an upper level negative layer, much like that of 3 June, but there was also a lower level negative charge layer observed in these storms, mostly confined to the precipitation core. In the updraft regions of 29 June and 22 June, during their final stage in charge structure evolution (i.e. their PPCG phase; see the right hand

side of Fig. 5c-d), both storms exhibited an inverted dipole with positive charge underlying negative charge.

During the early evolution of the 29 June and 22 June (cell 22A) charge structure, a four-layer alternating charge structure, the lowest layer being positive charge, was observed (see the left hand side of Fig. 5c-d). This type of charge structure could be termed a "double dipole" where both dipoles are inverted, or a normal tripole "plus one" (with the additional upper negative layer). There were IC flashes that originated between both the upper and lower dipoles. In cell 22A, as it began to merge with cell 22B and a strong, broad updraft developed on its eastern flank, a deeper region of positive charge was observed (see Part III). It appears, in both of these cases, that the charge structure evolved into an inverted tripole, rather than being inverted from the very beginning (such as the 3 June storm was). It was not until the storms had developed the general inverted tripole charge structure that they began producing frequent positive CG lightning.

The lack of CG lightning in the 3 June (inverted dipole) storm and prior to the development of the inverted dipole in the 29 and 22 June storms, lends support to the involvement of a lower negative charge layer in positive CG flash development. In addition, the positive CG flashes in these cases were observed to come to ground below the lower negative charge layer (Fig. 5c-d). This is analogous to a lower *positive* charge layer being required for a *negative* CG to come to ground (Williams 1989, Williams et al. 1989, and Mansell et al. 2002, 2005). Indeed, in the 19 June storm, negative CG flashes were also observed to come to ground below the lower positive charge layer of the normal tripole charge structure (Fig. 5a). Negative CGs were also observed in the 22 June storm, however, in this case they emanated from an upper level negative charge

layer at 11 km, and came to ground through the midlevel positive charge layer of the inverted dipole in the anvil (Fig. 5d). Nonetheless, an intervening "lower" positive charge layer was involved in the flash and present below the negative charge being tapped by the CG discharge.

The presence of the lower opposite charge layer alone may not be sufficient to indicate that CG flashes will occur, however, as we observed lulls in CG flash rate even when a lower opposite charge layer was detected. A specific example of this occurred on 19 June, during both intensification phases of storms A and B (see Part III). During these lulls in negative CG flash rate, enhanced IC flashes between the lower positive charge layer and the midlevel negative region were observed. This suggests that IC flashes were energetically favorable over CG flashes during these times. Though we cannot identify the reason for this preference for low-level IC flashes, we speculate that perhaps the lower positive charge layer was temporarily enhanced during these intensification periods such that charge from a lightning discharge would be neutralized before making it to ground. Regardless of the mechanism that prevents CGs from occurring in the presence of lower opposite charge, the presence of the lower opposite charge layer seems necessary in order for CGs to occur.

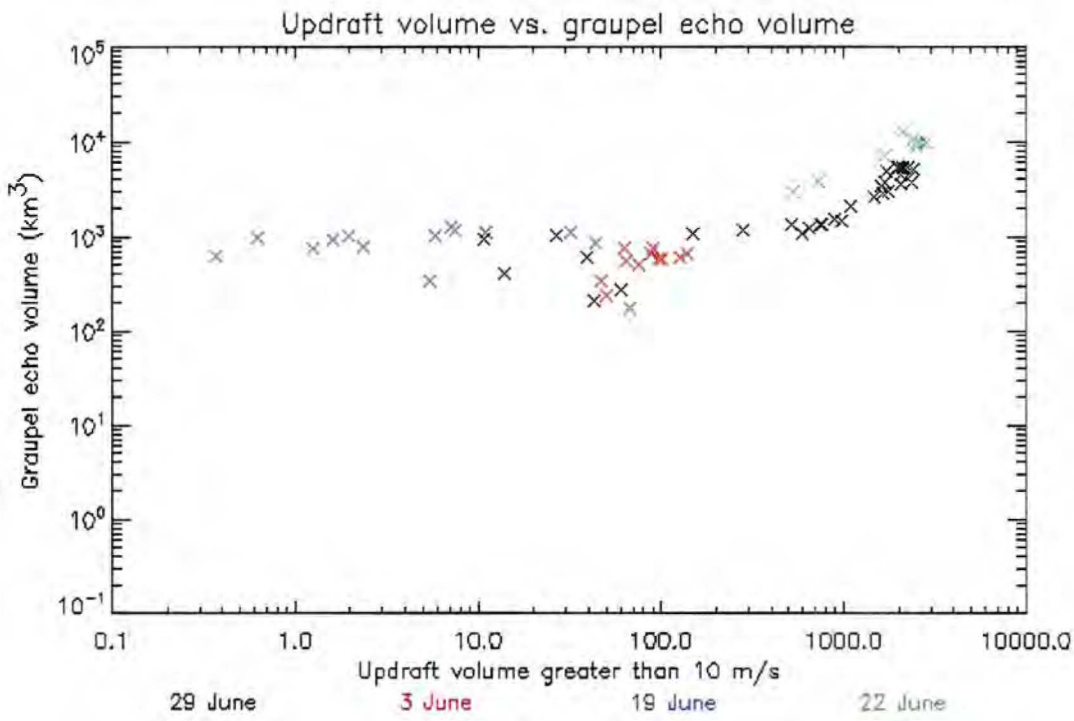

Figure 1. Scatter plot of updraft volume greater than 10 m s^{-1} (UV10) versus graupel echo volume for all four cases studied, with each 'X' representing a single radar volume/analysis time, color-coded by case (black = 29 June, red = 3 June, blue = 19 June, green = 22 June).

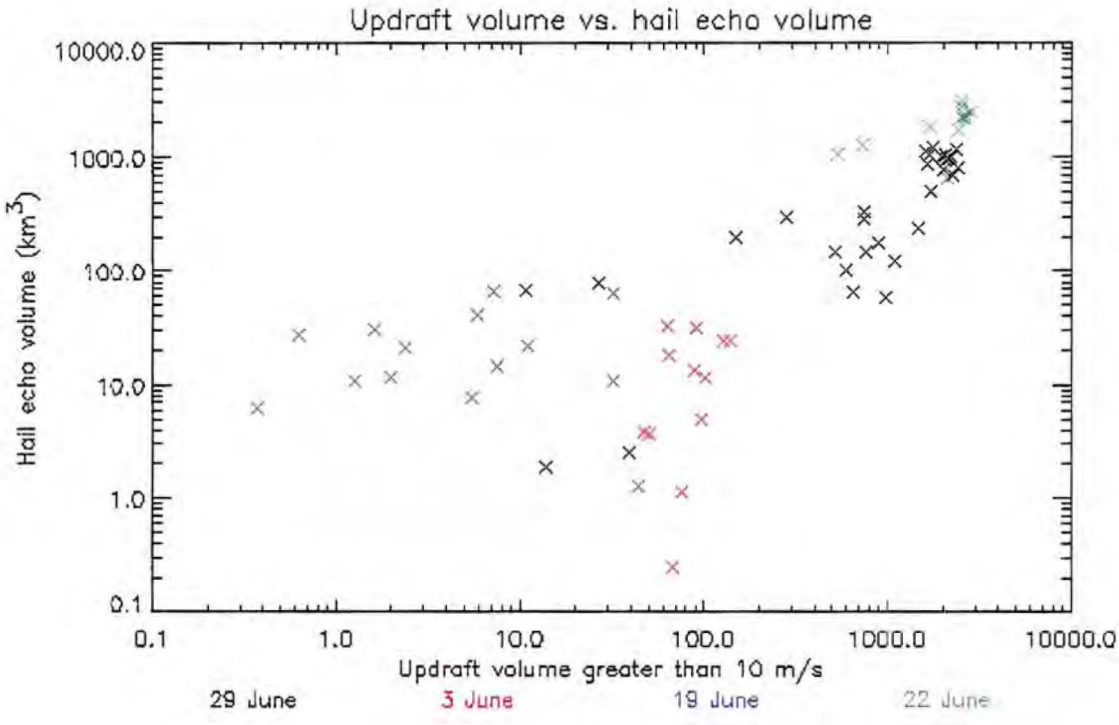

Figure 2. Same as Figure 1 except for UV10 versus hail echo volume.

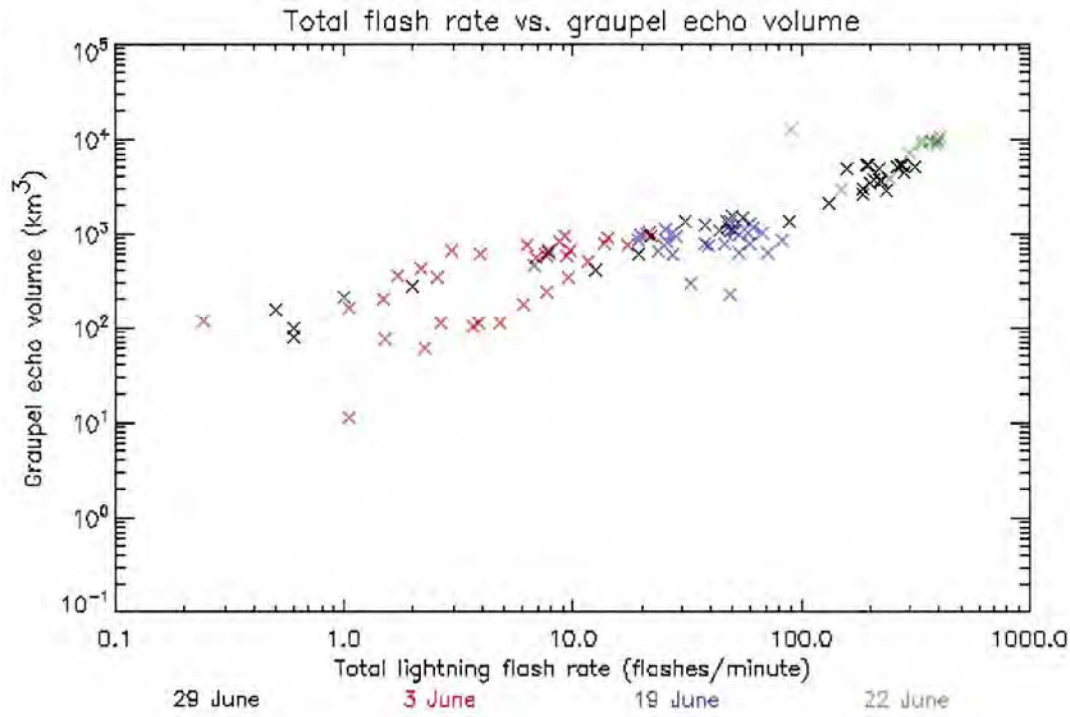

Figure 3. Same as Figure 1 except for total flash rate versus graupel echo volume.

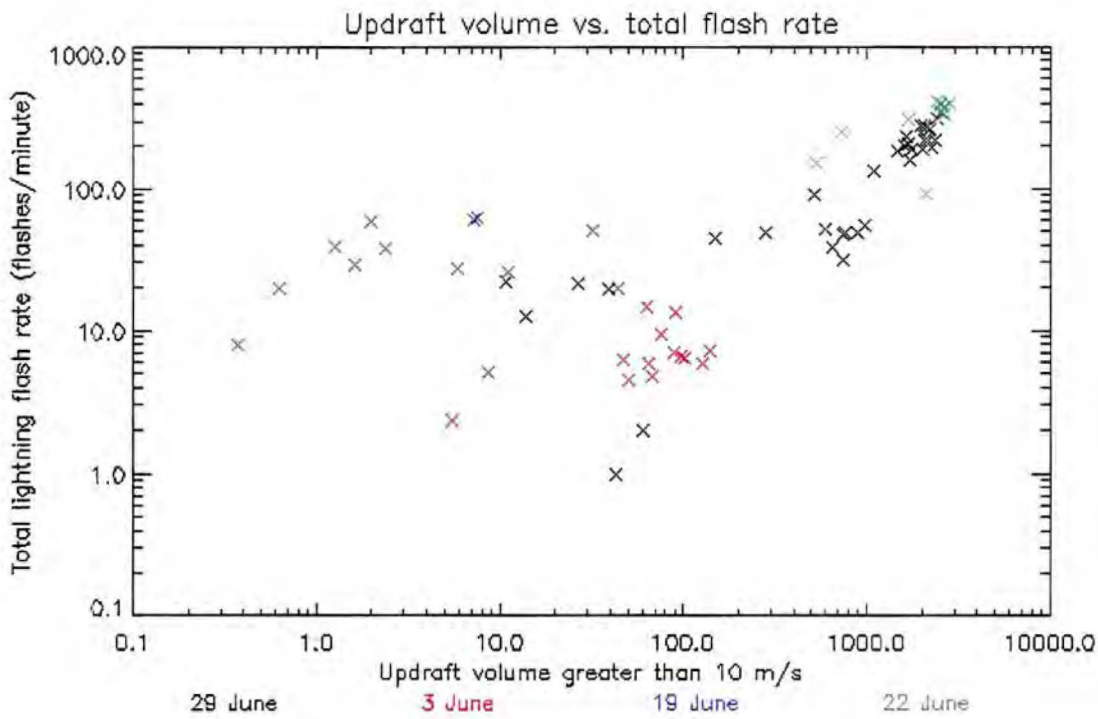

Figure 4. Same as Figure 1 except for UV10 versus total flash rate.

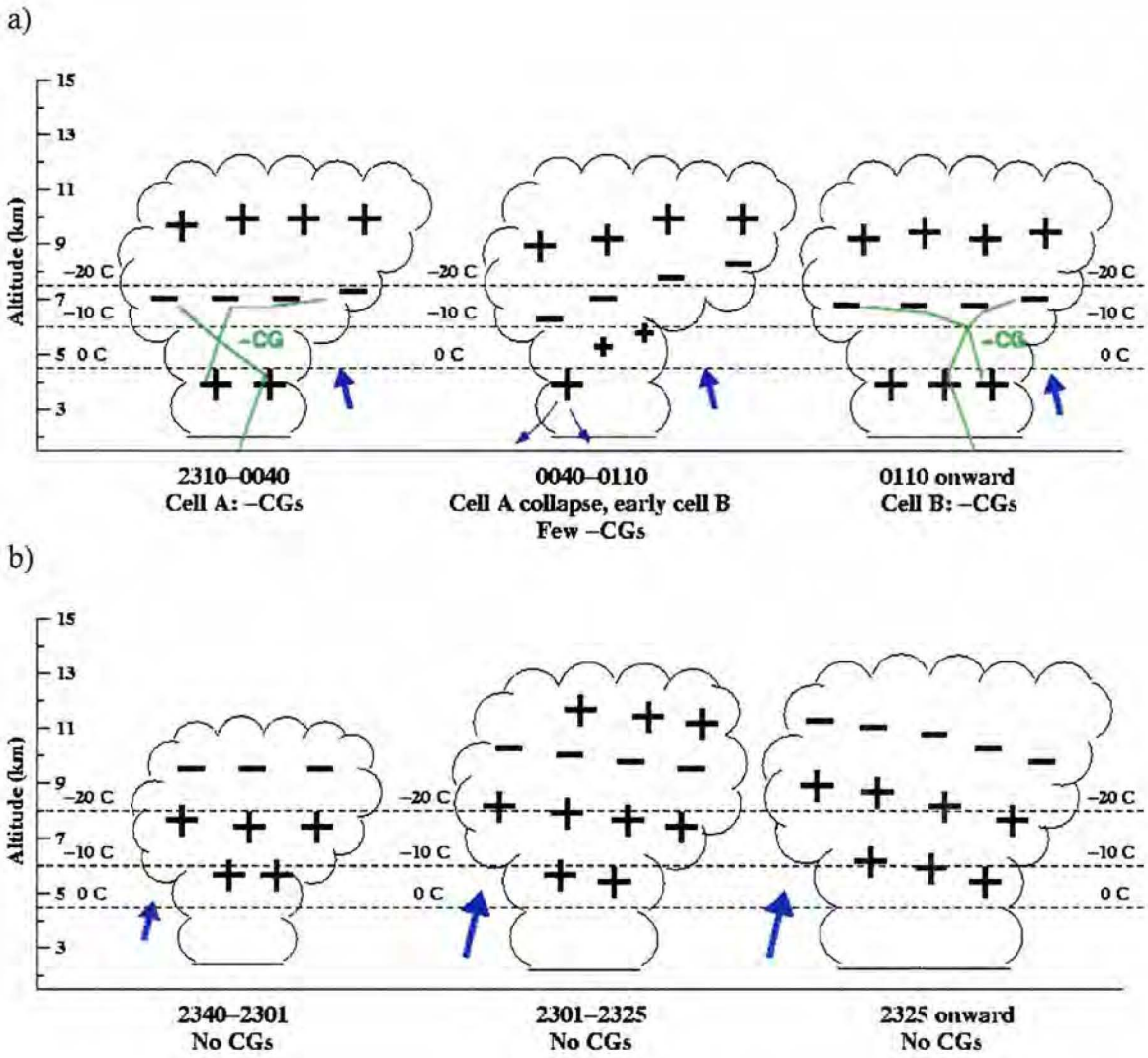

Figure 5. Schematic illustrations summarizing the representative charge structure evolution for each of the four cases: (a) 19 June (from Part III), (b) 3 June, (c) 29 June (from Wiens et al. 2005), and (d) 22 June (from Part III). Bold blue arrows illustrate the characteristic size and strength of the updraft. CG flashes are illustrated in red (positive CG) and green (negative CG). Thin blue arrows illustrate relevant airflow and particle motions.

c)

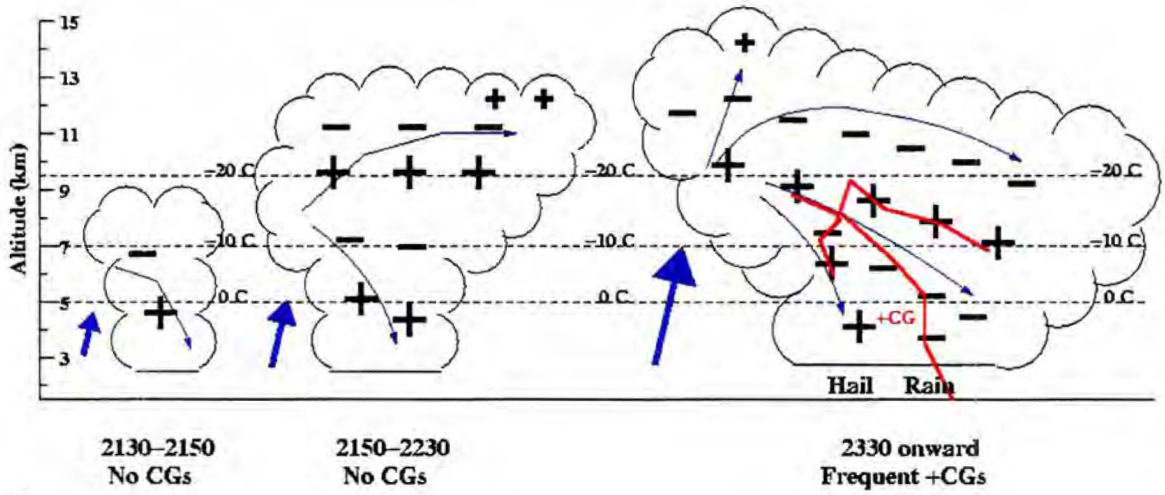

d)

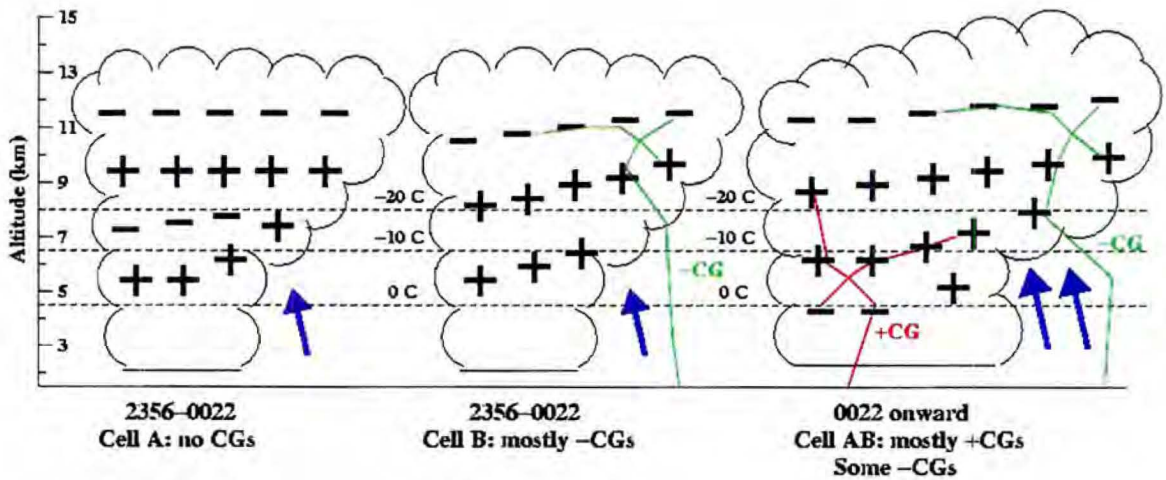

Figure 5 (cont'd).

CHAPTER 2

OVERALL CONCLUSIONS AND FUTURE WORK

The occurrence of inverted charge structures has now been documented in three storms observed during STEPS, two of which exhibited inverted *tripole* structures and produced PPCG lightning. Much like the lower positive charge layer has been deemed important in producing negative CG flashes, we suggest that the lack of the lower *negative* charge layer, which completes the *inverted* tripole (which, if present would provide the downward bias for positive CG flashes), was a key factor in preventing the 3 June storm from producing positive CG flashes. CG lightning that was detected in these cases were observed in the presence of a lower opposite charge layer and/or the LMA-mapped flash involved a lower opposite charge layer. When the lower charge layer was not detected or weakly detected, CG flashes were more rarely observed. Thus, the importance of the lower positive (negative) charge layer in the production of negative (positive) CGs has been documented by our LMA observations, and we would therefore add a lower negative charge layer to the inverted dipole (Williams 2001), making it an inverted *tripole*, hypothesis for the charge structure responsible for producing PPCG storms in the STEPS region.

Additionally, based on the observations presented herein, enhanced kinematic intensity remains a distinguishing factor in PPCG storms, supporting Lang and Rutledge (2002), Williams et al. (2005), and Wiens et al. (2005). However, we suggest that

enhanced kinematic intensity is not a sufficient condition for *inverted* storms, given that the 3 June storm was also inverted but had only moderate kinematic intensity, and kinematically intense storms are observed in other regions of the U.S. which produce mostly negative CG lightning (these storms more than likely have normal charge structures though there are limited charge structure observations to confirm this).

There are clearly more questions to be answered and further work is needed to validate the ideas presented herein. Specific questions that still need addressed are:

1) What causes a charge structure to become inverted?

2) How does the low-level charge layer (involved in CG flashes) develop?

Environmental variables, those specific to the STEPS region in particular, might have some influence on the high frequency of PPCG storms in this region, however, statistical analysis of a variety of environmental parameters in relation to the polarity of CG lightning over a broad region (extending well beyond the anomalous PPCG region) is needed. In addition, it has certainly been shown, conceptually and through storm-scale observations (Lang and Rutledge 2002, Williams et al. 2005, Wiens et al. 2005, herein), that enhanced kinematic intensity might contribute to the development of inverted charge structures, however, as mentioned above it is not a sufficient condition. We need better in situ measurements of liquid water content in updrafts (or more importantly, regions where charge separation is occurring), as well as more consistent laboratory studies of non-inductive charging to better assess the parameters that might cause an inverted charge structure to develop. In order to answer the second question, we need charge structure observations of more storms (both with and without CG flashes), in addition to

modeling simulations to better understand the processes (inductive vs. non-inductive, etc…) that contribute to the production of the lower level opposite charge layer.

REFERENCES

Lang, T.J., and S.A. Rutledge, 2002: Relationships between convective storm kinematics, precipitation, and lightning. *Mon. Wea. Rev.*, **130**, 2492-2506.

Lang, T.J., S.A. Rutledge, J.E. Dye, M. Venticinque, P. Laroche, and E. Defer, 2000: Anomalously low negative cloud-to-ground lightning flash rates in intense convective storms observed during STERAO-A. *Mon. Wea. Rev.*, **128**, 160-173.

Mansell, E.R., D.R. MacGorman, C. Ziegler, and J.M. Straka, 2002: Simulated three-dimensional branched lightning in a numerical thunderstorm model. *J. Geophys. Res.*, **107**, doi: 10.1029/2000JD00244.

Mansell, E.R., D.R. MacGorman, C.L. Ziegler, and J.M. Straka, 2005: Charge structure and lightning sensitivity in a simulated multicell thunderstorm. *J. Geophys. Res.*, **110**, doi: 10.1029/2004/JD005287.

Saunders, C.P.R., and S.L. Peck, 1998: Laboratory studies of the influence of the rime accretion rate on charge transfer during graupel/crystal collisions. *J. Geophys. Res.*, **103**, 13,949-13,956.

Takahashi, T., 1978: Riming electrification as a charge generation mechanism in thunderstorms. *J. Atmos. Sci.*, **35**, 1536-1548.

Wiens, K.C., S.A. Rutledge, and S.A Tessendorf, 2005: The 29 June 2000 supercell observed during STEPS. Part II: Lightning and charge structure. *J. Atmos. Sci.*, **62**, 4151-4177.

Williams, E.R., 1989: The tripole structure of thunderstorms. *J. Geophys. Res.*, **94**, 13,151-13,167.

Williams E.R., 2001: The electrification of severe storms. *Severe Convective Storms*, C.A. Doswell, III, Ed., *Meteor. Monogr.*, No. 50, Amer. Meteor. Soc., 527-561.

Williams, E.R., M.E. Weber, and R.E. Orville, 1989: The relationship between lightning type and convective state of thunderclouds. *J. Geophys. Res.*, **94**, 13,213-13,220.

Williams, E., V. Mushtak, D. Rosenfeld, S. Goodman, and D. Boccippio, 2005: Thermodynamics conditions favorable to superlative thunderstorm updraft, mixed phase microphysics and lightning flash rate. *Atmos. Res.,* **76**, 288-306.